ABSTRACT

Title of Document: **ENHANCEMENT OF A CANOPY REFLECTANCE MODEL FOR UNDERSTANDING THE SPECULAR AND SPECTRAL EFFECTS OF AN AQUATIC BACKGROUND IN AN INUNDATED TIDAL MARSH**

Kevin Ross Turpie, Ph.D., 2012

Directed By: **Professor Michael Kearney, Department of Geographical Sciences**

The presence of water produces unique specular and spectral characteristics in an inundated tidal marsh canopy. The aquatic substrate can affect conventional attempts to retrieve canopy characteristics, such as structure information (e.g., canopy height, leaf area index, etc.) or plant species composition. The background reflectance can also influence spectral analysis of plant characteristics based on hyperspectral data. A model to account for the aquatic substrate would be useful to understanding spectral field measurements and remote sensing of this type of land cover. To that end, an existing vegetation canopy reflectance model is combined with an aquatic background model to account for the effects of an aquatic substrate on the top-of-canopy bidirectional reflectance. The aquatic background model attempts to account for the optical effects of an inundated marsh substrate through the inclusion of first-principle models of water reflectance. The enhanced model is applied to multi-angular reflectance measured along

transects of a brackish marsh canopy. This allows us to explore whether the enhanced model can be used in retrieving the leaf area index (LAI) using non-destructive, above-canopy measurements. Then the original and the enhanced canopy reflectance models are compared with multi-angular reflectance data to test whether the change is effective in capturing specular effects of an inundated canopy. Furthermore the reflectance data and model are used to identify the influence of the background on the spectral characteristics of the canopy pertaining to vegetation. The spectral signature produced by the aquatic background model is quite different from the spectra of dry or unsaturated soil, which would be associated with terrestrial applications. The aquatic background model signature is used to explain the features seen in a field spectroscopy experiment, where canopy inundation levels were artificially raised. This project demonstrates the utility of developing a vegetation canopy model with an aquatic background and identifies challenges and directions for improved performance.

ENHANCEMENT OF A CANOPY REFLECTANCE MODEL FOR UNDERSTANDING THE SPECULAR AND SPECTRAL EFFECTS OF AN AQUATIC BACKGROUND IN AN INUNDATED TIDAL MARSH

By

Kevin Ross Turpie

Dissertation submitted to the Faculty of the Graduate School of the
University of Maryland, College Park, in partial fulfillment
of the requirements for the degree of
Doctor of Philosophy
2012

Advisory Committee:
Dr. Michael S. Kearney, Chair
Dr. Michelle A. Hofton
Dr. Naijun Zhou
Dr. Karl F. Huemmrich
Dr. David R. Tilley

Dedication

בסיעתא דשמיא

היגאה גמא בלא בצה? ישגה–אחו בלי–מים?

עדנו באבו לא יקטף; ולפני כל–חציר ייבש.

Can the rush shoot up without the marsh? Can the reed-grass grow without water?

While it is yet green, and not cut down, it withers before any herb.

Job 8:11-12

This project is dedicated to my wonderful wife, Sharon Shoshana, and our children, Yehudah Arial and his wife Shoshana Hanna, Bari Nathan, Aharon Akiva, and Alexandra Eliyah, without whose love, extraordinary understanding, and endless patience, this work would have been impossible. They have made many sacrifices and even participated in fieldwork. I am truly grateful to have been blessed with a supportive family that shares a love of science and nature.

Acknowledgements

Dissertation research is considered a highly independent activity. Yet clearly research is not done *in vacuo*. Naturally, the effort must be independently vetted and well grounded in the achievements of others. But, we also require the support and backing of those that find value in our work. Furthermore, we draw on alternative perspectives, emotional support, and even inspiration from our teachers, mentors, colleagues, and friends. For this work, I am indebted to Dr. Wayne E. Esaias and Dr. Charles R. McClain at NASA Goddard Space Flight Center (GSFC) for years of unwavering encouragement and inspiration, to Dr. Paula S. Bontempi at NASA Headquarters for her career advice, and to my adviser Dr. Michael S. Kearney for his continued patience. I am grateful to the late Dr. David Jonathan Slater, for his friendship and his kind prodding that got me started. Drs. Charles L. Walthall and Martha Anderson at US Department of Agriculture provided input and support early in this project. Around the same period, Drs. Richard T. Field and Victor V. Klemas at the University of Delaware also provided useful dialogue and suggestions regarding spectroscopy and remote sensing in coastal marshes. Drs. Curtis D. Mobley, Zhongping Lee, Gerhard Meister, Ziauddin Ahmad, Andres Kuusk, K. Fredrick Huemmrich, and Vern C. Vanderbilt also provided helpful discussions and input regarding the field of radiometry. Dr. Steven R. Schill provided his marsh canopy reflectance spectrum measurements and supporting information, which given the amount of data involved was not trivial, and Dr. Elijah Ramsey III provided invaluable leaf reflectance data. I owe special thanks to Dr. Patrick L. Coronado for his generous support of my field work, to Dr. Wenge Ni-Meister for lending her hand-held

spectrometer during my first field campaign, Dr. Stanford Hooker for the use of a gray reference panel that made calibration much easier, and Mr. Milton Hom, for his invaluable help with instruments, and Dr. Antonio Mannino for his input toward my field program. Dr. Elizabeth M. Middleton and Mr. Lawrence A. Corp at GSFC provided useful opportunities for field work experience. I am likewise grateful to Dr. David R. Tilley and his team, who amongst many things taught me to walk on the marsh - a skill that cannot be overvalued in this field. The US Fish and Wildlife Service (USFWS) facilitated access to the transect experiment study site and provided useful data regarding the local wetlands. The USFWS staff was very kind, but I would like to particularly thank Drs. Rodger Stone and Dixie Birch for their support. Finally, Dr. Roman V. Jensien of the Maryland Coastal Bay Program and Mr. James W. Charland, at the time the Assateague Coast Keeper, gave tours of the coastal bays of Maryland and provided insightful information about threats to these precious ecosystems in Maryland. Without all these and numerous other sources of input and support, this project would surely have *withered before any other herb*.

Table of Contents

List of Tables

List of Figures

decrease significantly for large zenith angles as the transmittance across the air-water interface decreases.

Figure 2-6. Selected BRDF reflectance response as calculated with Equation 22. Rows are associated with zenith angles of an incident beam of light and columns give different values of σ, which represent surface roughness. The disks show the distribution of the reflected light over the hemisphere, following the projection indicated by the diagram in the lower lefthand corner. Light enters from the left and the principal plane is horizontal and perpendicular to the page. The graded color bar gives the numerical meaning of the color in the disks. The reflectance r_d is set to 0.1 in this example. The colors at the very ends of the bar include values that exceed the numerical range indicated. The decrease of the reflectance distribution along the horizon (disk's edge) is caused by the diffuse component roll-off caused by the decreased transmittance across the air-water interface at high zenith angles. Note that by reciprocity, replacing the incident light direction with the observation direction will produce the same distributions.

Figure 2-7. Look-up table for the specular component of the directional-hemispheric or hemispheric-directional reflectances. As calculated by the second term of Equation 24, this table is a function of zenith angle and surface roughness, σ. The values in the plot above show this reflectance quantity divided by π. The intersection of the blue curves indicate points that are used in the look-up table for the aquatic background model.

Figure 2-8. The aquatic background albedo. The aquatic background albedo is primarily a function of the reflectance below the air-water interface, as illustrated in a. Surface roughness has little effect albedo as shown in b (r_d is set to 0.1 in this example).

Figure 2-9. The response along the principal solar plane of the full marsh vegetation model. Shown is the variation to a) the surface roughness σ and to b) to LAI. In this case, the 45° solar zenith angle and wavelength is 920 nm.

Figure 3-1. The five spectra used in the LAI retrieval test and their corresponding Price function fits. The Default Soil spectrum is the expert guess for the soil spectrum used by the default configuration of ACRM. Dry Marsh Soil and Wet Marsh Soil spectra were taken from marsh soil samples, the latter being nearly saturated. The Turbid Water spectrum is the same as the modeled spectrum in Figure D-3.

Figure 3-2. The ACRM and WCRM modeled relationship between LAI and canopy reflectance. The relationship is shown for several sensor zenith angles along the solar principal plane at a) 486 nm and b) 572 nm. Solar zenith angle was set to 45° for both models. The default soil was used for ACRM. WCRM was run with $\beta = 1$ and $\sigma = 0.06$.

Figure 3-3. The ACRM and WCRM modeled relationship between LAI and canopy reflectance. The relationship is shown for several sensor zenith angles along the solar principal plane at a) 661 nm and b) 838 nm. Solar zenith angle was set to 45° for both models. The default soil was used for ACRM. WCRM was run with $\beta = 1$ and $\sigma = 0.06$.

Figure 3-4. Box-whisker plot for the LAI retrieval for five modeling cases based on background spectra shown in Figure 3-1. The upper and lower extremes of the whiskers are the minimum and maximum, respectively. The bottom and top of the box indicate the lower and upper quartiles. The horizontal line near the center of the box is the median. The retrieval base on the blue reflectance has stuck on the initial value for LAI, which was set to a possibly questionable value. The actual value may be closer to the retrieval values based on the NIR reflectance.

Figure 3-5. Variation in the retrieved LAI in response to variation introduced to the reflectance field. The retrieval of LAI is based on monochromatic, multiangular reflectances for two representative wavelengths for blue and NIR. See text for details of the experimental procedure. Noise level is the standard deviation of the introduced random values divided by the overall range of reflectance values along the SPP in the backscatter direction. Each symbol indicates the standard deviation of the relative difference between the original LAI value and the retrieved values. The curves are 2nd order polynomial fits.

Figure 4-1. Transect Study Site. Green and blue pennon markers indicate positions of LAI measurements for the long transect experiment. Yellow curve shows the segment of Maple Dam Road traverse during the same experiment. Red boxes indicate where LAI and reflectance were measured for three sites as part of the short transect experiment, each identified with numbered red circles. (Inset: Dept of Commerce, via Wikimedia Commons)

Figure 4-2. Transect experiment apparatus.
1. OOI Gershun tube probe with 14° aperature.
2. Canon Digital Ixus camera (WiFi enabled).
3. Protractor.
4. Optical fiber, 500 μm thick, 20 m long.
5. Instrument probe mount.
6. Extendable boom, 5.2 m, max 6.7 m.
7. Guy cables.
8. Boom mast.
9. GPS unit and cable.
    a. 2007 - Garvin Etrex.
    b. 2008 - GlobalSat Tech Corp BU353 USB GPS Receiver.
10. Boom mask platform, OOI USB2000+ Spectrometer, computer console.
11. LI-COR LAI-2000 Canopy Analyzer with control unit and caps.

Figure A-2. Illustration showing the geometric convention used for the unit vectors and their zenith and azimuth angles.

Figure D-1. Shallow water absorption spectra components. Shown are total absorption and the absoption spectrum for water, a_w, phytoplankton, a_{ph}, for CDOM, a_{CDOM}, and for non-algal particles, a_{NAP}. As an example, C_a is set to 3 mg m-3 for the calculation of a_{ph}.

Figure D-2. Total scatter coefficients. Shown are total scatter coefficients for water, b_w, and particles, b_p, and backscatter co-efficient, b_b, where $\Re = 5$ and $C_a = 3$.

Figure D-3. Reflectance spectra for deep turbid water and and turbid water with submerged leaves near the surface. In this example, $H = 25$ cm, $C_a = 3$ mg m^{-3}, and SPM = 0.3 g m^{-3}.

Figure E-1. Calculation flow diagram. This diagram shows how the main components work together. The gray area includes components that were originally part of the original ACRM model. Above or below each component are shown its input parameters, which are defined in Table E-1. The parameter C_{ar}, the concentration of leaf carotenoid pigments, was not included in this study because ACRM uses the PROSPECT 3 model. Future updates to the model should include PROSPECT 5, which includes C_{ar}.

Figure E-2. Hierarchical structure diagram. This diagram shows the relationship of the new aquatic background code modules to the original ACRM code. The smcrm subroutine drives all calculations for the ACRM and WCRM models. The original subroutines dif2 and biz2 handle the diffuse and direct streams, respectively. These routines were adapted to call new modules related to the aquatic background. Other various subroutines, including the modules for leaf optics (PROSPECT and LIBERTY), sky spectrum, and the various higher level driving routine are not shown because no more than superficial changes were made to these routines. External calculations that are indicated are not listed in this document.

List of Acronyms

ACRM	Canopy reflectance model developed by A. Kuusk
AVIRIS	Airborne Visible and Infrared Imaging Spectrometer
BRDF	Bidirectional Reflectance Distribution Function
BRF	Bidirectional Reflectance Factor
CCD	Charged Coupled Device
CDOM	Chromophoric Dissolved Organic Matter
DC	Dark Count
EDT	Eastern Daylight Saving Time
FORTRAN	FORmula TRANslation, a programming language
GPS	Global Positioning System
IFOV	Instantaneous Field of View
LIBERTY	Leaf Incorporating Biochemistry Exhibiting Reflectance and Transmittance Yields
MESMA	Multiple Endmember Spectral Mixture Analysis
NASA	National Air and Space Administration
NDVI	Normalized Difference Vegetation Index
NIR	Near Infrared
PROSPECT	PROperties Optique SPECtrales des Feuilles
PVC	Polyvinyl Chloride
RMSE	Root Mean Squared Error
SAIL	Scatter from Arbitrarily Inclined Leaves
SCM	Spectral Cross-correlation Measure
SFG	Sandmeier Field Goniometer
SPM	Suspended Particulate Matter
SPP	Solar Principal Plane
TOC	Top of Canopy
USDA	US Department of Agriculture
USGS	US Geological Survey
WCRM	Wetland Canopy Reflectance Model

Chapter 1 Introduction

A state of inundation produces unique specular and spectral characteristics in the inundated tidal marsh canopy. Such an aquatic substrate can affect conventional attempts to retrieve canopy characteristics, such as structure information (e.g., canopy height, leaf area index, etc.) or plant species composition. The reflectance characteristics of such a background can also influence spectral analysis of plant characteristics based on hyperspectral data. A model to account for the effects of inundation would be useful to understanding spectral field measurements and remote sensing of this type of surface cover. To that end, an existing vegetation canopy reflectance model is combined with an aquatic background model to account for the effects of an aquatic substrate on the top-of-canopy bidirectional reflectance. The aquatic background model itself was based on first-principle models of water reflectance. The aquatic background reflectance model is also developed as a combination of two models: one to predict specular reflectance of a slightly roughened water surface and a shallow water model to handle diffuse specular reflectance from just beneath the water's surface. The combined vegetation canopy and aquatic background reflectance model is then used to understand specular and spectral characteristics of an inundated canopy.

The chapter addresses the overall value of the target biome and the importance of remote sensing to understand and manage this resource. Then the issues of remote sensing vegetation with aquatic background are discussed and an enhanced model approach is proposed. The chapter concludes with a selection of a particular model for use in the study.

Chapter 2 reviews the theory behind the calculations that are used to model the aquatic background optics. This defines the quantities that are calculated and describes how they are used with the vegetation canopy reflectance model. Two primary components are included in these calculations. First, specular reflectance of the water's

surface is modeled using a roughened Fresnel reflectance, following the approach of Cox-Munk (Cox and Munk, 1956). Second, the diffuse reflectance beneath the surface is obtained through a shallow water model taken from the literature (Lee*, et al.*, 1998; 1999). The latter component is the main driver of the specular characteristics of the aquatic background in non-specular directions. Further details of the implementation of these calculations as computer code are given in Appendix E.

Chapter 3 discusses retrieving *leaf area index* (LAI), where LAI is defined as the ratio of single-sided leaf area to horizontal ground area and is a key structure parameter used in describing canopy dynamics and processes. More specifically, the chapter focuses on the sensitivity of LAI retrievals via the canopy reflectance model to background conditions. The relationship between LAI and canopy reflectance is modeled for various sensor angles and wavelengths to identify conditions where there is potential for retrieval of LAI from measured canopy reflectance using model inversion. The behavior of the inversion algorithm when the LAI dependency on canopy reflectance breaks down is also discussed. This chapter sets the groundwork for understanding the model's applicability and limitations prior to its employment with field data.

Chapter 4 describes a field experiment where LAI data and canopy reflectance data taken at multiple angles were averaged over transects for three different marsh canopies. The transects were at a length that would be similar in spatial scale to pixels collected by some spaceborne remote sensing imager (e.g., Landsat). The averaged LAI was used to predict the multi-angular canopy reflectances using the new model, which qualitatively compares the averaged reflectance measurements. Challenges for application of this method for marsh canopies are discussed.

Chapter 5 describes an experiment where the original and enhanced canopy reflectance models are used to predict the canopy reflectance field of a marsh that was heavily sampled data over various viewing and illumination angles. The results show that the enhanced model affords an improvement by reducing biases from specular

reflectance at visible wavelengths. Then, cross correlation analysis of the data and canopy reflectance models with leaf reflectance data is used to indicate viewing and illumination angles that are preferential for reducing the influence of the background reflectance on the vegetation signature in the canopy reflectance.

Chapter 6 discusses how the model can be used to simulate a field experiment where the nadir canopy spectral reflectance was measured as the water level within the canopy was artificially raised. The results show that the aquatic background model can explain the spectral signature seen in the data. The results also provide an example of how the aquatic background can produce non-linear mixing of vegetation and water spectral signatures when vegetation becomes submerged. Using the marsh reflectance model to simulate the experiment also shows that the mixture of chlorophyll and water absorptions, along with the high near-infrared (NIR) reflectance of submerged leaves, produce a spectral feature that could complicate measurements of the canopy red-edge.

Chapter 7 provides some synthesis of the results and observations pertaining to the model development and working with field data. This begins with a summary of the project and discussion regarding the results and their implications. This is followed by a discussion of the potential applications, limitations, and future work for the enhancement model. The overall assessment concludes that the enhanced model could offer a potential method for LAI retrieval from above-canopy remote sensing but further work is needed to improve the vegetation canopy reflectance handling of multi-scatter effects in the NIR. However, the enhanced model did explain the spectral features of an inundated canopy and could have other applications, such as building spectral libraries. Also, application of the model to remote sensing imagery may require further work in developing a model to account for the high variable spatial distribution of vegetation, open water, and wet soil.

The Importance of Coastal Marsh Systems

Marshes are a vital part of the coastal ecosystem and provide a number of important ecological services, including improving estuarine water quality; providing food and resources for avian, piscine, mammal, and invertebrate populations; and providing materials and food for agricultural use. Marshes also help control erosion and dissipate wave energy from storms. Upland estuarine marshes can store flood water protecting coastal human populations and their property. They are also valued for their natural beauty and provide resources for human recreation (Barbier*, et al.*, 2011; Bromberg-Gedan*, et al.*, 2009). Given these services, Bromberg-Gedan et al. (2009) calculated an average annual value of $14,397 per hectare per year for the world's tidal marshes, based on the 2009 inflation-adjusted value derived by Constanza (1997).

Coastal marshes have been used by humans for centuries to provide raw materials and food for livestock , such as harvesting *Spartina patens* (saltmeadow cordgrass or salt marsh hay) for animal fodder or *Phagmites austalis* (common reed) as thatch for roofing (Bromberg-Gedan*, et al.*, 2009). They are also valuable as open space, as food sources and habitats for breeding marine and estuarine fauna (Hughes, 2004), including mammals, birds, fish, and invertebrates (e.g., mollusks and crustaceans). In particular, marshes are known to provide important support to bird populations (Hughes, 2004) and provision fisheries (Boesch, 1984) that supply commercial and recreational fishing (Bell, 1997). In fact, 90% of the world's catch of fish depends on tidal marshes (UNEP, 2006).

Coastal and estuarine marshes are ecotones that play a major role in biogeochemical cycling between terrestrial and marine biomes. Coastal marshes function as sinks for sediments, nutrients, and pollutants from rivers and runoffs (Cebrian, 2002; Day, 1989). In this sense, coastal marshes have been referred to as the "kidney of the landscape" (Cox, 2002, page 5). Coastal wetlands remove nitrogen from surface water, mostly in the form of NO_3 and outputs N_2O to the atmosphere as a result of denitrification. Through the removal of N and sediment, coastal marshes provide the

valuable ecological service of maintaining estuarine water quality and reducing eutrophication and subsequent hypoxia in estuarine waters. Coastal wetlands are also the most productive regions in coastal watersheds and export carbon to nearby marine ecosystems (Adam, 1990; Cebrian, 2002). These systems uptake carbon, which is output to the atmosphere as CO_2 and CH_4 through respiration and decay processes, and export carbon to estuarine systems in the form of suspended organic carbon, including humic and fulvic acids. A personal observation made while in the field was that a substantial amount of the above-water carbon stock could be released to the atmosphere as a result of season or prescribed burning, and possibly flushed into estuarine waters or buried in marsh soils as soot and ash. Marshes keep a large carbon pool in their soil. For example, soil carbon pools range from one to several hundred metric tons of carbon per hectare in the marshes along the Gulf of Mexico. Likewise, in Gulf of Mexico marshes, the soil carbon pool accumulates, on average, a few percent per year. Eventually, this carbon pool can be sequestered as a result of soil accretion. On an areal basis, these wetland systems may be more valuable than any other as carbon sinks because of their high sequestration rate (Engle, 2011).

Coastal marshes also serve as buffers against the sea, dissipating 90% of incident wave energy, while their root systems stabilize sediment from erosion. Furthermore, the absorbed energy stimulates sedimentation and helps many salt marshes to keep pace with relative sea level rise (RSLR) (Zanuttigh, 2011), which could reduce further land loss and erosion. In fact, marshes can significantly protect inland human assets and coastal land from severe storms. Such disturbances can result in considerable loss of marsh vegetation. For example, hurricane Katrina transformed about 100 mi^2 of coastal marsh into open water (Klemas, 2009). However, there is evidence that damage further inland may have been worse without those marshes (Gedan*, et al.*, 2011). Furthermore, upland marshes can offer water storage volume during spring tides or high river discharge thus limiting flooding in coastal cities and towns (Barbier*, et al.*, 2011).

Coastal Wetland Threats

Changes in coastal wetlands can interfere with these essential functions and services they provide (Klemas, 2001). Being vulnerable to anthropogenic disturbances and climatic change, this valuable resource has undergone considerable degradation. Globally, around half of the original salt marsh ecosystems have been degraded or lost, and in some areas, such as the West Coast of the USA, the loss is as much as 90% (Barbier*, et al.*, 2011). The USGS estimates that 85,000 acres of emergent estuarine wetlands in the USA were lost between 2004 and 2009 with a loss rate that was three times higher than the period from 1998 and 2004 (Dahl, 2011). 83% of that loss was to open water stemmed from coastal storms, land subsidence, RSLR, or other ocean processes, which could be tied to anthropogenic and natural processes. These losses undermine the function and services that coastal marshes provide (Barbier*, et al.*, 2011).

Historically, marshes have been exploited for their material goods and used for livestock grazing, which can alter the marsh ecology. Coastal wetlands are being converted to salt works in western Australia (Adam, 2002), a practice that in the early 20th century severely degraded marshes in California. Coastal marshes have also been lost through land reclamation to support agriculture or urban growth (Lotze, 2006) or degraded by manmade changes to hydrology, such as damming, diking, or ditching through human construction (Bromberg-Gedan*, et al.*, 2009).

Introduction of invasive destructive plant and animals species has severely impacted marshes worldwide. Natural or anthropogenic changes in watershed ecology, e.g., removal of high level predators, can lead to runaway herbivory that can denude marshes. Significant expanses of marshland have been severely degraded by geese, herbaceous crabs or snail (Bromberg-Gedan*, et al.*, 2009). Some spontaneous and unexplained marsh dieback has also been observed in marshes of the Gulf of Mexico and along the eastern seaboard of the USA, which could be tied to drought, predation (Bromberg-Gedan*, et al.*, 2009), excessive submergence (Kearney and Riter, 2011; Webb

and Mendelssohn, 1996; Webb*, et al.*, 1995). However, the etiology of many cases of the recently observed phenomenon of "sudden dieback" remains largely unknown (McKee*, et al.*, 2004; Ogburn and Alber, 2006).

Climate changes could also be affecting marsh systems and lead to further degradation. Increased CO_2 levels and temperature changes may change the current distribution of C3 and C4 plants (Bromberg-Gedan*, et al.*, 2009). Most marshland grass species are C4 plants and are not expected to increase productivity under higher CO_2 levels, but that is probably not the case for C3 plants (Erickson*, et al.*, 2007), which include many of the marsh sedges and rushes. Rising temperatures from global warming may bring invasion of warmer water species into colder zones (Zomer*, et al.*, 2009). RSLR also endangers these systems through increased inundation and drowning of plants, salt water incursion, and increased vulnerability to storms. As sea level rises because of subsidence or global warming, marshes of the supralittoral zone can be squeezed out, between the sea and adjoining coastal defenses or agricultural land (Titus, 1998; Zanuttigh, 2011). Thus monitoring marshland coverage is important to understand the affects of climate change on coastal watershed and estuarine biogeochemical cycling.

Monitoring, Assessment, and Remote Sensing

Efforts have been made to assess and monitor coastal marshes in order to improve our understanding of their essential services and to aid in their management (Dahl, 2011; UNEP, 2006). Part of the process of managing degradation of coastal marsh services includes identifying changes in marsh systems that would affect these services (Barbier*, et al.*, 2011). Studies of changes in ecological function and response are often limited to a small number of plots and scientists must extrapolate findings to regional scales. Although monitoring widespread changes to these landscapes could assist researchers and policymakers in assessing and monitoring marsh deterioration or restoration, limited accessibility makes large-scale, *in situ* evaluation challenging (Seher, 1973). Remote

sensing techniques offer an efficient approach to quantify changes in marsh vegetation (Klemas, 2011a; 2011b). The utility of remote sensing techniques has been explored for measuring quantities over large regions of wetlands, such as species and cover type (Artigas and Yang, 2005; Jensen*, et al.*, 1986; Jollineau and Howarth, 2008; Judd*, et al.*, 2007; Schmidt and Skidmore, 2003; Silvestri and S., 2003; Underwood*, et al.*, 2006; Zomer*, et al.*, 2009), canopy density or LAI (Sone*, et al.*, 2009; Wang*, et al.*, 2007; Xavier and Vettorazzi, 2004; Xiao*, et al.*, 2002), or quantities related to plant production and stress (Klemas, 2001; Mendelssohn*, et al.*, 2001; Ramsey and Rangoonwala, 2006; Tilley, 2003; Vaesen*, et al.*, 2001; Zhao*, et al.*, 2009). However, the optical properties of an inundated canopy can present new challenges for some of these techniques.

Unique Nature of Remote Sensing in Marshes

Marsh remote sensing depends on the spectral reflectivity of the vegetation canopy and its aquatic substrate. The canopy structure and its substrate affect reflectance with changing viewing and solar angles. Reflectivity that changes as a function of these angles is more generally defined as the bidirectional reflectance distribution function (BRDF). The form of the BRDF can also vary with the wavelength of the incident light, thus changing spectral characteristics of the canopy reflectance when measured at different angles (Sandmeier*, et al.*, 1999). Thus spectral variation of the BRDF directly affects remote sensing techniques for retrieving marsh canopy characteristics, such as species composition, aerial biomass, or indicators of plant stress. Since airborne and spaceborne remote sensing imagers measure over a large range of viewing angles and solar angles, this effect could be a challenge for existing techniques that are dependent on canopy spectral features.

In general, reflected light from materials found at the bottom of canopy can strongly influence remote sensing of vegetation canopies (Gemmell, 2000; Gemmell and McDonald, 2000; Goward and Huemmrich, 1992; Huemmrich and Goward, 1997).

Experience has shown that the background can have an overwhelming influence in marsh vegetation spectroscopy, which includes but is not limited to substances like water, mud, sand, detritus, bacterial mats, and algal growth (Field, 2006 - personal communication). The presence of an inundated substrate can complicate ground cover classification techniques (Brown de Colstoun and Walthall, 2006). Kuusk (1998) reported that retrieval of canopy characteristics from the inversion of a terrestrial vegetation model failed for *Phragmites austalis* because of the presence of water. In reporting their work on mapping invasive species of marshes, Underwood et al. (2006) also noted that variation in water turbidity alone reduced the accuracy of classification for certain species by 10 to 60%. Influence of the aquatic background presents a significant challenge for remote sensing of marshes.

The aquatic substrate contributes strongly to both directional and spectral features in the top of canopy (TOC) reflectance. Vanderbilt et al. (2002) demonstrated that the directional specular solar reflectance produces a signature for inundated canopies that is distinct from both canopies with a dry substrate and from open water. Essentially, the specular reflectance causes a second "hot spot" on the solar principal plane in the forward scatter direction. In fact, they exploited this directional feature to successfully distinguish inundated canopies from dry ones using an airborne multi-angular, multi-spectral radiometer. Interestingly, Vanderbilt and collaborators from the University of California at Davis, have performed more recent, detailed characterization of coastal wetlands in California based on sun glint (Ustin, 2006 - personal communication). Still, given that remote sensing instruments used for, *inter alia*, classification are often pointed at nadir, with measurements taken near solar noon, there is a potential impact of strong specular reflectance off water from the sun or sky that could adversely affect standard methods.

Spectral effects of water reflectance have also been studied for the marsh canopy. In 1995 and 1996 field experiments, Stutzer (1997) measured the nadir TOC reflectance spectra for three marsh species, *Schoenoplectus* (formerly *Scirpus*) *americanu*s, *Spartina*

patens and *Spartina cynosuroides*, while varying inundation levels. His results showed that increasing water level causes a profound change in the nadir reflectance spectrum, marked by a dramatic decrease in the Near Infrared (NIR) reflectance because of high water absorption. In addition, features that are uncharacteristic of either ground or vegetation spectra appear in the canopy reflectance spectra as the canopy became submerged, suggesting the domination of specular reflectance from the water surface. For instance, although it is not noted in his thesis, there is a dip in reflectance in a large region around 760 nm, which could be attributed to water absorption features. In general, his results demonstrate that water, which is highly variable (i.e., driven by tidal and weather related events), can affect remote sensing applications that depend on TOC spectral features at optical wavelengths. Since many species in the marsh are most distinguishable at the red to NIR region of the spectrum (Artigas and Yang, 2005), the spectral influence of water optics is a significant consideration for species classification, as well as other remote sensing applications.

Historically, efforts to correct for the influence of the BRDF have been strictly empirical and narrowly focused. For instance, Gross, Hardisky, and Klemas (1988) empirically derived a statistical correction for sun angle to estimate aerial biomass using field spectroscopy. However, this was specific to the *Spartina alterniflora* species at a single viewing angle. In addition, Miyamoto et al. (2001) also used multi-angle spectroscopy to improve classification of marsh plant species over single nadir measurements. Although those results are tantalizing, the work was very limited in scope and detail, and being entirely empirical, they provide little nomothetic knowledge of radiative transfer processes that could feed into general or global applications in marsh remote sensing. After an intense effort to empirically characterize the BRDF for *S. alterniflora*, Schill and Jensen et al. (2004) recognized that a more extensive scope was needed. They called for the development of a BRDF model for coastal marsh canopies to improve estimates of surface reflectance and albedo, to identify spectral bands that are

least affected by BRDF, to find optimal viewing and solar angles for data collection and to adjust remote sensing imagery for the effects of BRDF. In addition, canopy characteristics could potentially be retrieved from the inverse of this model and remote sensing data.

An Enhanced Canopy Reflectance Model for Marsh Applications

In this study, an existing canopy reflectance model is enhanced to account for the optical influence of an aquatic substrate by coupling it to an aquatic background reflectance model. The aquatic background reflectance model is also developed as a combination of two models: one to predict specular reflectance of a slightly roughened water surface and a shallow water model to handle diffuse specular reflectance from just beneath the water's surface. The modeled relationship between LAI and canopy reflectance is examined for the combined vegetation and aquatic substrate models, and for the canopy reflectance model with its default soil reflectance model. This provides insight into how marsh conditions affect the retrieval of LAI using remotely sensed canopy reflectances. Comparisons of the model to field transect data help identify where the vegetation canopy model can be challenged by canopies populated with some marsh species. It is also shown that the addition of an aquatic background model reduces biases in canopy BRDF prediction that are caused by specular reflectance. The enhanced canopy model is also used to explain how the optical properties of the aquatic substrate can affect the marsh canopy spectral features. This is of particular interest because it could relate to hyperspectral and spectral index techniques.

Chapter 2 Adaptation of a Canopy Reflectance Model for an Inundated Canopy

Introduction

This chapter describes the adaptation of a canopy reflectance model for emergent vegetation in a coastal marsh, hence referred to as the Wetland Canopy Reflectance Model, or WCRM. As marsh vegetation is optically comparable to its counterparts on dry land, the approach is to modify an existing canopy reflectance model for terrestrial vegetation to account for the aquatic background. The optical characteristics of the aquatic background differ from dry land in two key distinct ways. First, the air-water interface is a Fresnel reflector, which can produce significant specular reflectance. Furthermore, although the water's surface beneath vegetation is much smoother than open bodies with a greater fetch (Vanderbilt*, et al.*, 2002), it is not mirror smooth, thus some consideration of dispersion of the upwelling light from direct illumination is considered. Second, the water column beneath the air-water interface, along with its dissolved and suspended constituents, are characteristically different from unsaturated soil. To account for this, a shallow water model is employed to produce diffuse reflectance spectrum. Together, these specular and diffuse components are combined to calculate the key properties of an aquatic background beneath vegetation (see Figure 2-1).

Light from the sun and sky works its way through a medium of vegetation to reach the underlying inundated substrate. Along its downward path, it is reflected upward, transmitted downward, or absorbed by the vegetation (e.g., leaves, stems, etc.). The remaining light that finally reaches the bottom is likewise reflected upward or absorbed. The amount of light that is reflected upward at any given point by leaves or substrate depends on the reflectance spectrum of these components. The transmission of

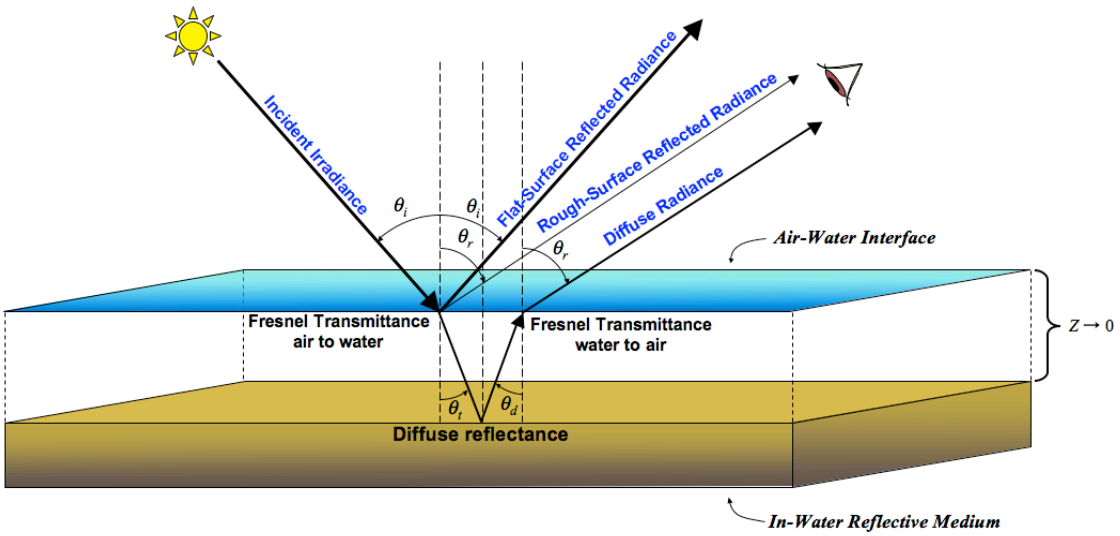

Figure 2-1. Key components for the aquatic background reflectance model. The aquatic background model is based on a diffused reflector at depth Z, as Z approaches zero. This produces a specular component from the air-water interface and a diffuse component stemming from an assumed isotropic reflectance condition beneath the surface. Most of the specular radiance is reflected upward at angle θ_i, but any roughening of the surface (e.g., capillary waves from wind disturbance) would redirect some specular radiance in the direction of the observer.

light through leaves or water at any given wavelength also depend on the optical properties of these components. Furthermore, the amount of light that can pass to the bottom or make its way to an observer in some direction depends on the density and orientation of leaves (Verhoef, 1984). Hence, the LAI or leaf angular distribution (LAD) are important structure parameters in determining the flow of light for given illumination and viewing directions.

To calculate these various flows, a common practice is to consider both the direct and diffuse flows of radiation onto and through the canopy. The direct stream of radiation begins with the highly directional beam of light from the sun, while the diffuse stream can start with light from the sky. Direct light propagates through the canopy until it encounters material that will scatter it in some new direction. If the scattering optic element is not a specular reflector or transparent, the scattered light partially or fully

enters the diffuse stream of light. The various upward and down streams are illustrated in Figure 2-2.

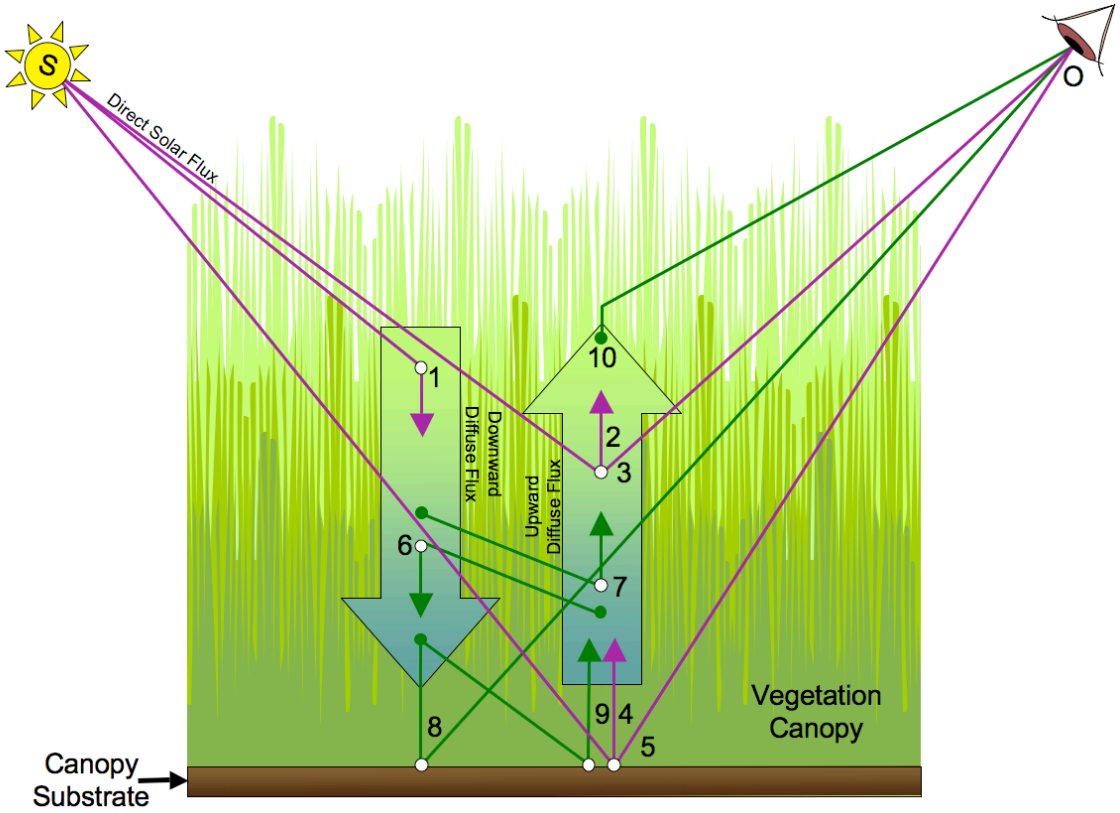

Figure 2-2. Diagram illustrating the principal fluxes of a vegetation canopy reflectance model. Illustrated are the fluxes that can be calculated within a one-dimensional canopy reflectance model. Magenta lines indicate pathways that are fed by direct flux, while the green lines show the pathways of diffuse flux. White circles indicate switch points in the flux pathway (e.g, from a reflectance event). The direct solar flux enters the diffuse downward flux (1) and diffuse upward flux (2). The direct solar flux also undergoes single scatter events that redirect light straight to the observer from the canopy (3) and from the surface (5). The direct solar flux is also reflected of the surface and introduced into the diffuse upward flux (4). The upward diffuse flux is also reflected off of canopy leave back into the downward flux (6) and the reverse is true for the downward flux (7). The downward diffuse flux is also reflected off of the surface and can directly reach the observed through the foliage (8) and can also be reflected into the upward diffuse flux (9). The upward diffuse flux is also observable as that flux escapes the canopy through gaps in the foliage (10).

The Vegetation Canopy Reflectance Model

The reflectance model chosen for the vegetation component of the marsh reflectance model was originally published by Kuusk in 1995 and 1996 and designated ACRM. ACRM was shown to effective in remote sensing applications for terrestrial vegetation canopies, with better correlations with ground measures of LAI than several well known spectral indices (Houborg*, et al.*, 2009; Houborg and Boegh, 2008; Houborg*, et al.*, 2007; Weihs, 2008). This model includes many of the calculations found in other canopy reflectance models in the literature that pertain to a one dimensional turbid medium model (Pinty*, et al.*, 2001; Pinty*, et al.*, 2004). The original vegetation canopy model combines the direct radiative flow of an enhanced version of the Nilson-Kuusk (N-K) model (Nilson and Kuusk, 1989) with the four-stream approximation of diffuse fluxes of the Scatter from Arbitrarily Inclined Leaves (SAIL) model (Verhoef, 1984). The enhancement of the former component includes a parameter, based on Markov probability, to account for correlation in gaps between canopy layers (Kuusk, 1995b). Both of these components are combined into a computationally efficient canopy reflectance model (Kuusk, 1995a; 1996). Details of the calculations in ACRM are given in both Kuusk's 1995 and 1996 publications. As another benefit, the code supporting the ACRM algorithm was also developed to calculate the inverse of the ACRM algorithm, i.e., estimating input vegetation parameters given measured reflectance values, making it more readily useful for remote sensing applications. Finally, but no less important than the other consideration, the code is freely available from the author.

The ACRM model also includes the third version of the model called Properties Optique Spectrales des Feuilles (PROSPECT) to estimate the leaf reflectance and transmittance (Jacquemoud and Baret, 1990). This model supports remote sensing application of the vegetation canopy reflectance model by reducing the need for *a priori* knowledge of leaf optical properties. PROSPECT uses relative amounts of chlorophyll *a* and *b*, brown pigment, dry matter, water content, and a structure parameter that

modulates the internal leaf complexity. Thus, fewer parameters are required when predicting the canopy BRDF or when inverting the canopy model to retrieve canopy structure.

ACRM estimates the angular distribution of the substrate bidirectional reflectance factor (BRF) using a polynomial soil model developed by Walthall et al. (1985). This relies on predefined empirical coefficients, so the angular properties of the soil component requires no input parameters. ACRM also defines the soil reflectance spectrum using four Price functions, which essentially forms four-vector basis (Kuusk, 1995a; 1996) that can describe the spectral characteristics of many dry soils. The soil spectra modeling was based on the work of Price (1990), who developed a four-vector basis to describe 500 measured soil spectra. The modeled soil spectrum, therefore, requires values for four coefficients to describe the soil beneath a canopy of interest. Default values for these coefficients are provided with the software. Also by default, the first two Price coefficients are varied when inverting the model to get canopy structure characteristics (e.g., leaf area index). In this way, ACRM attempts to account for the spectral reflectance of the soil substrate when retrieving properties of the canopy using measured reflectances.

Defining Surface Reflectance Quantities

To create a marsh canopy reflectance model, the interactions between the direct and diffuse streams must be considered. The canopy substrate reflects the direct flux upward into direct and diffuse streams towards an observer. Likewise, the diffuse stream is also reflected diffusely or directly. These four possible interactions are governed by four reflectance quantities, which the new model must calculate for the an aquatic substrate. In ACRM, these four different reflectance quantities include the surface BRF, the hemispheric-directional and directional-hemispheric reflectances, and the bi-hemispheric reflectance for an isotropic illuminating radiation field (also known as the

albedo) (Nicodemus*, et al.*, 1977; Schaepman-Strub*, et al.*, 2006). As many different definitions for reflectance exist, using consistent definitions is essential to coupling a new aquatic reflectance model with the vegetation canopy reflectance model. Thus, this section will define these quantities, which will be used throughout this thesis.

Serving as a foundation for all four definitions, the BRDF is an important inherent optical property of the surface and is defined as the instantaneous quantity:

$$f(\theta_i,\phi_i,\theta_r,\phi_r) = \frac{dL_r(\theta_r,\phi_r)}{L_i(\theta_i,\phi_i)\cos\theta_i d\Omega_i} \qquad \text{Eq. 1}$$

where L_i is the radiance of the light source, dL_r is a differential element of the reflected radiance (Nicodemus, 1963), $d\Omega_i$ is the differential solid angle in the direction of the light source, θ_i is the angle measured from the zenith direction to an incident beam of light, while ϕ_i is the angle of the same beam direction as measured around the surface plane from the x-axis. θ_r and ϕ_r are the corresponding angles giving the direction of reflectance towards an observer (Nicodemus*, et al.*, 1977). The BRDF, as defined in Equation 1, is used to calculate all four reflectance quantities used by the vegetation canopy reflectance model.

The first reflectance quantity, namely the BRF, is used specifically to determine the amount of specular flux that is reflected from the surface into the direct flux going through the vegetation toward the observer. This can be related to the BRDF through the calculation,

$$\rho(\theta_i,\phi_i,\theta_r,\phi_r) = \pi f(\theta_i,\phi_i,\theta_r,\phi_r) \qquad \text{Eq. 2}$$

This quantity is often used in the literature, as it is commonly measured in the field using reference panels (Schaepman-Strub*, et al.*, 2006). In the description of the ACRM calculations (Kuusk, 1995a; 1996) the quantity $\rho_{soil}(\theta_i,\phi_i,\theta_r,\phi_r)$ is based on the BRF

calculation for soil developed by Walthall et al.1985). This quantity will be combined with the corresponding quantity for water, $\rho_{water}(\theta_i,\phi_i,\theta_r,\phi_r)$, to yield the total BRF of the aquatic background, which is denoted as $\rho_{aquatic}(\theta_i,\phi_i,\theta_r,\phi_r)$.

In the description of ACRM calculations, the soil directional-hemispheric reflectance, $\rho_{soil}^{(sd)}(\theta_i,\phi_i)$, defines the portion of flow from specular flux that is redirected at the dry ground into the upward diffuse flux. It should be noted that this definition of hemispheric reflectance is different from definitions found in the aquatic literature because it assumes an isotropic irradiance field (Mobley, 1994). Thus, this quantity is computed for interaction with the vegetation canopy reflectance model as,

$$\rho^{(sd)}(\theta_r,\phi_r) = \int_{\Omega_+} f\left(\theta_i,\phi_i,\theta_r,\phi_r\right)\cos\theta_r d\Omega_r \qquad \text{Eq. 3}$$

where $d\Omega_r = \sin\theta_r\, d\theta_r\, d\phi_r$ is the differential solid angle in the direction of reflectance and Ω_+ is the entire upward directional hemisphere (i.e., the set of all upward solid angles). Similarly, the hemispheric-directional flux, $\rho_{soil}^{(do)}(\theta_r,\phi_r)$, gives the amount of downward diffuse flux that is reflected directly toward the observer. The same assumption of irradiance isotropy is used in the formulation of the hemispheric-directional reflectance, which is thus computed as,

$$\rho^{(do)}(\theta_r,\phi_r) = \int_{\Omega_-} f\left(\theta_i,\phi_i,\theta_r,\phi_r\right)\cos\theta_i d\Omega_i \qquad \text{Eq. 4}$$

where $d\Omega_i$ is the differential solid angle in the direction of incidence and Ω_- is the entire downward directional hemisphere (i.e., the set of all downward solid angles). In implementing of these calculations in the vegetation canopy reflectance model, an appeal was made to the property of reciprocity for these quantities, i.e.,

$$\rho^{(do)}(\theta,\phi) = \rho^{(sd)}(\theta,\phi) \qquad \text{Eq. 5}$$

so the same calculation is used for both, but for different directions.

Finally, the spherical albedo, $\rho_{soil}^{(dd)}$, gives the amount of downward diffuse flux that is reflected into the upward diffuse flux stream and is calculated given by

$$\rho^{(dd)} = \frac{1}{\pi}\int_{\Omega_-}\left(\int_{\Omega_+} f\left(\theta_i,\phi_i,\theta_r,\phi_r\right)\cos\theta_r\, d\Omega_r\right)\cos\theta_i d\Omega_i. \qquad \text{Eq. 6}$$

To couple the two models, the reflectance quantities defined by Equations 2 through 6 are replaced in ACRM with a linear combination of the soil reflectance quantities and corresponding reflectance quantities for a surface inundated with turbid water. Thus, the new reflectance quantities for the aquatic background are defined as,

$$\rho_{aquatic}(\theta_i,\phi_i,\theta_r,\phi_r) = (1-\beta)\rho_{soil}(\theta_i,\phi_i,\theta_r,\phi_r) + \beta\rho_{water}(\theta_i,\phi_i,\theta_r,\phi_r) \qquad \text{Eq. 7}$$

$$\rho_{aquatic}^{(do)}(\theta_i,\phi_i) = (1-\beta)\rho_{soil}^{(do)}(\theta_i,\phi_i) + \beta\rho_{water}^{(do)}(\theta_i,\phi_i) \qquad \text{Eq. 8}$$

$$\rho_{aquatic}^{(sd)}(\theta_r,\phi_r) = (1-\beta)\rho_{soil}^{(sd)}(\theta_r,\phi_r) + \beta\rho_{water}^{(sd)}(\theta_r,\phi_r) \qquad \text{Eq. 9}$$

$$\rho_{aquatic}^{(dd)} = (1-\beta)\rho_{soil}^{(dd)} + \beta\rho_{water}^{(dd)} \qquad \text{Eq. 10}$$

where, β is the fraction of the soil surface that is covered in water. In this study, β is binary and primarily used to turn the aquatic calculations on or off (i.e., $\beta = 1$ or $\beta = 0$, respectively); however, it is supposed that intermediate values might facilitate modeling the properties of partially covered (i.e., puddled) surfaces.

Finally, the aquatic background BRDF model is partitioned into specular and diffuse components to account for the reflectance at the air-water interface and below surface reflectance, respectively. It thus can be described mathematically as

$$\rho_{water}(\theta_i,\phi_i,\theta_r,\phi_r) = \rho^{(d)}_{water}(\theta_i,\phi_i,\theta_r,\phi_r) + \rho^{(s)}_{water}(\theta_i,\phi_i,\theta_r,\phi_r) \quad \text{Eq. 11}$$

Figure 2-1 illustrates the optical pathways of these two components. The specular component, $\rho^{(s)}_{water}$, is based on a model for a non-flat water surface. The diffuse component, $\rho^{(d)}_{water}$, simply assumes a diffuse reflector beneath the surface of the water at an arbitrarily small depth, which will be described later.

The Specular Component

The physical process underlying the specular reflectance of the air-water interface is best explained by Fresnel reflectance, calculations of which are given in Appendix A. A completely flat Fresnel reflector sends a reflected beam in a single direction. However, angular dispersal of some of the reflected light can be expected because water surface is rarely absolutely flat or still. Thus a specular reflectance model was chosen that incorporates the Fresnel reflectance of the water's surface, and includes reflected beam dispersion due to surface roughness. As specular reflectance is largely spectrally uniform over visible and NIR wavelengths, this component contributes primarily to the background influence in the BRDF anisotropy.

The specular component of the aquatic background BRDF is based on the model originally developed by Cox and Munk (Cox and Munk, 1954a; 1954b; 1956), which extends the notion of a Fresnel reflector to an open body of water with waves. The Cox-Munk specular reflectance model is largely based on the empirical response of the open ocean surface roughness to windspeed, but the model's treatment of the effects of a roughened surface is still applicable. However, the empirical linear relationship between the surface mean slope squared and the windspeed and direction is excluded from WCRM, because wind no longer plays a singular role in determining surface roughness for a marsh aquatic substrate.

The Cox-Munk specular model partitions the air-water interface into tiny facets, each being locally tangent to the surface. The physics of reflection and facet orientation are primary characteristics that determine how much radiant flux from the source is reflected in the direction of observation. First, the conventions and notations for describing the physics and facet geometry are described in Appendix A. Second, the amount of specular reflectance is driven by the physics of Fresnel Reflectance and is represented by the quantity, $r_f(\lambda,\omega)$ as defined in Appendix B. The amount of measured upwelling radiance is proportional to the projected area of the each facet in the direction of either the source or observation, which is given by $\cos\omega$. Similarly, the projected area of the region contain the facets change the radiance measured by $\cos\theta_r$. Furthermore, the area of the tilted facet is related to the horizontal plane by the factor $\sec\theta_n$, because θ_n is by definition the angle of greatest tilt of the facet. All these quantities must factor into the calculation of the total energy that is reflected by the aquatic surface.

In the Cox-Munk model, variation in the slope of these small facets of the water surface is treated as being independently and normally distributed in orthogonal, horizontal directions. Interestingly, this is the same as the more generalized Torrance-Sparrow model (Torrance and Sparrow, 1967) for surfaces with partial specular reflection. However, the Torrance-Sparrow model includes a factor to account for facet occlusion or shading. The absence of this factor is more appropriate for calm wetland surface conditions usually found under clear skies, hence the simpler Cox-Munk model is preferable. Also, whether the assumed normal distribution is ideal for cumulative effects of all the previously mentioned sources of surface disturbance requires further study. For this effort, however, it was decided that bounding the distribution variance would provide insight into the potential contribution of specular reflectance to the character of the marsh reflectance.

In the literature, the facet slope probability density function describing the facet slope distribution is usually defined over Cartesian space ($\mathbb{R}^2$) for the facet slopes z_x and z_y in the x and y directions, respectively, as

$$p_{\mathbb{R}^2}(z_x, z_y) = \frac{1}{\sqrt{2\pi\sigma}} e^{-\left(z_x^2 + z_y^2\right)/2\sigma^2} \qquad \text{Eq. 12}$$

To further simplify this probability density model, a version of the density function that is independent of wind direction is applied because the wind direction is not considered a significant contributing factor when shielded by vegetation. When open channels or ponds are combined with vegetation within pixels of remote sensing imagery, windspeed and direction may play a stronger role, however, generally the wind field is usually not available for the marsh at the scales of interest (Kay*, et al.*, 2009; Wang and Bailey, 2001).

The proportion of the horizontal surface area where facets are oriented to reflect from anywhere in a small solid angle in the direction of the source, $\vec{\xi}_i$ to the direction of observation, $\vec{\xi}_r$, is approximately given by $P_{\mathbb{R}^2}(z_x, z_y) \cdot dz_x dz_y$, which is the same as the probability that the slopes of a facet in the x and y directions, z_x and z_y, orient the facet such that light is reflected from the source to the direction of observation. With this, the Fresnel reflectance, and the projection cosines, the small amount of radiance produced by specular reflectance, $dL_{r,s}$, that can be measured in the direction of observation can be calculated as,

$$dL_{r,s} = L_i \frac{\cos\omega}{\cos\theta_n \cos\theta_r} r_f(\omega) \cdot p_{\mathbb{R}^2}(z_x, z_y) \cdot dz_x dz_y \qquad \text{Eq. 13}$$

where, L_i is the radiance of the source. For simplicity, the dependence on wavelength λ is omitted in this equation. For a more convenient application of the model in WCRM, the

variables are changed to spherical coordinates. Details are given in Appendix C regarding that conversion, which leads to the form,

$$dL_{r,s} = \frac{L_i}{4\cos^4\theta_n \cos\theta_r} \cdot r_f(\omega) \cdot p_\Omega\left(\theta_i,\phi_i,\theta_r,\phi_r\right) \cdot d\Omega_r \qquad \text{Eq. 14}$$

Allowing $d\Omega_r = d\Omega_i$ Equation 14 can be rearranged, and rewritten more compactly, to match the definition of a BRDF given in Equation 1. This gives the specular component of the water BRDF,

$$f_{water}^{(s)}\left(\theta_i,\phi_i,\theta_r,\phi_r\right) = \frac{r_f(\omega)\, p_\Omega}{4\mu_n^4 \mu_0 \mu} \qquad \text{Eq. 15}$$

using the common convention of defining $\mu_n = \cos\theta_n$, $\mu_o = \cos\theta_i$, and $\mu = \cos\theta_r$ and dropping the angular dependent variables for P_Ω to simplify the notation.

Surface Roughness of the Aquatic Background

The water surface in a marsh is typically calm, as the vegetation tends to shield the surface from the wind, therefore the degree of angular dispersion of the specular reflectance is smaller than open water conditions (Vanderbilt*, et al.*, 2002). However, it was observed in the field that the water surface rarely stays completely flat and some dispersion of specularly reflected light can be expected from the presence of small distortions, both dynamic and static, in the air-water interface.

Dynamic distortions include primary capillary waves from disturbances. Some coastal breezes are sufficiently strong to cause very small capillary waves in the flat surface, even for the water surface between plants, either directly or to a much smaller extent indirectly by wind driven movement of the plants themselves. Waves can also start from outside the canopy, but are quickly dissipated by the vegetation. It was also

observed that the water surface could occasionally be disturbed slightly by the movement of fauna, such as insects and insect larvae, or by bubbles rising from the bottom.

Static distortions are mainly facilitated by water tension. Water tension can cause curvature in the air-water interface around plants and debris that penetrate or float on the air-water interface (see Figure 2-3). Similarly, the presence of scum or floating debris could also change the specular and diffuse reflective properties of the surface. Finally, additional dispersion of the direct beam, independent of the surface, may include light diffusion by the atmosphere and the canopy (especially at near-infrared wavelengths). This type of scatter could appear like the effects caused by static surface roughness, and its effect may be included into the same calculation.

Figure 2-3. Photograph of specularly reflected light in the marsh. This close-up photograph of a *Spartina alterniflora* canopy in the Blackwater Marsh in Maryland, USA demonstrates the distortion to the air-water interface created by the presence of vegetation and water surface tension.

In general, all these surface distortions could possibly reflect light away from the direction of specular reflectance for a completely flat surface. Furthermore, from a remote sensing perspective, the pixel field-of-view of a spaceborne or airborne imager's pixels is likely to mix light reflecting from channels and ponds along with the vegetation canopy. These small bodies of water have a more significant fetch length and were observed to be often roughened by the wind. Therefore, when pointed near the specular direction, it is likely that an imaging remote sensing instrument with a pixel size greater than a meter or more will consistently detect specular reflectance from the sun, even when the air-water interface is essentially still within the canopy.

The Diffuse Component

The diffuse reflectance component depicts reflectance just below the water's surface and is modeled simply as a submerged isotropic reflector at zero depth. This component of the background reflectance is further approximated as a combination of the absorption and backscatter properties of turbid water along with the reflective properties of submerged vegetation. As this component make assumptions of isotropy below the water's surface, it is not expected to contribute to the canopy anisotropy. Conversely, as the specular component is spectrally uniform across the visible and NIR wavelengths, the diffuse component contributes the most to the spectral characteristics of the aquatic background. In this model, light passes through the air-water interface, reflects uniformly in all directions from under the surface, and returns through the air-water interface. Thus, light emerging in the air from the water was subjected to at least two Fresnel transmission events (i.e., in and out of the water) and one isotropic reflectance event.

Substituting in quantities for air-water interface transmissivity and subsurface reflectivity (Mobley, 1994) in a calculation derived by Bohren and Clothiaux (2006) for a submerged diffuse reflector, the upwelling radiance from just below the surface can be approximated by

$$L_{r,d} = n_r^2 t_f(\theta_i) t_f(\theta_r) \frac{r_d}{\pi} L_i \cos\theta_i \Omega_i \qquad \text{Eq. 16}$$

where, once again dropping the wavelength dependence for simplicity, the Fresnel transmittance is given as

$$t_f(\theta) = 1 - r_f(\theta). \qquad \text{Eq. 17}$$

and r_d is the irradiance reflectance of the submerged diffuser. The transmittance $t_f(\theta)$ pertains to a flat air-water interface and does not consider the effect of surface roughness,

as was done for the specular component. However, Monte Carlo modeling of Fresnel transmittance across a roughened surface showed little difference (<3%) between a smooth surface and the surface conditions more likely found on even a large body of water with strong winds. Thus simplifying the model to use a flat surface transmittance is considered a reasonable approximation for wetland aquatic surface conditions. The first t_f in Equation 16 gives the transmittance of light across the air-water interface into the water from the air at the angle of incidence θ_i, as measure from the zenith direction. The second use of t_f gives the transmittance from water to air at zenith angle θ_r in the direction of observation. Using reciprocity, this is computed as the transmittance from air to water at incident zenith angle θ_r.

Replacing the incident solid angle Ω_i in Equation 16 with a small incremental quantity $d\Omega_i$ can be said to produce a small incremental quantity dL_i. Thus, the equation can be rewritten to form a BRDF for the diffuse component of the aquatic background,

$$\frac{dL_{r,d}}{L_i \cos\theta_i d\Omega_i} = n_r^2 t_f(\theta_i) t_f(\theta_r) \frac{r_d}{\pi} \qquad \text{Eq. 18}$$

Lee et al. (1998) described a more rigorous formulation that includes more detail of the underwater light field with the equation

$$R_{rs} = n_r^2 t_f(\theta_i) t_f(\theta_r) \frac{r_d / \pi}{1 - Q\gamma \, r_d / \pi} \qquad \text{Eq. 19}$$

where, the remote sensing reflectance, R_{rs}, is defined as the ratio of above-water radiance leaving the water from just below the surface to the above-water downwelling irradiance. Q is the ratio of the downwelling irradiance below the surface to the upwelling radiance at nadir. Q is a measure of the isotropic characteristics and, by definition, becomes π for

isotropic reflectance. γ is a factor that accounts for internal reflection below the air-water interface. Lee et al. (1998) gives a value for γ of around 0.48 (Gordon*, et al.*, 1988; Lyzenga, 1978). With these assumptions, we can use Equation 19 to incorporate consideration for the effects of internal reflectance, which can be significant.

Unlike the definition given for BRDF, R_{rs} depends on the irradiance from all directions in the hemisphere. For a diffuse reflector, however, the reflected radiation will be nearly the same regardless of the nature of the incident light field. So, for the diffuse component of the marsh aquatic background, R_{rs} is taken to be a close approximation to the BRDF. Therefore, we can write the diffuse component of the marsh aquatic background BRDF as,

$$f_{water}^{(d)}\left(\theta_i,\phi_i,\theta_r,\phi_r\right)=\frac{n_r^2 t_f\left(\theta_i\right)t_f\left(\theta_r\right)r_d}{\pi\left(1-\gamma r_d\right)}. \qquad \text{Eq. 20}$$

It should be noted that the new internal reflectance factor of $1/(1 - \gamma r_d)$ is more significant for high subsurface reflectance, increasing the amount of radiance seen by the observer by as much as a factor of two, as illustrated in Figure 2-4. However, for dark subsurface reflectors, which are often seen in marsh conditions, the increase is relatively small. For instance, a 10% irradiance reflectance would increase the observed radiance by around 5%; a 20% irradiance reflectance would get an increase of around 10%. But, the reflectance measured for a wet marsh soil sample alone did not exceed 12% over the spectral range from 400 to 1000nm. Thus, the predicted positive bias for internal reflectance would typically not significant. Conversely, the presence of light sand or a suspension of bright soil particles could cause larger effects. Thus, the correction factor $1/(1 - \gamma r_d)$ is included so the that model can provide for a broader range of applications.

The final step is to determine the reflectance attributed to scatter beneath the air-water interface, r_d. The shallow water model developed by Lee et al. (1998; 1999) is well

described by Volpe et al. (2011) for coastal applications. The underwater remote sensing reflectance, which is take as equivalent to r_d in this case, is given by

$$r_d = r_{rs}^{dp}\left[1 - e^{-\left(K_d + K_u^C\right)H}\right] + \frac{\rho_b}{\pi} e^{-\left(K_d + K_u^B\right)H} \qquad \text{Eq. 21}$$

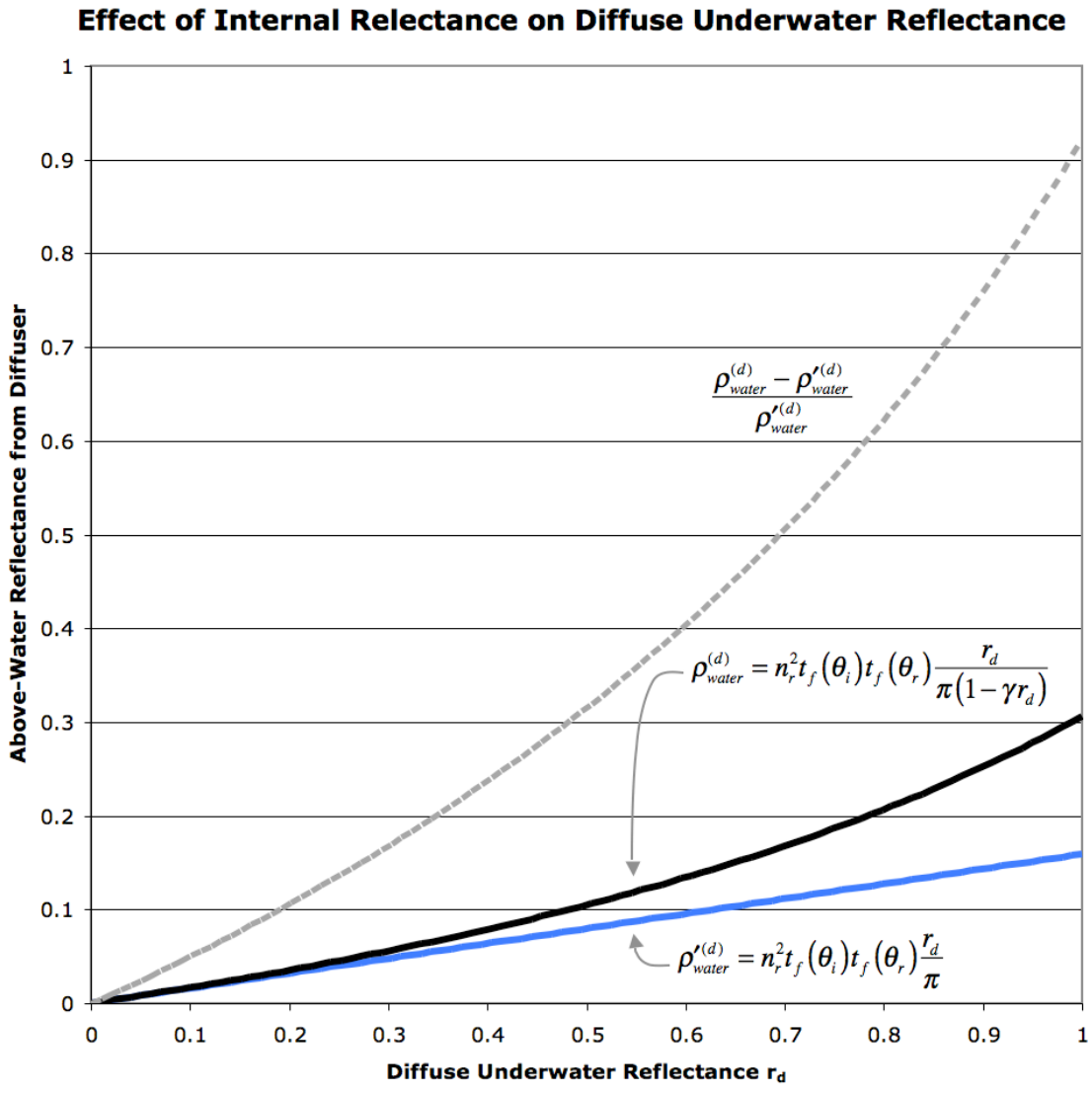

Figure 2-4. Predicted above-water reflectances for a submerged diffuser reflector. Reflectance r_d is varied from 0 to 1. The black curve gives the response with internal reflectance included and the blue without internal reflectance. The gray dashed curve shows the relative difference between the two. Note that the correction becomes increasingly less significant with decreasing r_d.

The details of this model are given in Appendix D, including the definition of the quantities that appear on the lefthand side of the equation. The shallow water reflectance model is used to understand the reflectance spectrum of the aquatic background and is discussed further in Chapter 6.

Computing the Four Reflectance Quantities for Water

The BRDF for the specular and diffuse components are combined to form a model of the total effect of the aquatic background. The combined BRDF is then used to form the reflectance quantities used by the vegetation canopy model through integration. Substituting Equations 15 and 20 into Equation 11, the water component of the background BRDF becomes

$$f_{water}\left(\theta_i,\phi_i,\theta_r,\phi_r\right)=\frac{n_r^2 t_f\left(\theta_i\right)t_f\left(\theta_r\right)r_d}{\pi\left(1-\gamma r_d\right)}\ +\ \frac{r_f\left(\omega\right)p_\Omega}{4\mu_n^4\mu_0\mu} \qquad \text{Eq. 22}$$

where ω, P_Ω, μ_n, μ_0, and μ are dependent on $(\theta_i,\phi_i) \in \Omega_-$ and $(\theta_r, \phi_r) \in \Omega_+$, as previously defined. Examples of the resulting distribution are illustrated in Figures 2-5 and 2-6, both with r_d set to 0.1. Figure 2-5 shows a cross section of the BRDF along the principal solar plane for a zenith angle of 45 degrees and azimuth of 180 degrees. The separate contributions of the specular and diffuse components can be clearly seen in curves corresponding to low values for σ. Fresnel transmittance causes the diffuse component to drop off significantly near the horizon. This also produces the darken disk edges and the overall darker blue disks in the bottom row in Figure 2-6. The increase of the specular component with increasing surface roughness, and the drift of its peak toward higher angles, is driven by the cosine of the viewing and illumination zenith angles in the denominator of Equation 12. These factors account for the amount of light being received by a detector with a fixed solid angle that is subtended by an area that is

increasing with the secant of the viewing angle, and hence likewise viewing an increasing number of highlights.

This does not take into account the attenuation of highlight over that area, which tends towards being a parabolic section (i.e., with infinite area) as the detector approaches the horizon. In addition, the model as configured ignores the effects of shadows, multiple scattering events, or the visual overlap of waves (Cox and Munk, 1954a; 1954b; 1956). However, it is assumed that the omission of such effects, which pertain to high zenith angles (e.g., >60°) or extremely rough surface conditions (e.g., σ >0.15), does not significantly degrade the model's ability to provides a practical prediction for surface

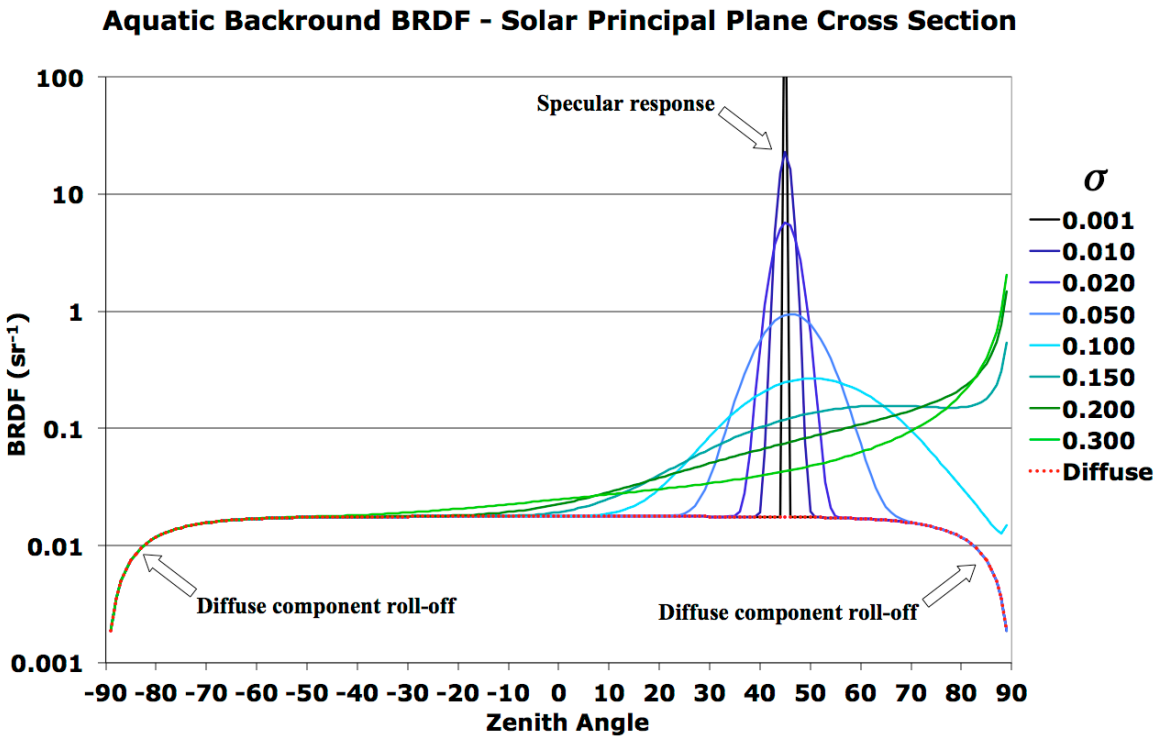

Figure 2-5. The BRDF along the principal plane for several values of σ. In this plot, r_d is set to 0.1 and the direction of illumination is 45° from zenith and 180° azimuth, which for comparison corresponds to the middle row of Figure 2-6. The specular and diffuse components are clearly identifiable for low σ, where the specular component form a localized peak at 45° (and 0° azimuth) and the diffuse component from a base (shown in red) that is treated as independent of surface roughness. The latter can also be seen to decrease significantly for large zenith angles as the transmittance across the air-water interface decreases.

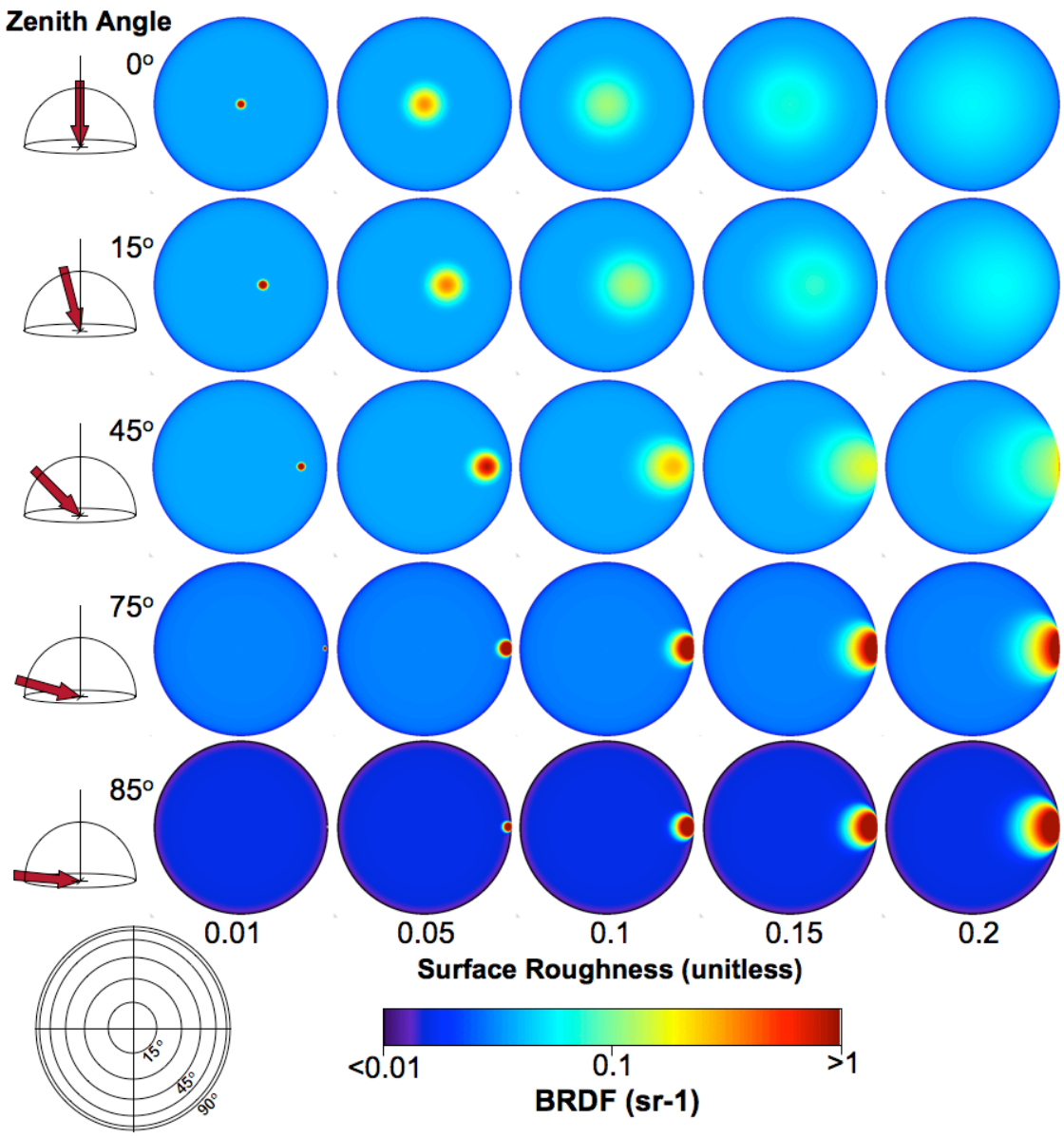

Figure 2-6. Selected BRDF reflectance response as calculated with Equation 22. Rows are associated with zenith angles of an incident beam of light and columns give different values of σ, which represent surface roughness. The disks show the distribution of the reflected light over the hemisphere, following the projection indicated by the diagram in the lower lefthand corner. Light enters from the left and the principal plane is horizontal and perpendicular to the page. The graded color bar gives the numerical meaning of the color in the disks. The reflectance r_d is set to 0.1 in this example. The colors at the very ends of the bar include values that exceed the numerical range indicated. The decrease of the reflectance distribution along the horizon (disk's edge) is caused by the diffuse component roll-off caused by the decreased transmittance across the air-water interface at high zenith angles. Note that by reciprocity, replacing the incident light direction with the observation direction will produce the same distributions.

reflectance over most of the hemisphere of interest to remote sensing of coastal marshes. Additional reading on this topic can be found in a paper by Zeisse (1995).

Figure 2-6 demonstrates how surface roughness disperses the reflected light over the entire upper hemisphere. Going across columns (i.e., varying σ in Equation 16 to change surface roughness) the light is scattered over a large range of directions with increasing surface roughness. This effectively decreases the amount of light that is going in the direction of specular reflectance, which is largely depicted by the first column on the left in Figure 2-6, and increases the amount of light going elsewhere in the upper hemisphere, especially in directions that are close to the specular direction. This change in distribution effectively increases the brightness of the water with surface roughness.

Following the definition given by Equation 2, the BRF used in the vegetation canopy model is calculated as,

$$\rho_{water}\left(\theta_i,\phi_i,\theta_r,\phi_r\right)=\pi f_{water}\left(\theta_i,\phi_i,\theta_r,\phi_r\right) \qquad \text{Eq. 23}$$

This quantity controls the amount of reflected light predicted to reach the observer from single scatter events from the aquatic surface (see 5 in Figure 2-2). To determine the water contributions to the reflectance quantities defined in Equations 3, 4, and 6, Equation 22 is integrated over the upward hemisphere Ω_+ to get $\rho_{water}^{(do)}$ or hemisphere downward Ω_- to get $\rho_{water}^{(sd)}$, or both and divided by π to get $\rho_{water}^{(dd)}$. As previously mentioned, the principle of reciprocity results in $f_{water}\left(\theta_i,\phi_i,\theta_r,\phi_r\right)=f_{water}\left(\theta_r,\phi_r,\theta_i,\phi_i\right)$. Thus the hemispheric-directional and directional-hemispheric reflectances are both calculated as

$$\begin{aligned}\rho_{water}^{(do)}(\theta,\phi) &= \rho_{water}^{(sd)}(\theta,\phi)\\ &= \frac{n_r^2 t_f(\theta) T_f r_d}{\left(1-\gamma r_d\right)} + \frac{1}{4\mu}\int_{\Omega}\frac{r_f(\omega)\,p_{\Omega}}{\mu_n^4}\,d\Omega\end{aligned} \qquad \text{Eq. 24}$$

where $d\Omega = \sin\theta \; d\theta \; d\phi$, $\mu = \cos\theta$, and the subscripts for θ, ϕ, and Ω are dropped to generalize the form of the function. Assuming azimuthal isotropy, the constant T is simply the integral of the Fresnel transmittance over a hemisphere, which can be written

$$T_f = 1 - 2\int_0^{\pi/2} r_f(\theta)\cos\theta\sin\theta\, d\theta. \qquad \text{Eq. 25}$$

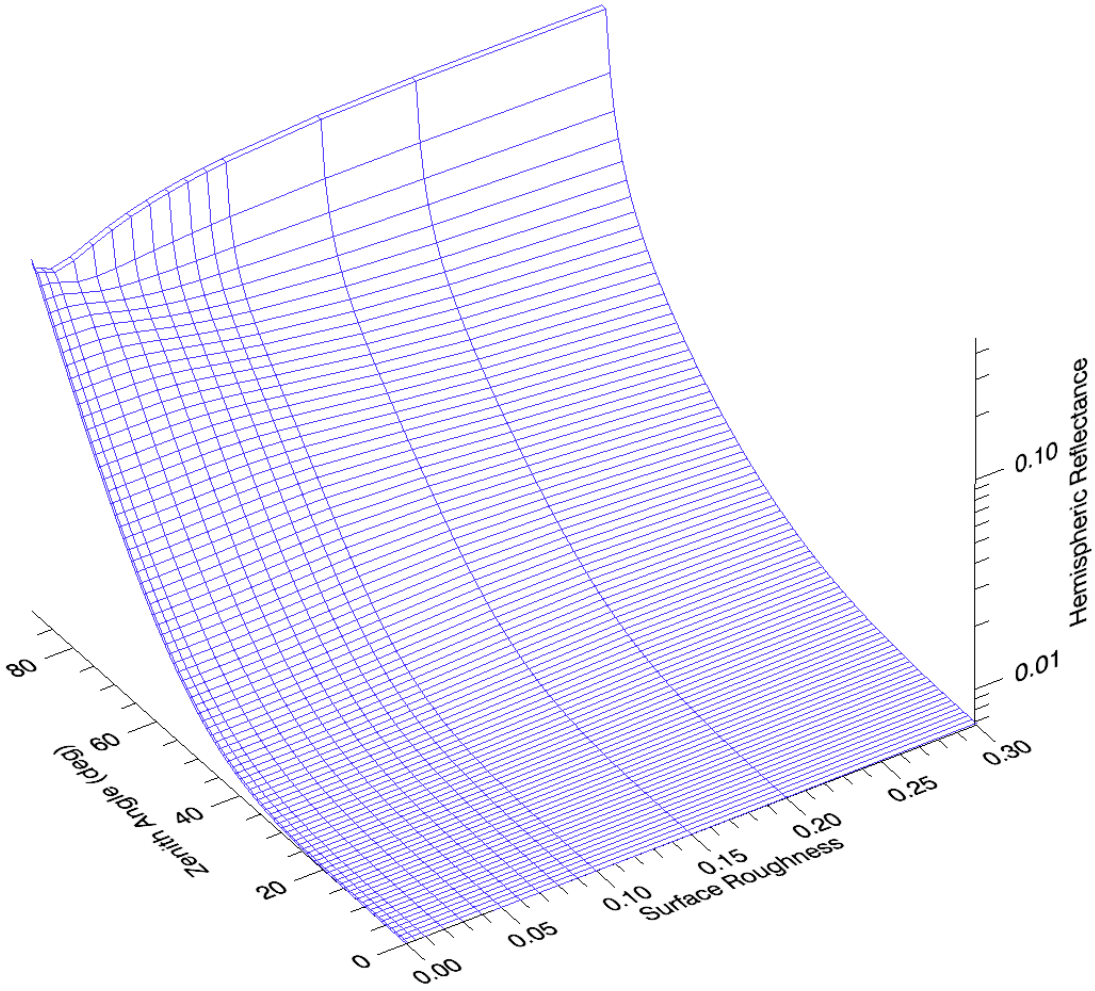

Figure 2-7. Look-up table for the specular component of the directional-hemispheric or hemispheric-directional reflectances. As calculated by the second term of Equation 24, this table is a function of zenith angle and surface roughness, σ. The values in the plot above show this reflectance quantity divided by π. The intersection of the blue curves indicate points that are used in the look-up table for the aquatic background model.

Applying numerical integration to compute the righthand side of this equation gives $T_f = 0.93$. The second term of Equation 24 is also computed by numerical integration for various values of the mean slope square of the air-water interface, σ, representing surface roughness, and zenith angle, θ. For application in the vegetation model, these values are interpolated in a look-up table as shown in Figure 2-7. As illustrated by the plot, the specular component of Equation 24 is primarily driven by Fresnel reflectance, as described in Appendix B, and exactly so for $\sigma = 0$. Thus, in log space, the component rises steadily from zenith angles of about 45°, but varies slightly with changes in surface roughness. In particular, the specular component decreases with increasing surface roughness from around 45° and above, only sharply increasing at very high angles, but increases slightly for zenith angles much lower than 45°. With increased variation in the surface, there are more opportunities for lower reflectance facet orientations when reflectance would otherwise be high or vice versa when reflectance would otherwise be low (i.e., near zenith). In the vegetation canopy model, the total value for $\rho_{water}^{(do)}$ controls the amount of direct illumination that contributes to the upward diffuse flux (component 4 of Figure 2-2) and $\rho_{water}^{(sd)}$ controls the amount of light going from the downward diffuse flux directly toward the observer from the background (component 8 in Figure 2-2).

Following the definition given by Equation 6 the albedo of the aquatic background is calculated as,

$$\rho_{water}^{(dd)} = \frac{n_r^2 T_f^2 r_d}{\left(1 - \gamma r_d\right)} + \frac{1}{4\pi} \int_{\Omega_-} \int_{\Omega_+} \frac{r_f(\omega)\, p_\Omega}{\mu_n^4} d\Omega_r \, d\Omega_i \qquad \text{Eq. 26}$$

The behavior of the diffuse and specular contributions are illustrated in the plots in Figure 2-8. As shown, the numerically integrated specular component (second term) in Equation 26 is approximately independent of surface roughness. Therefore a value of 0.026 is used in the model algorithm in place of this term and hence plays a very small role in the background albedo, unless the diffuse reflectance is less than ~2%. The diffuse

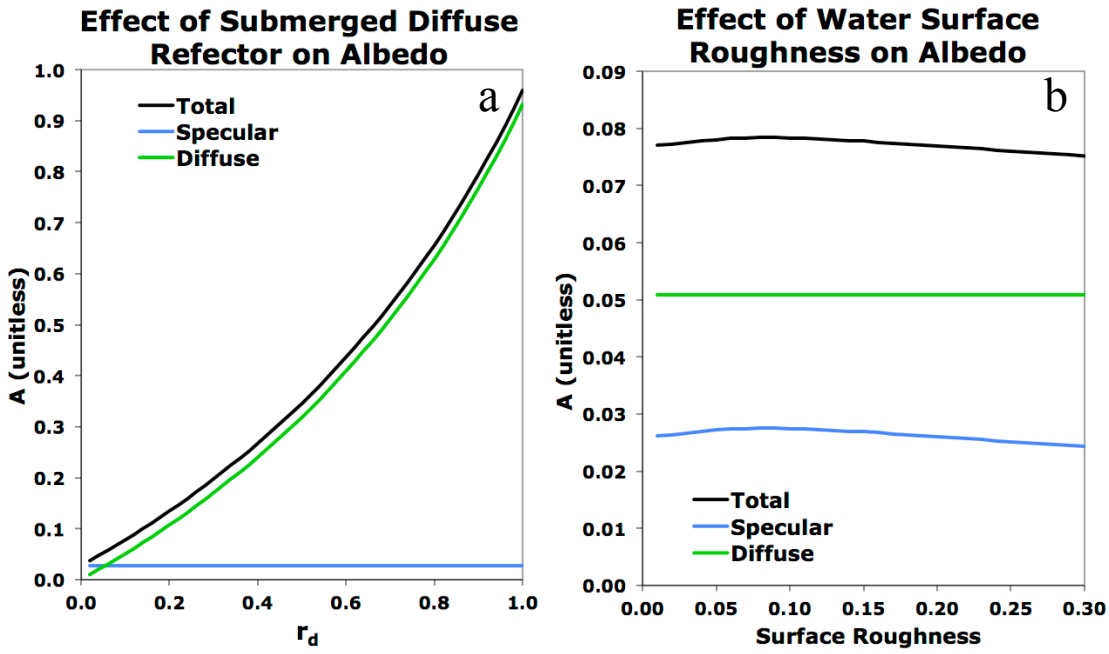

Figure 2-8. The aquatic background albedo. The aquatic background albedo (A) is primarily a function of the reflectance below the air-water interface, as illustrated in a. Surface roughness has little effect on albedo as shown in b (r_d is set to 0.1 in this example).

component, conversely, is strongly driven by the subsurface diffuse reflectance r_d. The internal reflectance is set to 0.48 in calculating the diffuse component. In the vegetation model, the total albedo controls the flow of light from the downward diffuse flux to the upward diffuse flux (component 9 in Figure 2-2).

Physical Plausibility of the Model Predictions

Little is known about the surface reflectance of the aquatic substrate, and no data could be found in the literature regarding some aspects of the surface conditions, such as surface roughness. However, it is worth considering whether results of modeling of the aquatic background at least make physical sense. As expected, results showed that the surface roughness plays strong role in varying the BRF around the specular direction. A small amount of surface roughness can disperse the distribution of reflectance light away from the specular direction. For zenith angles greater than zero, increasing surface

roughness pushes the reflectance peak towards the horizon, in addition to widening the dispersion pattern. This result follows the expectation that for all the opportunities afforded by non-horizontal air-water facets, the ones reflecting at higher angles will have the greater reflectance. Furthermore, the facets tilting away from the incident light have a small range of zenith angles to which they can redirect the light than facets tilting towards the light. Therefore, the beam distribution is skewed to a greater zenith angle than that of the specular direction.

It was also noted that surface roughness had a milder influence on hemispheric-directional and directional-hemispheric reflectances. The effect of surface roughness on albedo, which is mostly dependent on the subsurface reflectance, is very small. For low zenith angles, the Fresnel reflectance is at a minimum for a flat surface, so some variation in the air-water interface increases these reflectance quantities. For larger zenith angles, where Fresnel reflectance is higher, the opposite happens, and thus the hemispheric reflectance decreases with increasing surface roughness. The model predicts a sudden increase with surface roughness of hemispheric reflectance near the horizon, but this possibly stems from a breakdown in the model's representation where the calculation becomes indeterminate (Zeisse, 1995). However, this is not a practical limitation for employing the model for remote sensing of the marsh landscape.

After the aquatic background model was integrated into the vegetation canopy reflectance model, results from the new WCRM model were also considered. Figure 2-9 illustrates the response of the enhanced model, WCRM, along the solar principal plane (SPP) for varying LAI and surface roughness, σ. This sensitivity analysis indicated that the model response is greatest for these two parameters around the specular direction, as expected. Conversely, the influence of σ diminished rapidly as the viewing angle moves away from the specular reflection, which was also expected. Decreasing σ rapidly increased and narrowed the spike associated with specular reflectance. Specular reflectance was also strongly attenuated by increasing LAI.

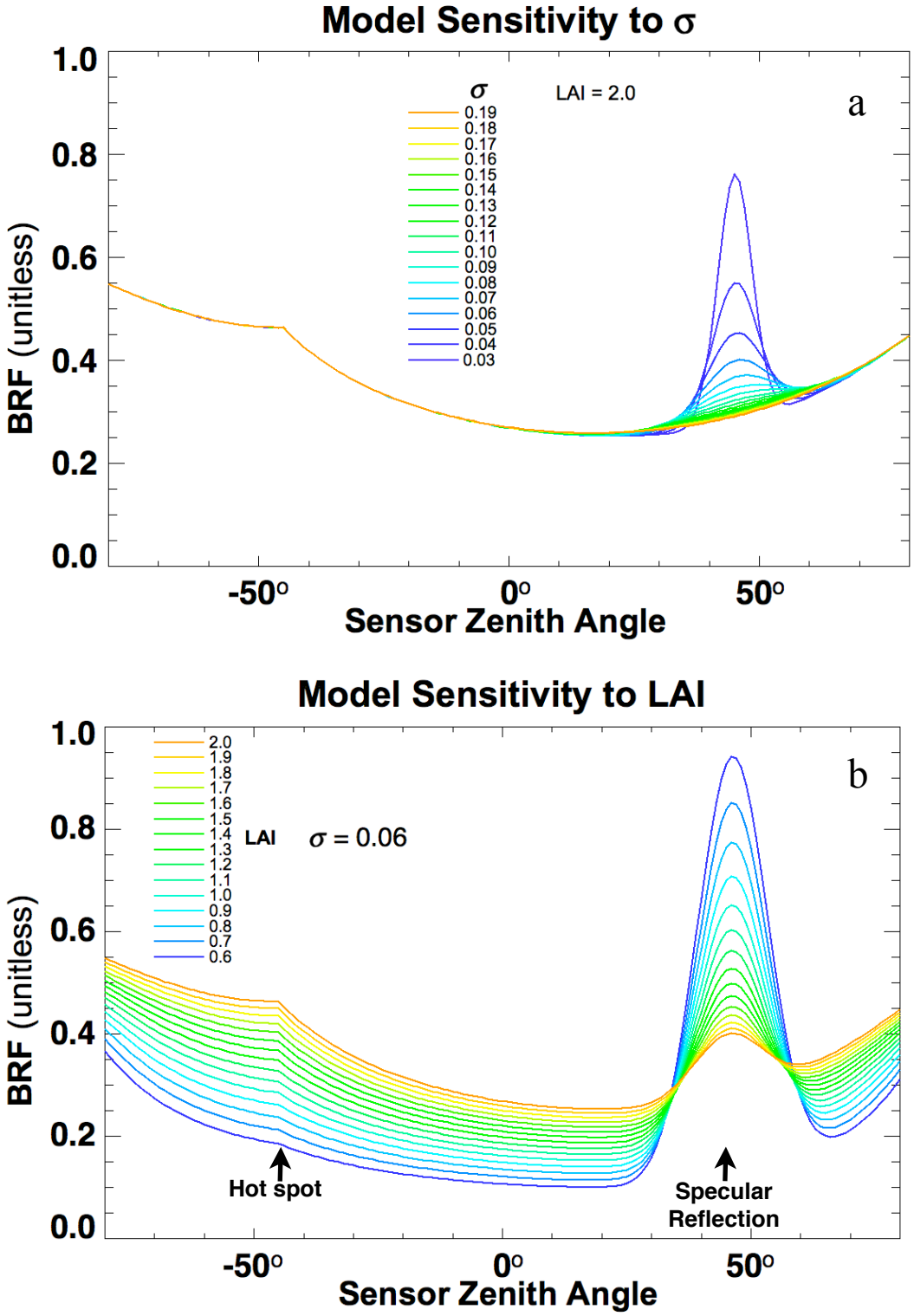

Figure 2-9. The response along the principal solar plane of the full marsh vegetation model. Shown is the variation to a) the surface roughness σ and to b) to LAI. In this case, the 45° solar zenith angle and wavelength is 920 nm.

Therefore, it can be concluded that dense vegetation is less susceptible to aquatic background specular reflection, as it would be for any background. However, this pertained to a uniform distribution of marsh cover, which is generally not the case on a scale of meters or smaller. Hollows and spaces in the canopy are not uncommon and could cause specular reflectance to direct additional light toward the observer, even when the surrounding canopy is fairly dense. WCRM will require further work to address those kinds of vegetation spatial distributions. It was further observed that the specular reflectance peak was substantially higher for NIR wavelengths than for visible wavelengths. This not remarkable as more light would be transmitted to the water surface in the NIR, albeit though the diffuse flow. However, further model runs at different wavelengths showed that the specular peak was twice as high for the NIR than for the blue even when LAI was set for 0.01. As the specular component of the aquatic background model as no spectral dependence, this results much stem from a limitation of the vegetation canopy reflectance model (i.e., ACRM) in modulating the flow from the background for very sparse vegetation.

Summary

A simple, first-principle model of the aquatic background BRDF was formulated based on a specular component for the air-water interface and a diffuse component to calculate reflectance from beneath the surface. The specular reflectance based a roughened specular reflector as described by the Cox-Munk model (Cox and Munk, 1954a; 1954b; 1956; Kay*, et al.*, 2009). This component is principally driven by the Fresnel reflectance of the air-water interface, however light is dispersed around the specular direction by surface roughness, σ. The diffuse reflectance is based on the Lee shallow water reflectance model (Lee*, et al.*, 1998; 1999). This component is based on an isotropic reflector that is submerged in turbid water. This component is also subject to Fresnel transmittance of the air-water interface and an approximation of the effect of

internal reflection under the air-water interface. These two component were then summed to calculate to the total aquatic background BRDF for the new enhanced canopy reflectance model.

The aquatic background BRDF was then used to calculated the four key reflectance quantities used for the background in the ACRM vegetation canopy reflectance model (Kuusk, 1995a; 1996). The first of these quantities was the BRF, which is used to determine the amount of observed reflectance due to direct illumination of the aquatic background. The BRDF was also used to compute the direct-hemispheric reflectance and hemispheric-direct reflectance. The direct-hemispheric reflectance is used in the vegetation canopy reflectance model to determine the amount of light reflected from the direct flux into the diffuse upward flux. Similarly, the hemispheric-direct reflectance determines the amount of diffuse downward flux that is reflected directly towards the observer. Both the direct-hemispheric and hemispheric-direct reflectances were determined through analytic integration of the diffuse BRDF component and numerical integration of the specular BRDF component. To implement the specular BRDF component of the hemispheric reflectances, a look-up of table was created from the numerical integration. Finally, the BRDF was integrated over all upward and downward directions to calculate the aquatic background albedo, which in the vegetation canopy reflectance model governs the amount of the diffuse downward flux is redirected into the diffuse upward flux. The resulting calculations for all four reflectance quantities were implemented in FORTRAN code and integrated with the ACRM program to create WCRM. Details of that implementation are given in Appendix E.

Chapter 3 Effects of the Background on LAI Retrieval

Introduction

One application of a canopy reflectance model is to retrieve LAI given measured canopy reflectance data at various angles, which is done by inverting the model using an optimization technique. This chapter examines the feasibility of such retrievals. To that end, both the ACRM and WCRM models were run for a range of LAI values to relate LAI to canopy reflectance at various viewing directions and wavelengths. This establishes conditions where retrieval of LAI from reflectances can potentially be done. It is shown that the presence of a low-reflectance substrate reduces the potential of LAI retrieval at visible wavelengths, but increases the potential at NIR wavelengths. It is also reported that the inversion technique that is built into the canopy reflectance model can dwell indefinitely on the initial guess when the potential to retrieve LAI is low. An example scenario is provided.

Inversion Technique

To retrieve LAI from reflectance measurements, the canopy reflectance model must be inverted. That is to say, values are found for the model input parameters that best explain the measured reflectance values. The technique employed in this study accomplishes this in a fashion analogous to a nonlinear regression fit of the model to the data. In that sense, the model input values are systematically varied until the difference between the model output and measured values are minimized. This is also known as an optimization problem, and is commonly used in remote sensing applications because the desired surface parameters are not directly measurable by the sensor, but instead determined *remotely* through the measurement of light.

WCRM and ACRM were inverted using the Powell method, as described in Press et al. (1992). As with most optimization techniques, the difference between predicted and measured light must be systematically minimized using a quantity that gives the size of that difference. Furthermore, it needs to be weighted to emphasize input parameters that are more important or more accurate. That quantity is determined by following equation, also know as a cost function, which was defined by Kuusk (2009) for ACRM:

$$F(\vec{\mathbf{x}}) = \sum_{j=1}^{m}\left(\frac{\rho_j^* - \rho_j}{\varepsilon_j}\right)^2 + \sum_{i=1}^{n}\left[\left(x_i - x_{i,b}\right)^4 w_i^2\left(\frac{x_i - x_{e,i}}{dx_i}\right)^2\right] \qquad \text{Eq. 27}$$

where, $\vec{\mathbf{x}}$ is the vector of model input parameters, m is the number of measured reflectance values ρ_j^*, ρ_j is the model reflectance value, ε_j is the error of the measured reflectance value ρ_j^*, x_i is the i^{th} model input parameter and $x_{i,b}$ is its value on the boundary of the given region. w_i is a weight such that $w_i = 0$ in the given region $x_i = \{x_{i,min}, x_{i,max}\}$ and w_i is defined as a constant elsewhere. $x_{e,i}$ is the expert estimate of x_i and dx_i is a tolerance for x_i that controls the sensitivity of the cost function to the expert estimate. Default values for the weight, tolerance, expert values, boundary values, and error were used for all input parameters, except for certain exception as will be discussed. This equation was built into the software by its original author to facilitate the retrieval of input parameters given measured reflectances. Analysis of WCRM and ACRM showed that both models are more sensitive to LAI than any other input parameter. Thus, the inversion is greatly simplified by using representative values for other input parameters and let only LAI vary in the inversion.

Background Spectrum

Comparisons between ACRM and WCRM demonstrates that the background spectrum strongly affects the relationship between LAI and the canopy reflectance. The aquatic background model in WCRM produces a different reflectance spectrum than the

embedded soil spectrum model in ACRM, which is generated by a linear combination of four Price functions (Price, 1990). ACRM uses four Price function coefficients to describe a variety of background terrestrial soil spectra, and does not take an entire spectrum as an input parameter. By default, the inversion mode of the ACRM model allows the coefficients for the first two Price functions to fit the measured reflectance to account for a variety of soil types, without *a priori* knowledge of the target's soil spectrum. ACRM also can be run using the default expert values for the Price coefficients or they can be fixed to match a known soil spectrum. Figure 3-1 shows examples for five background spectra for ACRM and WCRM. The ACRM includes: default expert soil (gray), measured and modeled dry marsh soil (orange and red),

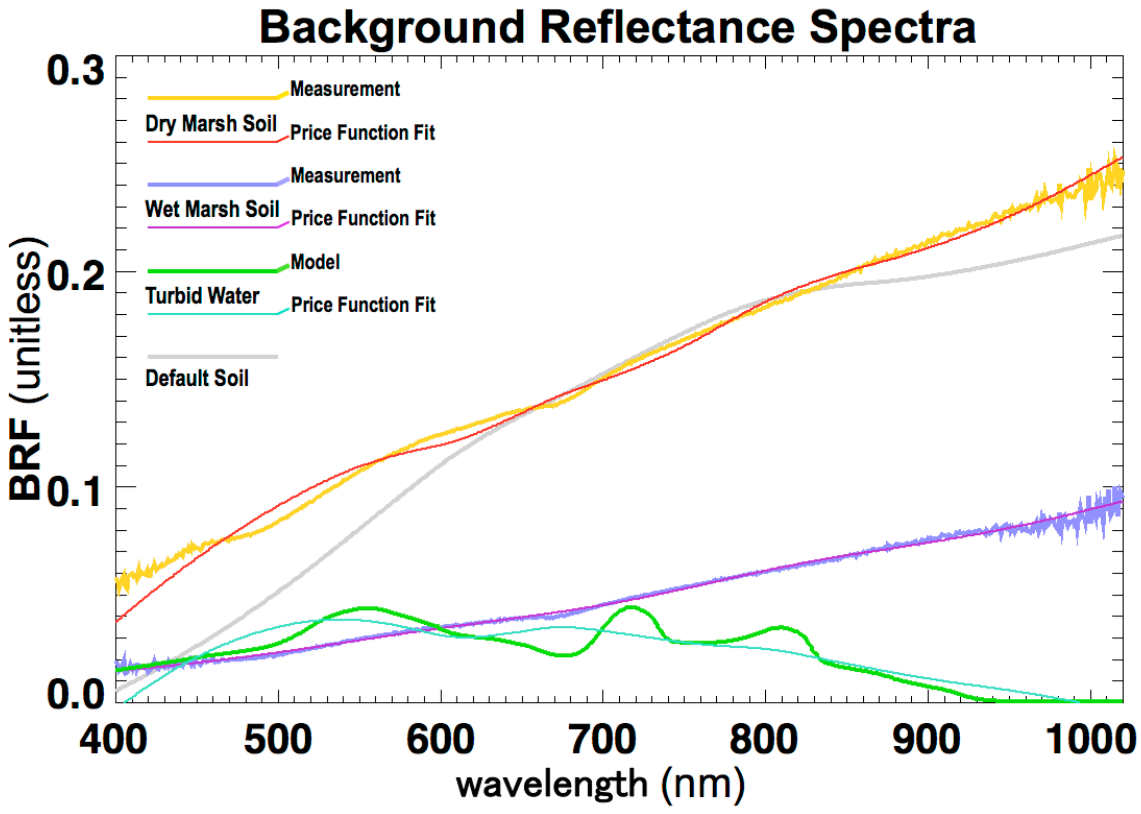

Figure 3-1. The five spectra used in the LAI retrieval test and their corresponding Price function fits. The Default Soil spectrum is the expert guess for the soil spectrum used by the default configuration of ACRM. Dry Marsh Soil and Wet Marsh Soil spectra were taken from marsh soil samples, the latter being nearly saturated. The Turbid Water spectrum is the same as the modeled spectrum in Figure D-3.

measure and modeled wet marsh soil (blue and purple), and for turbid water (green and turquoise).

The measured dry and wet marsh soil spectra were from a soil sample taken from the Blackwater Marsh, Maryland in 2008. 17.3 g of the soil was left to air dry at room temperature for 24 hours. Most of the organic debris were removed from the soil sample by hand. 15 g of tap water was mixed into the soil to produce a nearly saturated soil. BRF spectra were taken for both the dry and wet cases with an Ocean Optics USB2000+ spectrometer and a Spectralon reference panel. Illumination and spectrometer probe were set at 45° from zenith and rotated azimuthally by 90° to reduce the effects of glint.

The Price function coefficients for the each spectrum were derived by multiplying the spectrum by a Moore-Penrose inverse of the Price four-vector basis. The turbid water spectrum pertains to a case of the WCRM aquatic background that includes submerged vegetation as described in Appendix D. The fit of Price functions to the WCRM turbid water spectrum was poor when compared to the soil spectra fits. The ACRM background also differs from the full WCRM model by the exclusive use of the Walthall soil BRDF model (1985) and the omission of the aquatic calculations pertaining to the passage of light across the air-water interface found in WCRM.

The Relationship between LAI and Canopy Reflectance

To understand the feasibility of LAI retrieval, both the WCRM and the ACRM models were run for various LAI values and these values were plotted against the SPP canopy reflectance for different wavelengths and sensor zenith angles. The default expert soil was used for ACRM (cf. gray curve in figure 3-1). This produces a spectrum that is only slightly higher in blue reflectance when compared to the WCRM aquatic background spectrum, but is increasingly much higher with increasing wavelength. The solar zenith was set to a nominal 45°. The WCRM surface roughness, σ, was set to a nominal value of 0.06, which was derived by a fit to field data. The aquatic ground

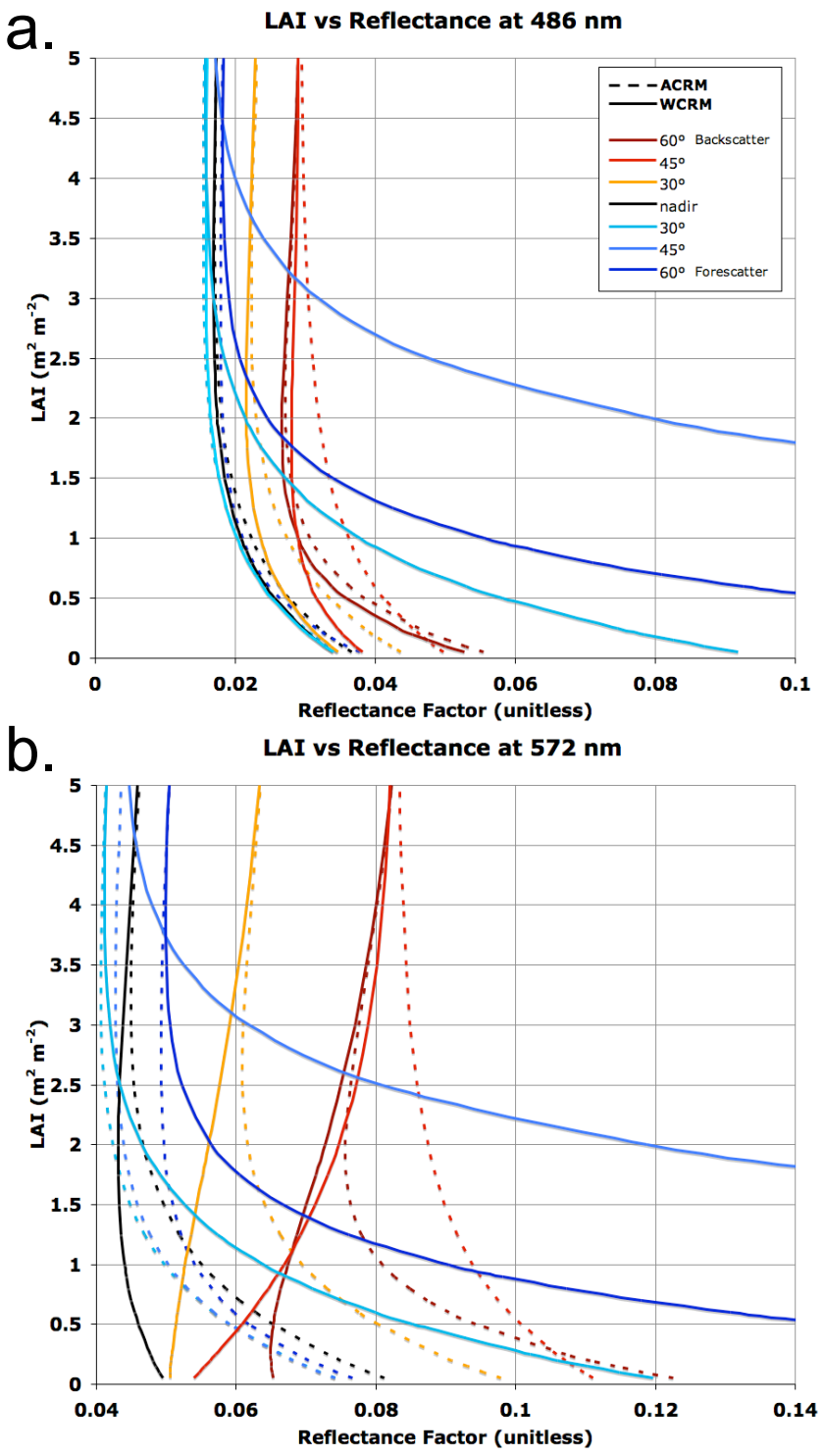

Figure 3-2. The ACRM and WCRM modeled relationship between LAI and canopy reflectance. The relationship is shown for several sensor zenith angles along the solar principal plane at a) 486 nm and b) 572 nm. Solar zenith angle was set to 45° for both models. The default soil was used for ACRM. WCRM was run with $\beta = 1$ and $\sigma = 0.06$.

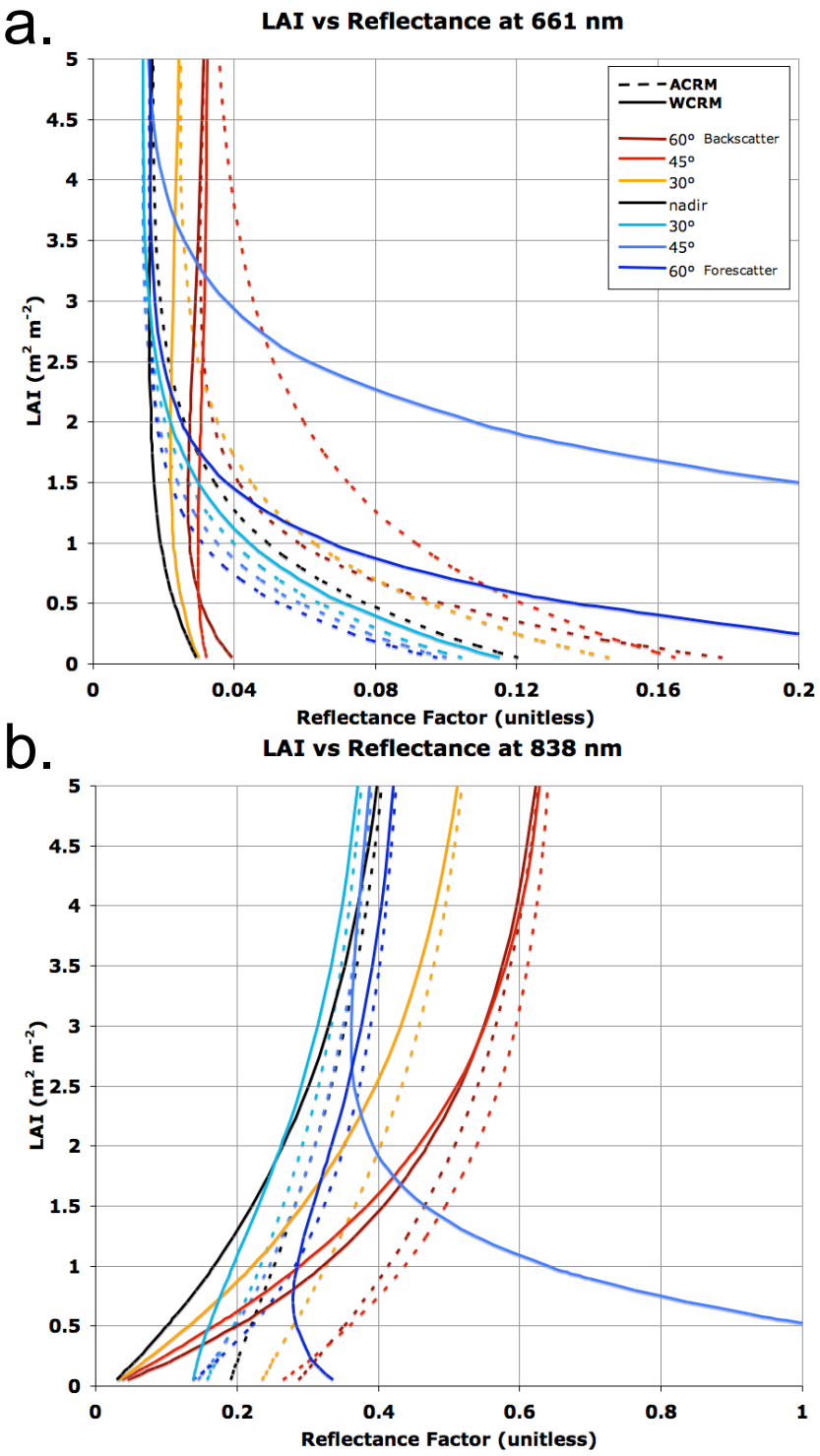

Figure 3-3. The ACRM and WCRM modeled relationship between LAI and canopy reflectance. The relationship is shown for several sensor zenith angles along the solar principal plane at a) 661 nm and b) 838 nm. Solar zenith angle was set to 45° for both models. The default soil was used for ACRM. WCRM was run with $\beta = 1$ and $\sigma = 0.06$.

coverage fraction, β, was set to 1, thus causing WCRM to simulate complete coverage of water over the substrate. The SPP reflectance was chosen because the most variation is expected along that plane and, hence, the most structure information. In addition, the presence of specular effects strongly affects the reflectance profile in this plane. Runs at other solar zenith angles indicated that the relationship between LAI and reflectance does not differ much for smaller solar zenith angles, but the relationship can as the sun gets closer to the horizon. However, as most remote sensing applications currently tend to not work well with very large solar zenith angles, such cases are left to future study. Plots of the modeled relationship between canopy reflectance and LAI are shown in Figures 3-2 and 3-3. Curves were plotted for a nadir view and for sensor zenith angles at 30° increments from nadir in the forward and backscatter directions along the SPP. Both 15° sensor zenith angle curves were omitted from each figure as they were not very different from the nadir curves and their removal reduced clutter.

The results show that performance appeared to be driven largely by the contrast between the background and foreground reflectance. In cases where the soil or water is more reflective than the vegetation, the LAI increases with decreasing canopy reflectance, as demonstrated by the curves in Figures 3-2 and 3-3. When the background is darker than the vegetation, LAI increases with increasing canopy reflectance. For ranges of LAI where these relationships hold, we can expect that the models can retrieve LAI. However, as the vegetation density increases, the influence of the background decreases. Furthermore, both models predict that for increasing vegetation density decreases shadowing, thus ultimately increasing canopy reflectance. Therefore, the negative relationship between LAI and reflectance for bright backgrounds can reverse as the vegetation becomes denser (i.e., increasing LAI). This situation leads to curves that are neither functions nor invertible. If it is known *a priori* that the LAI values being retrieved are confined to section of the curve that is invertible, then the model might be usable. So theoretically, retrieval of LAI in the presence of a bright background can be

limited to situation when LAI is known to be below or above a certain threshold value. However, the threshold would change with zenith viewing angle, thus limiting its applicability to most remote sensing applications. Also, for cases examined in this study, this threshold value typically occurred when the curve slope was very high over a large range of LAI, undermining predictive performance of the model inversion for most possible LAI values. Most curves became vertical, or nearly vertical, over some range of LAI values. It is mathematically impossible to retrieve a single LAI value for a given canopy reflectance value when the curve is vertical. Even very steep, non-vertical curves are limited as the large slope greatly magnifies any uncertainty in reflectance, which can be expected to be several percent or more for typical field and remote sensing reflectance measurements.

It can be concluded from Figure 3-2a that retrieval of LAI from the canopy reflectance is problematic for both WCRM and ACRM at 486 nm. The vertical or near vertical slope of the curves indicates that a single LAI value above 1.5 cannot be obtained for any given canopy reflectance in the blue. For the WCRM curves pertaining to far off-nadir LAI retrievals, the slope of the curves change sign over the range of LAI values, so the curve is no longer invertible for a larger range of LAI. The poor performance of these models to predict LAI stems from the lack of contrast between the background and the vegetation foreground. The performance of WCRM is slightly worse than ACRM at nadir and in the backscatter direction because of the darker background and the lower contrast that it affords. In fact, for very bright soils and sparse vegetation, the lack of multi-scatter effects may offer better potential to retrieve LAI, as was demonstrated by Chopping (2003) with sparse grasses in arid regions. However, except for the rare presence of a substrate of sand or bright clay, the blue wavelengths are not likely to be useful for typical tidal marshes.

Conversely, potential for LAI retrieval is very good for WCRM near the specular reflectance direction in the forward direction, where a very strong contrast is created by

the presence of sun glint. This suggests that sun glint could be used to probe the canopy for LAI, and perhaps other structure parameters. This idea was first suggested by Vanderbilt (2002). However, using WCRM for LAI retrieval using background specular reflectance is limited by knowledge of σ and β. The values of these parameters may need to be known before inverting the model, although the sensitivity of the inversion of WCRM to this uncertainty remains to be explored. Also, in the case of remote sensing imaging, it is also not clear whether variation in horizontal distribution of vegetation within pixels would not undermine the model assumptions of uniformity and thus adversely affect prediction performance. The potential of the specular reflectance in retrieving LAI from canopy reflectance appears at all visible wavelengths. However, the NIR curves in the specular direction are confounded by the bright vegetation foreground, causing relationships that are not invertible.

Figures 3-2b and 3-3a show that the potential retrieval of LAI for the modeled marsh is not good for the green band and even worse for the red. Conversely, the comparatively brighter background of dry soil affords better potential for ACRM to retrieve LAI values that are known to not exceed much more than a value of 2. Of course, this is subject to the aforementioned limitations regarding knowing that LAI is so constrained. The increased contrast between foreground and background seen for modeled terrestrial conditions provides the opportunity for ACRM to retrieve an LAI value over a large range of LAI. Conversely, WCRM curves suggest a lower potential for LAI retrievals over marsh canopies, which typically have inundated substrates or wet, dark organic soils and peat. Furthermore, green wavelengths are more subject to variation in reflectance contributions from phytoplankton, algae, and submerged vegetation in the aquatic substrate. Thus, these constituents produce considerable variation in the shallow water model at this wavelength. For low productivity water and low sediment load, the vegetation foreground should be comparatively brighter than the background. Conversely, productive waters or high sediment load can cause the

background reflectance to be closer to the canopy above, decreasing the contrast and hence performance in retrieving LAI.

Sensitivity of Model Inversion Technique

The LAI verses canopy reflectance curves indicate what is theoretically possible given the modeled relationship between LAI and canopy reflectance. However, the inversion of the model through the minimization of a cost function (see Equation 27) is affected by low contrast between background and foreground in ways that are not intuitive and can deceive a casual user of the model inversion. The inversion is an iterative process, which starts with an initial guess for LAI (or any set of one or more input parameters). This input parameter is then changed slightly and the cost function is checked for decrease. The input parameter continues to be systematically adjusted as long as the cost function continues to decrease. However, when the LAI verses canopy reflectance curve is has a very large slope (i.e., near vertical), the cost function does not change significantly. Therefore, the LAI value does not change much from the initial guess. If the initial guess is good, then getting a value near it may seem acceptable. But, what has happened instead is that the model inversion has only returned whatever it was given, regardless of the actual LAI value.

Figure 3-4 illustrates an example of this scenario. WCRM and ACRM were run to retrieve LAI from marsh BRF data sampled from a *Spartina alterniflora* canopy in South Carolina (Schill*, et al.*, 2004), which will be described further in Chapter 4. The initial value for LAI was set to the published measurement of 2.27. Retrievals based on NIR reflectance data yielded LAI values that were significantly lower than the published value, but the LAI retrieval based on blue reflectance appeared very accurate for every case. It was later noticed that the overall reflectance values were much lower than other similar reflectance measurements found in the literature (Artigas and Yang, 2005; Kearney*, et al.*, 2009; Schmidt and Skidmore, 2003). This brought the published LAI

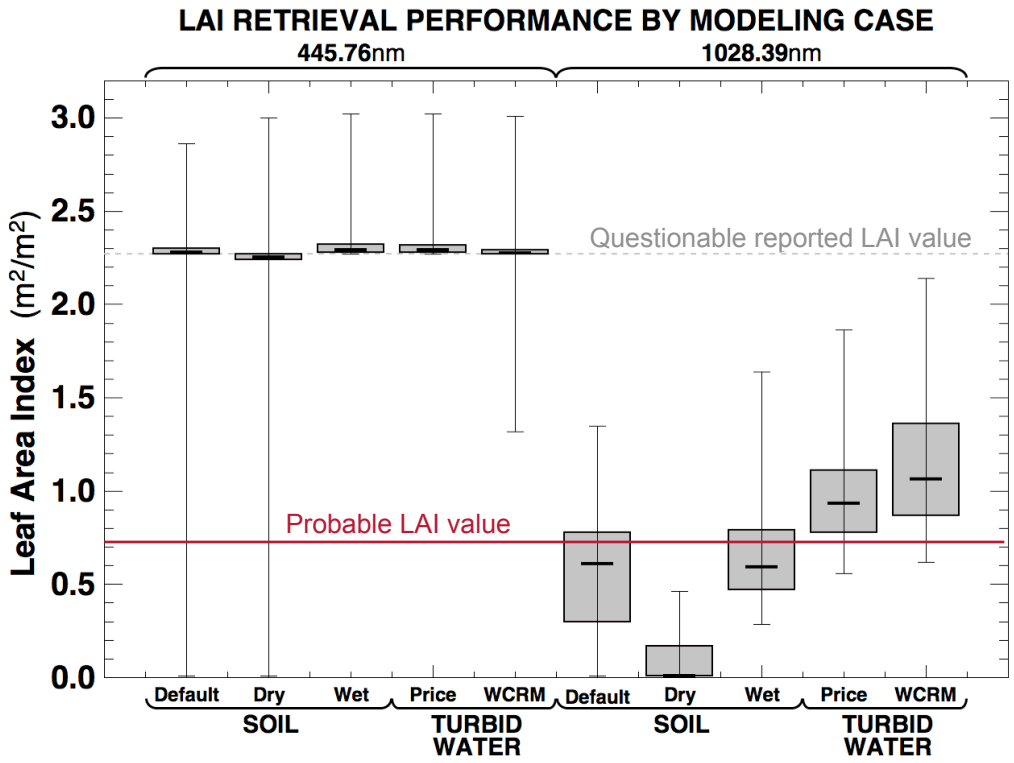

Figure 3-4. Box-whisker plot for the LAI retrieval for five modeling cases based on background spectra shown in Figure 3-1. The upper and lower extremes of the whiskers are the minimum and maximum, respectively. The bottom and top of the box indicate the lower and upper quartiles. The horizontal line near the center of the box is the median. The retrieval base on the blue reflectance has stuck on the initial value for LAI, which was set to a possibly questionable value. The actual value may be closer to the retrieval values based on the NIR reflectance.

and reflectance values into question. Although not completely exonerated, no problem could be found with the reflectance factors that would lead to about half the expected reflectance for a moderately dense canopy. However, an LAI value of 0.723 was found recorded in notes accompanying the data, which may be closer to the actual measured LAI value. As can be seen in Figure 3-4, the inversion based on the NIR reflectance values were much closer to the new LAI value, which further supports this as the actual value. Meanwhile, the inversion that was based on the blue reflectance had clearly become stuck on the initial guess for LAI, which by design was the target value.

To further emphasis this point, a Monte Carlo experiment was run with WCRM model to test the sensitivity of LAI retrieval to random variation of the canopy reflectance field. First, the WCRM model was run to produce canopy reflectances across the SPP. This was done at NIR and blue wavelengths, for a solar zenith angle of 45°, and for eleven sensor zenith angles going from 0° to 80° in the forward scatter and backscatter directions. Normal distributed random values (also know as Gaussian noise), were added to the simulated reflectances. This added noise was scaled relative to the backscatter reflectance range (i.e., the difference between the maximum and minimum reflectances along the backscatter half of the SPP) to simulate variation in vegetation density. The model was then inverted based on the noisy canopy reflectance in attempt to recover the original LAI value. The process of generating a canopy reflectance field, introducing noise, and retrieval of LAI through inversion was repeated 1000 times and then summary statistics were taken for all recorded deviations from the original LAI value. Figure 3-5 shows the summary statistics as the variation of the introduced noise is set to increasingly larger values. For each increment, the standard deviation of the introduced random values, or noise, was set to large values relative to the overall range of reflectance along the backscatter portion of the SPP. The results clearly indicate that the inversion based on blue reflectance is far less responsive to random variation in the SPP reflectances. As long as the variation in the reflectance field yields no significant change in the cost function, the retrieval cannot move far from the initial value for LAI.

As a side benefit of this experiment, it was also noticed that introduced noise caused no significant bias in the retrieved LAI value based on the NIR reflectance data. By the principle known as Jensen's Inequality (see pg 182 of Casella, 1990), this implies that over the range of variation introduced, the inverse of WCRM (with respect to LAI) is fairly linear. This indicates that retrieval of LAI is applicable to data aggregates. An important case of data aggregates are remote sensing pixels, which often contain reflectance values averaged over spatial scales much larger than the variation observed in

field data. This implies that although the inversion of WCRM to retrieve LAI from reflectance values found in remote sensing imagery would be sensitive to sub-pixel variation, as indicated by Figure 3-5, retrieved LAI should also be relatively free of bias.

Conclusion

The ACRM and WCRM models were used to generate curves that represent the theoretical relationship between LAI to canopy reflectance for various viewing geometries and wavelengths. It is was seen that contrast between the background and foreground reflectance drives the potential for successful retrieval of LAI from the canopy reflectance field. These curves demonstrated that the visible wavelengths afford poor conditions for retrieval of LAI by WCRM. The exception to that rule are cases that involve using specular reflectance, where the glint greatly increases the contrast. The idea of using specular reflectance to probe the canopy structure was originally explored by Vanderbilt (Vanderbilt*, et al.*, 2002). However, lack of knowledge about the surface roughness, σ, and water coverage fraction, β, may make it difficult to connect measured reflectance to a given LAI value. Further study is needed to determine the how these parameters affect the LAI retrieval by model inversion.

Conversely, the consistently dark background at NIR wavelengths provides an opportunity to retrieve LAI over a fairly large range of possible values. Retrieval of LAI based on specular reflectance is confounded by the high reflectance of vegetation at these wavelengths, which hence would probably be a poor choice for such a technique. For marsh surface conditions, the NIR wavelengths may be the best choice for retrieval of LAI from canopy reflectance. Without solid information regarding σ and β, the viewing directions that avoid specular reflectance from the sun would be preferable. The curves in Figure 3-3b indicate that viewing angles in the backscatter direction at a zenith angle of 45° or greater may be ideal for retrieval of LAI.

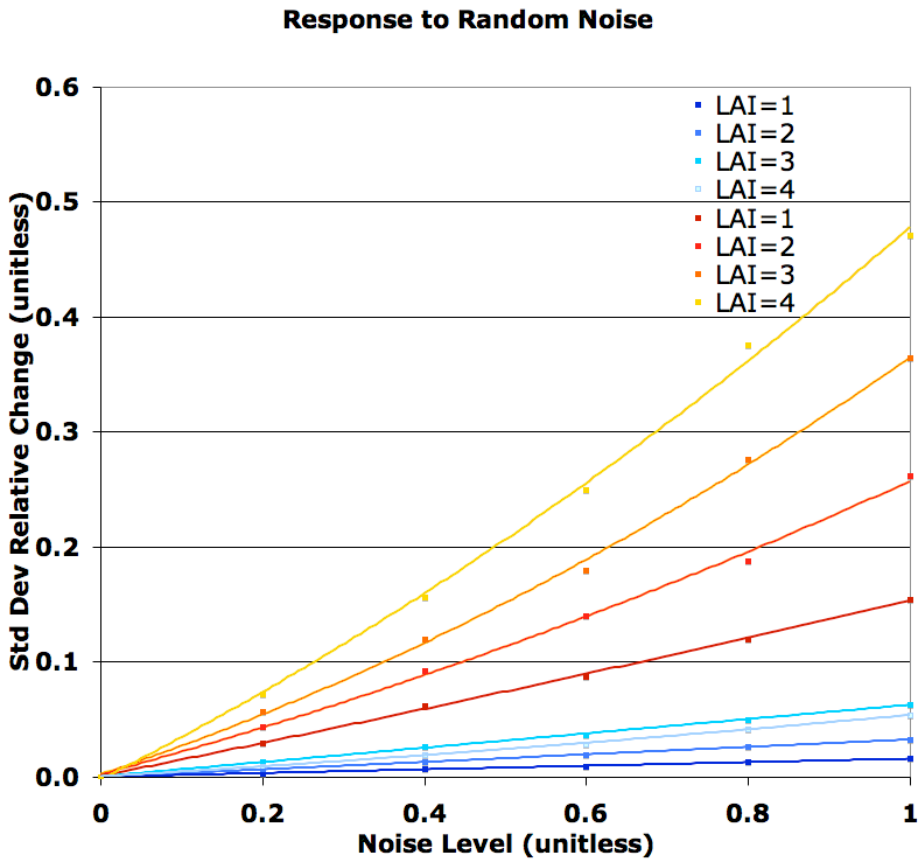

Figure 3-5. Variation in the retrieved LAI in response to variation introduced to the reflectance field. The retrieval of LAI is based on monochromatic, multiangular reflectances for two representative wavelengths for blue and NIR. See text for details of the experimental procedure. Noise level is the standard deviation of the introduced random values divided by the overall range of reflectance values along the SPP in the backscatter direction. Each symbol indicates the standard deviation of the relative difference between the original LAI value and the retrieved values. The curves are 2nd order polynomial fits.

When the slope of the curves depicting the relationship between LAI and canopy reflectance became near vertical, the inversion technique based on minimization of a cost function was also affected. However, rather than producing any LAI value, as a near vertical curve might suggest, it was found that inversion algorithm would tend to produce a retrieved LAI that is close to the initial value. This appearance of convergence on a reasonable value can be deceptive, as illustrated in an example scenario. It was further shown that this sluggish response is fairly robust to random variation in the measured

reflectance field. As a positive outcome, analysis of this behavior also demonstrated that retrieval of LAI based on NIR reflectances are likely not to be biased by the nonlinearity of the model when applied to remote sensing applications, like imagery.

Chapter 4 The Transect Experiment

Introduction

Reflectance and LAI measurements were collected along transects for different marsh canopies to explore whether the model can be applied to remote sensing imaging data. For each transect, reflectance was measured at six angles with a narrow field of view and were then averaged to a scale closer to pixels of an airborne or spaceborne imager. This study included three sites, each with mostly monospecific populations (i.e., one dominant species). In each, 30.5 m transects were measured at six different angles. Given the potential connection of NIR reflectance and LAI, the data are compared with WCRM predictions at those wavelengths given measured LAI values. The results of the comparison suggest that LAI may be retrieved when the canopy has little dead or senescent vegetation, while conversely, the reduced reflectance stemming from the presence of these materials may cause the vegetation canopy reflectance model to predict LAI values that are much lower than what might be measured with a LI-COR LAI-2000.

Data and Methods

Measurements of LAI and BRF were taken in the Blackwater Marsh, which is part of the Chesapeake Marshlands National Wildlife Refuge Complex managed by the U.S. Fish and Wildlife Service. Data were collected along Maple Dam Road, about 20 km south of Cambridge, Maryland USA (see Figure 4-1). All measurements were taken in mid-afternoon on 1 September 2008. Most of the equipment used for the transect experiments is shown and described in Figure 4-2. Measurements were made under clear-sky conditions to minimize uncertainty stemming from fluctuation in the canopy irradiance. All reflectance measurements were made within a few hours of solar noon and LAI measurements were made from late afternoon to dusk. Equipment, such as the

instrument boom, were set up and broken down at one of the gates along Maple Dam Road or Shorter's Wharf parking lot. Set up and initial calibration took about twenty minutes.

For the late summer measurements of the transect experiment, the sky was generally clear with a few small cumulus clouds on the far horizon. Temperatures were < 90 °F (32 °C), the relative humidity was high, and the surface conditions were very wet with relatively high water levels. Table 4-1 summarizes the conditions for each site of transect experiment. Site 1 was chosen as representative of the highly prevalent *Schoenoplectus americanus* at Blackwater Marsh. Site 2 showed lower density cover, including a mix of shorter *Schoenoplectus americanus* and *Spartina patens.* The landscape around Site 2 also had more variable vegetation coverage than what was observed at Site 1, with other more monospecific canopies and open water nearby. Site 3, which was in close proximity to Site 2, was predominantly *Spartina alterniflora,* with intersperse *Spartina patens and Distichlis spicata.* Interestingly, although this mixed-specie canopy was shorter, and appeared to

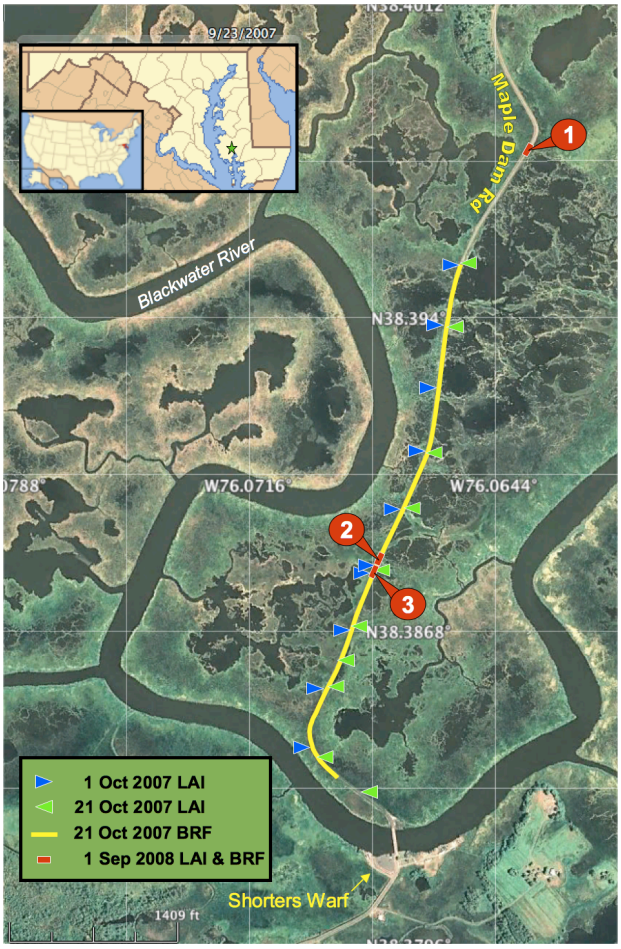

Figure 4-1. Transect Study Site. Green and blue pennon markers indicate positions of LAI measurements for the long transect experiment. Yellow curve shows the segment of Maple Dam Road traverse during the same experiment. Red boxes indicate where LAI and reflectance were measured for three sites as part of the short transect experiment, each identified with numbered red circles. (Inset: Dept of Commerce, via Wikimedia Commons)

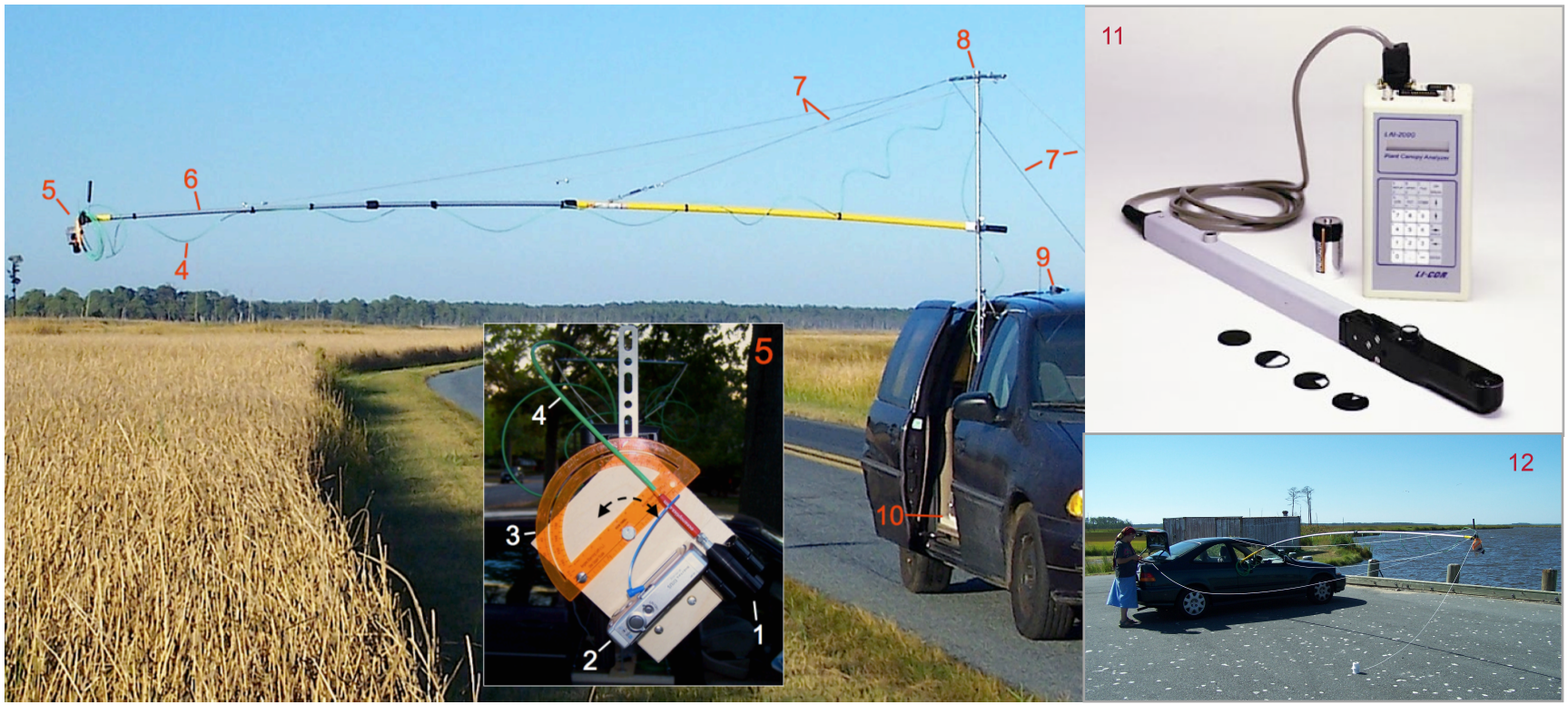

Figure 4-2. Transect experiment apparatus.

1. OOI Gershun tube probe with 14° aperature.
2. Canon Digital Ixus camera (WiFi enabled).
3. Protractor.
4. Optical fiber, 500 μm thick, 20 m long.
5. Instrument probe mount.
6. Extendable boom, 5.2 m, max 6.7 m.
7. Guy cables.
8. Boom mast.
9. GPS unit and cable.
   a. 2007 - Garvin Etrex.
   b. 2008 - GlobalSat Tech Corp BU353 USB GPS Receiver.
10. Boom mask platform, OOI USB2000+ Spectrometer, computer console.
11. LI-COR LAI-2000 Canopy Analyzer with control unit and caps.
12. Alternative small-vehicle setup with guy cords (2008).

Table 4-1. Conditions observed in the canopy for the short transect experiment by site. Hgt indicates the measured canopy height in meters. LAI was averaged from five measurements (in units of m^2m^{-2}). LAI standard deviation and root mean squared standard error are given below the average.

Site	Hgt (m)	LAI Mean StdDev Std Err	Species	Cover Density	Surface
1	1.2	**3.7** 0.24 0.22	Mostly *Schoenoplectus americanus*, with *Spartina patens* inter-dispersed.	Consistently dense coverage.	Surface is soggy. Tide appears high.
2	0.9	**3.1** 0.60 0.38	Mostly *Schoenoplectus americanus*, with some *Distichlis spicata* inter-dispersed.	Moderately to highly dense, with patches of sparse growth.	Small ponds and interstitial water present.
3	0.5	**3.9** 0.60 0.28	*Spartina alterniflora* with occasional patches of *Spartina patens;* some *Distichlis spicata* present.	High with patches of moderate cover.	Soggy with small ponds. Browning of *S. alterniflora* observed.

have less foliage than observed at Site 1, the average measured LAI was the highest of the three sites. The surface conditions were better drained, but more variable.

BRF for all transects used in this study were taken with an Ocean Optics USB2000+ spectrometer (OOI) with a 20 m optical fibre cable and a Gersun tube probe with a 14° aperture. The probe was situated on the end of an extendable instrument boom and could be set at any zenith angle. Suspended continuously over the marsh canopy, the instrument boom was carried by a motor vehicle down Maple Dam Road, which cuts across the marsh. Although measurements were taken on either side of the road, only those taken on the west side are considered in this study because the larger number of ponds against the road on the east side significantly reduced the number of canopy measurements. Short transect sites were made only on the west side. The boom was extended about 5 m from the vehicle. Taking into account the road side and mowed area (~3 m), the instrument probe was deployed about 2.1-2.7 m into the canopy and at a height above the top of the canopy of about 1 m for the long transect experiment and about 0.3 m for the short transect experiment. During the long transect experiment, the

BRF was sampled with the instrument probe pointing in the nadir direction; set at 60° and 45° in the backscatter direction; and then at 45° in the forward scatter direction. For each site of the short transect experiment, the instrument probe was set pointing at nadir; at 60°, 30°, and 45° in the backscatter direction; and 30° and 45° in the forward scatter direction. Other information, such as marsh conditions and species composition, were recorded on predefined forms during collection of LAI point measurements and later logged into a spreadsheet.

The spectrometer was configured with a 200 μm aperture and internal cylindrical lens over a 2048 channel CCD array to maximize sensitivity. This was necessary in order to capture light from the darker surface conditions found in the marsh and to compensate for signal attenuation caused by the optical fibre. The instrument sampled the vegetation spectrum at 1 nm intervals from 340 nm to 1028 nm, but with spectral resolution of about 10nm. The instruments radiometric sensitivity reaches its maximum for wavelengths near 400 nm and decreases linearly to near zero just above 1 μm. Measurements were collected using vender software on MacBook Pro laptop via a USB cable. To get reflectance factor measurements, the software processed the ratio of dark-count (DC) corrected counts (dn) from the vegetation canopy to that of a reference panel. DC counts were taken by measuring with the cap over the instrument aperture. The system features a continuous electronic DC correction, which was activated during any use of the spectrometer. The spectrometer was set to integrate over 2 ms intervals, and the average of 100 samples was recorded to improve the signal-to-noise. The instrument and data collector could only record a measurement every 1 to 2 seconds, varying for unknown reasons by a factor of two between transects.

Calibration of the reflectance factor measurements were done using a gray Spectralon™ reference panel. This panel was also characterized using the spectrometer and a stable light source and its reflectance was factored into the BRF data during analysis. A Savitsky-Golay filter (Savitzky and Golay, 1964) was applied to the resulting

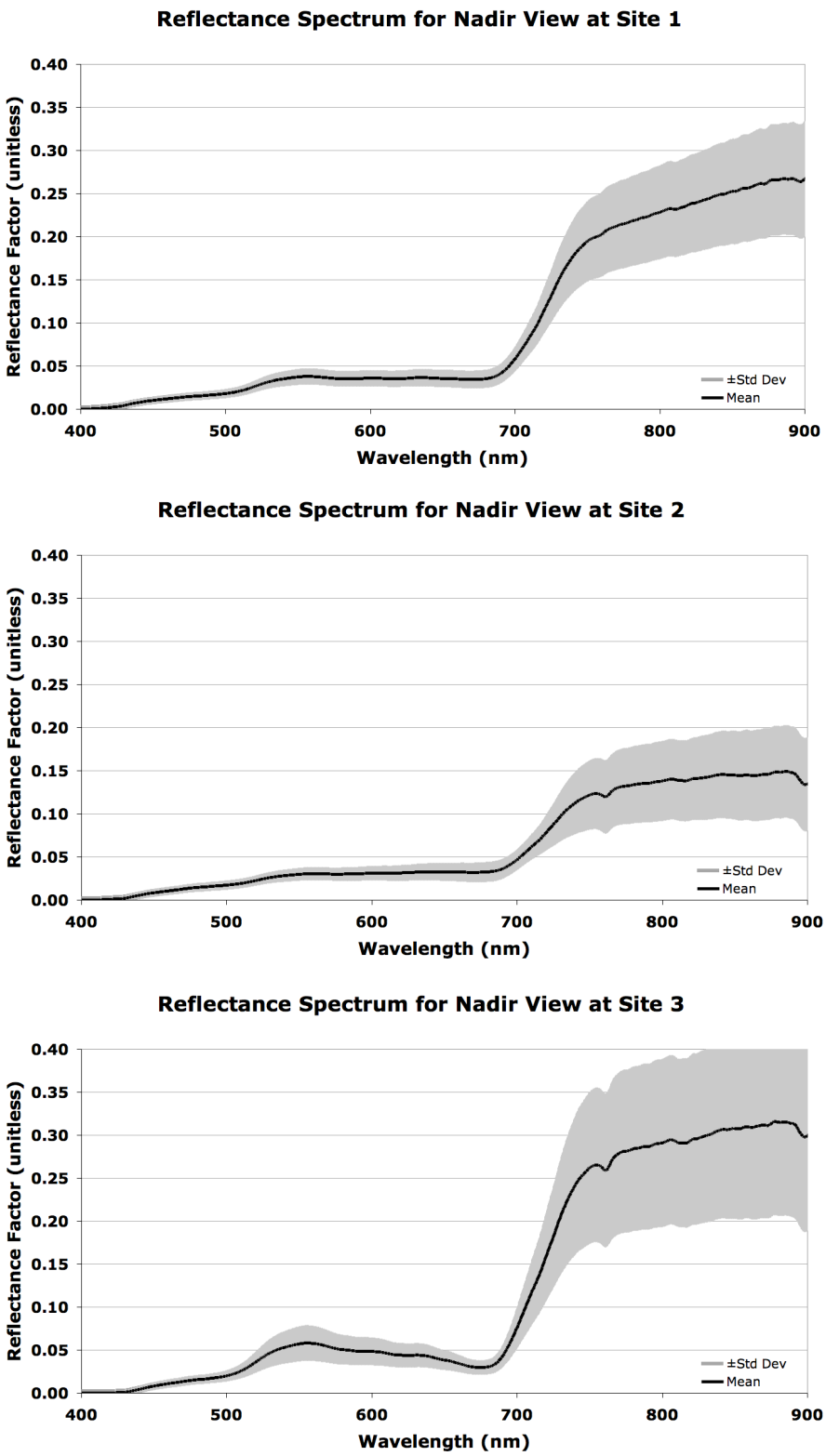

Figure 4-3. Mean of the reflecance spectra Sites 1, 2, and 3. The gray region indication plus and minus one standard deviation of the reflectance at each wavelength.

calibrated reflectance spectra to reduce the noise as a function of wavelength (Schmidt and Skidmore, 2004).

Positioning of the data was done with a GlobalSat Tech Corp BU353 USB GPS mouse receiver. However, the GPS mouse receiver was not used to geolocate individual short transect measurements as they were being sampled at spatial intervals much smaller than the uncertainty of the GPS position. Instead, the reflectance measurements were simply averaged over the 30.5 m transect for each sensor angle.

LAI measurements were made after the site reflectance measurements using a LI-COR LAI-2000 plant canopy analyzer, including one LAI-2050 optical sensor and one LAI-2070 data collector. The fisheye lens of the optical sensor was covered by a cap with a 90° section opening. The opening was oriented to mask the sun and the instrument operator (LI-COR, 1992). Each LAI measurement included two calibration measurements, each followed by four in-canopy measurements (i.e., a total of eight below-canopy measurements). For a 1 m canopy height, the sensor samples canopy up to 3.5 m laterally. LAI was sampled at 6.1 m intervals along the transect of each site to produce several independent measurements along the transect. Thus, coincident with the reflectance measurements of each site were five groups of LAI measurements (a total of 40 in-canopy measurements). For hummocky canopies, where vegetation was observed to grow in clumps, one in-canopy measurement was within a clump for every in-canopy measurement made between clumps, as an attempt to compensate for the stark variation in vegetation density within the canopy. This situation was most notable for poorly drained canopies of *Schoenoplectus americanus* during the various campaigns of 2007 and 2008. This technique was only applied conservatively for Site 2 during this transect experiment.

Because these canopies are largely erectophile, light from the zenith reaches more deeply into the foliage, causing more signal scatter events in the blue. As a result, the outer ring of the plant canopy analyzer received additional light from the canopy itself,

causing it to underestimate LAI (LI-COR, 1992). This phenomenon has also been reported in the literature for marshes in particular (Stroppiana*, et al.*, 2006). The instrument manufacturer suggested alternatives for addressing this negative bias in LAI, including reprocessing the transmittance measurements with the outer ring excluded (LI-COR, 1992). In this study, the method developed by Lang (1987) was used, which statistically reduces the weight of the outer ring. Use of either method significantly increased the LAI measurements taken in this study.

Results and Discussion

Figure 4-3 shows the mean reflectance spectrum at nadir for each site. As was observed in the field, the sites varied in the relative amounts of green and dead vegetation. Site 3 was seen to have mostly dense thick grass (*Spartina alterniflora*), with comparatively less detritus than the other sites, which given its spectra the strongest reflectance in the green and NIR, and lowest red reflectance, of all three sites. Site 1 was populated with dense sedge (*Schoenoplectus americanus*), which gave its spectra a strong NIR signal, but the large quantity of senescent and dead vegetation in this canopy gave higher red and lower green reflectances than Site 1. Site 2 had more variable coverage, including sparse patches. The Site 2 canopy was populated with mostly the same species of sedge as Site 1, but mixed with grass (mostly *Spartina patens*). Some large holes (> 30 cm), where the substrate was visible, could be seen in the Site 2 canopy. The mixture of the senescent and dead vegetation associated with the sedge and the less dense cover caused spectra with overall lower reflectance. In addition, Site 2 spectra have the same senescent appearance as Site 1, but with a much flatter NIR plateau. However, the average measured LAI for Site 2 was 3.1.

The spectra taken at each site were averaged over the three spectral regions, including from 440 to 460 nm, from 650 to 670 nm, and from 790 to 810 nm. These arithmetic means are shown in Figure 4-4 for each sensor zenith angle of the transect

experiment. The large amount of variability in the blue and red means suggest that these are not useful for LAI retrievals given the sensitivity analysis of Chapter 3. The NIR reflectances as a function of angle seem better behaved, separating out in the order expected given the associated LAI values given Table 4-1. The NIR reflectances produce the concave up profile expected for a canopies that tend to erectophile. The visible wavelength measurements are very low, but an upward trend from the forward to backscatter directions is significant. This is likely caused by shadowing, which is more visible in the forward scatter direction. However, the differences in blue and red reflectance between sites do not appear significant.

WCRM was run for the average measured LAI of each site to predict the marsh canopy reflectance for the transect experiments. Default values for all other model input parameters describing the vegetation, except the leaf angle distribution parameters were set to the

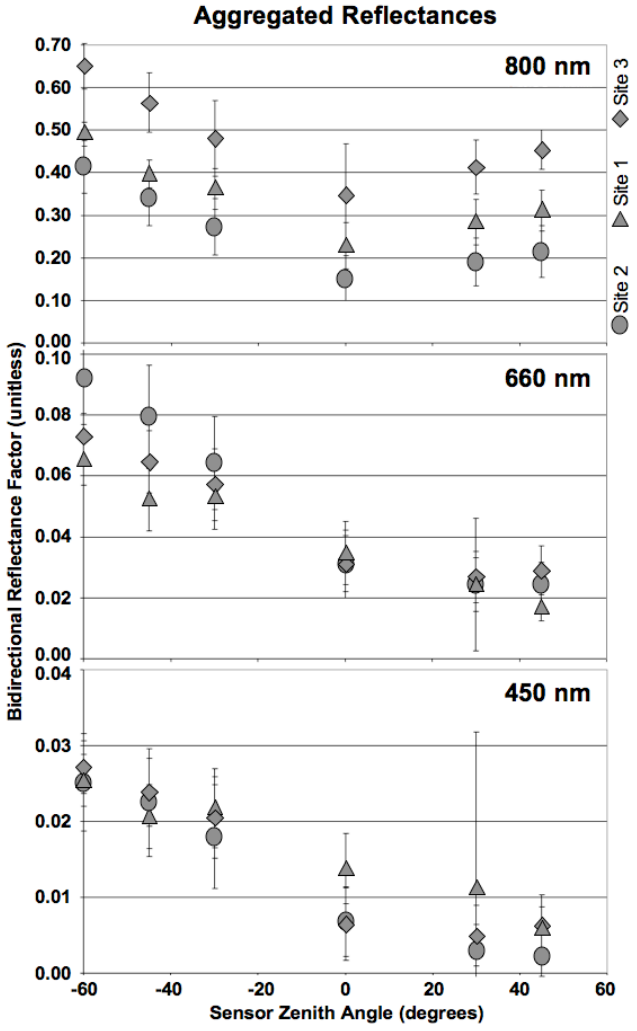

Figure 4-4. Average reflectance across 30.5 m transects at three sites. Three wavelengths are presented for the three sites of the short transect experiment. Negative sensor zenith angles indicate the backscatter direction. The transect is near the SPP for each site and some limited specular reflectance was observed in the unaggregated data near 30° in the foreward scatter direction, but is only noticeable for Site 1. The bars indicate the sample standard deviation. The error in the mean is smaller than the plot symbols.

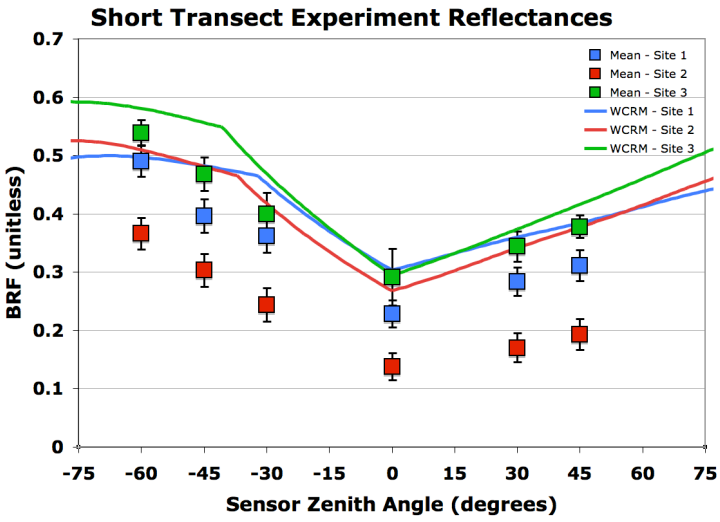

Figure 4-5. Mean and modeled reflectance values. Reflectance for 800 nm was averaged across each transect at six sensor zenith angles (symbols). WCRM was then used to model reflectance for each transect based on average measured LAI (curves).

maximum amounts, indicating a predominantly erectophile canopy. Solar zenith and azimuth angles were calculated for the location of each site at the time that the measurements were taken. The modeled canopy reflectances along the solar principal plane were plotted over the averaged reflectances at 800 nm. The plot of these two data sets is shown in Figure 4-5. The reflectance values in Figure 4-5 were adjusted from those plotted in Figure 4-4 to account for an anomalous loss of responsivity in NIR detectors during the reference panel measurements at Sites 2 and 3. To compensate, the reflectance measurement for Site 1 was normalized to the solar zenith angles of Site 2 and 3. This addressed the anomaly for the shorter wavelength NIR detectors, including 800 nm, but little to no response could be seen above 928 nm (not shown in Figure 4-3). This improvement, however, removes any compensation for changes in atmospheric conditions, but the atmosphere was extremely clear and stable during the experiment. This adjustment also removes any drift in repsonsitivity at other wavelengths. However, at 800 nm, the correction causes only a slight change in Site 1, essentially pushing its reflectance values closer to Site 3. Thus, the closeness of these values in Figure 4-5 cannot be connected to their coincidental closeness in LAI values. Site 2 reflectance was lowered very slightly, and not significantly in comparison to the in canopy variation. Again, the reader is advised to

disregard any apparent relationship between adjusted differences between Site 1, 2 and 3 reflectance and LAI.

Instead, what the comparison does indicate is that the model follows the profile in the data fairly well, but there is a large offset for Site 1 and especially Site 2. As a results, the inversion of the WCRM model to retrieve LAI values using the multi-angular reflectance data at 800 nm produced large underestimates for LAI in comparison to the measured values (LAI values of 1.0 and 2.0 for Sites 1 and 2, respectively). The inversion algorithm converged on lower values of LAI to account for the negative offset in reflectance. The drop in reflectance at these sites is mostly attributed to the large amount of dead standing stock and detritus. In attempt to get a more accurate leaf spectrum for the canopy, the WCRM was run in inverse mode with fixed LAI values in order to retrieve the input parameters for PROSPECT model. However, both WCRM and ACRM failed to produce leaf optical properties that was representative of dead or even senescent leaves.

It was also noticed that the *hot spot* predicted by the ACRM component seemed high for the NIR. The *hot spot* effect occurs when shadows are eliminated from view because the direct illumination source is exactly behind the observer or sensor (and the observer's or sensor's shadow is significantly small in the field of view). With the large amount of multi-scatter amongst leaves at NIR wavelengths, however, this effect would expected to be softened by the corresponding reduction in shadows by the diffuse flux. The strong effect predicted by WCRM (via ACRM) seems to contradict such an intuitive result. The ACRM model employs an empirical profile for the *hot spo*t (Kuusk, 1991), which clearly does not depend on leaf reflectance (only leaf size and density). Further investigation of this effect and multi-scattering processes might provide more insight into what should happen at NIR wavelengths.

Conclusions

Multi-angular, hyperspectral reflectance and LAI measurements were taken along linear 30.5 m transects of a marsh canopy at three sites. Measurements along a 1.5 km transect were also taken and compared to the short transect results. The results show that aggregated above-canopy reflectance potentially could be used to retrieve LAI for given viewing and illumination directions when the data are averaged spatially. However, when the canopy reflectance in the NIR is influenced by the presence of dead or senescent plants, the model inversion underestimates the LAI. Allowing the PROSPECT parameters to vary during the model inversion did not change the results. Further experimentation with PROSPECT demonstrated that the version employed could not produce a dead or senescent leaf spectrum given realistic input values. This can be viewed as a limitation of the WCRM model that is inherited from ACRM. Therefore, this area needs to be improved for marsh canopy applications because many species of marsh plants retain a dead standing stock in the canopy.

In addition, this result identifies a distinction between LAI based on above-canopy reflectance in the NIR and LAI based on below-canopy transmittance in the blue, as employed by the LI-COR LAI-2000. The latter includes all matter obstructing light from penetrating the canopy in the estimate of LAI and, in fact, the manufacturer suggests that the measurement made by LAI-2000 plant canopy analyzer may be better termed a *Foliage Area Index* (FAI) (LI-COR, 1992). In other words, the LAI-2000 will greatly overestimate the amount of green LAI in canopies populated with many marsh species, such as *Schoenoplectus americanus*, because of the amount of dead vegetation present. Conversely, the above-canopy reflectance is sensitive to the amount of dead vegetation and will produce a lower LAI. Therefore, it can be difficult to get these to techniques to agree for such canopies. Using information from the green wavelengths at single or multiple viewing angles may provide information that would improve a green LAI estimate above the canopy.

Furthermore, unlike the below-canopy approach, the above-canopy approach can be influenced by changes in the background. High sediment loads from disturbances, such as strong precipitation events, could change the contrast between the foreground and background reflectances in the NIR and decrease the methods accuracy. This could limit the conditions for which this approach is applicable. More research in this area is warranted to understand how surface conditions could affect LAI retrieval using WCRM or similar approaches.

Chapter 5 The Marsh BRF Experiment

Introduction

In 2000, the reflectance spectrum of an inundated *Spartina alterniflora* canopy was heavily sampled over the entire upwelling hemisphere (i.e., sampling over viewing directions) as the sun changes position throughout the day, providing BRF data for various illumination directions (Schill*, et al.*, 2004). This is a unique data set for exploring the properties of marsh reflectance for a large varieties of viewing and illumination conditions. This chapter investigates using these data and the WCRM model.

In this study, the marsh BRF data were used to show that WCRM is an improvement over the original terrestrial vegetation canopy reflectance model (ACRM). Comparison with the original version of the model, ACRM, indicates that WCRM reduces biases stemming from specular reflectance, and is thus an improvement over ACRM for application to canopies with an aquatic background. The data are then compared to the leaf reflectance spectrum for *S. alterniflora* to determine what viewing and illumination directions were optimal for discerning the vegetation signal. The resulting correlation were compared to similar correlations based on modeling with WCRM and ACRM.

Data

The canopy BRDF was sampled using the NASA Sandmeier Field Goniometer (SFG) (Sandmeier, 2000; Sandmeier and Itten, 1999) at two sites in South Carolinian marsh over the course of two days in 2000, one day in March and one in October (Schill*, et al.*, 2004). The marsh canopy at both sites were monospecific and populated with *Spartina alterniflora*. The horizontal base of the NASA SFG was a circular rail, with a

radius of 2 m, called the *azimuthal ring*. Eight PVC pipes were sunk into the marsh soil to raise the azimuthal ring level with the top of the canopy. On top of the azimuthal ring sat a half-circle arc called the *zenith arc*, which could rotate a full 360° of azimuth. Figure 5-1 gives a photograph of the SFG deployment at the site of interest. The NASA SFG employed a GER-3700 spectroradiometer (GER, 1997) that moved on a sled mounted to the zenith arc (see Figure 5-2). A Spectralon™ reference panel situated at the top of the zenith arc was used to determine reflectance. The reflectance was taken to be the ratio of the dark-count corrected digital numbers (dn) taken of the canopy to those of the reference panel. The canopy reflectance spectrum was sampled over 704 bands ranging from 312.71 nm to 2403.81 nm, with a sampling varying rate that increased from about 1.2 nm at the blue end of the spectrum to about 8.6 nm at the NIR end. When pointed towards nadir, the intersection of the GER-3700 field-of-view and the top of the canopy was approximately a 10 centimeter disk. This was measured from 11 positions along the zenith arc, with sensor zenith

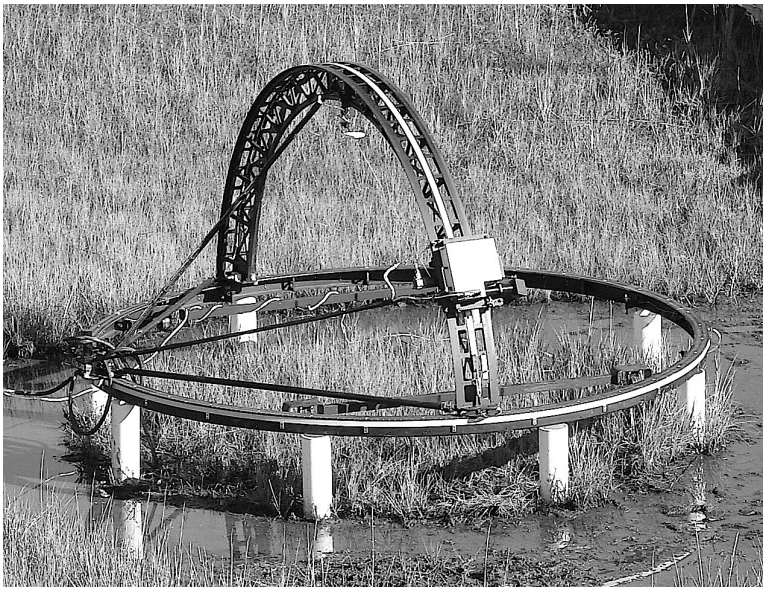

Figure 5-1. The NASA Sandmeier Field Goniometer. The entire system (sans computer) is shown deployed at the Boardwalk Site in October of 2000. Photograph provided courtesty of Steven Schill.

Figure 5-2. The GER-3700 spectro-radiometer on its sled. The sensor is positioned here for a nadir measurement. Note the moveable reference panel just below the zenith arc. Photograph provided courtesy of Steven Schill.

angles ranging from -75° to 75°, where a negative value indicates the backscatter direction. The first 11 measurements were taken along the solar principal plane (SPP) and then along five additional planes rotated from the SPP in a counterclockwise direction in increments of 30° of azimuth. Furthermore, 10 measurements were made at 2° intervals along the SPP, centered on the backscatter "hot spot." Each suite of measurements, totaling to 76 spectra, was completed in 8 minutes to minimize the effects of changing illumination. A suite of measurements was made for 13 different times of day, starting at 8:00AM EDT and ending at 4:00PM EDT, producing at total of 988 spectra per site, per day. In this study, the October data from the Boardwalk Site were used because of better data quality (Schill, 2006).

Figure 5-3 shows the most prominent features of the reflectance along the SPP. The spikes seen at the forward scatter direction are fairly coincident with the position of the solar specular angle. In addition, examination of these spikes over time showed they increase with solar zenith angle. That specular reflectance as the source of spikes was further supported by the facts that Fresnel reflectance would similarly increase with solar zenith angle and that that other reflectance processes, conversely, would decrease with growing shadows.

A remarkable feature is the general increase of reflectance in the backscatter direction, especially in the NIR. This increase largely maintains the upwards concave shape of the BRDF that is expected with a grass canopy. A reasonable hypothesis is that the direct illumination of the canopy from below by specular reflectance is brightening the entire canopy in the backscatter direction. Roberts suggested this process as an explanation for his observations of greater than expected NIR reflectance for marshes along the Gulf of Mexico (Roberts, 2011). The first principles underlying the WCRM model predict that glint is greatly attenuated by the interception of the reflected light by canopy leaves and stems. As a consequence, the same intercepted light would likewise be reflected backwards diffusely by the canopy. Furthermore, this would be more

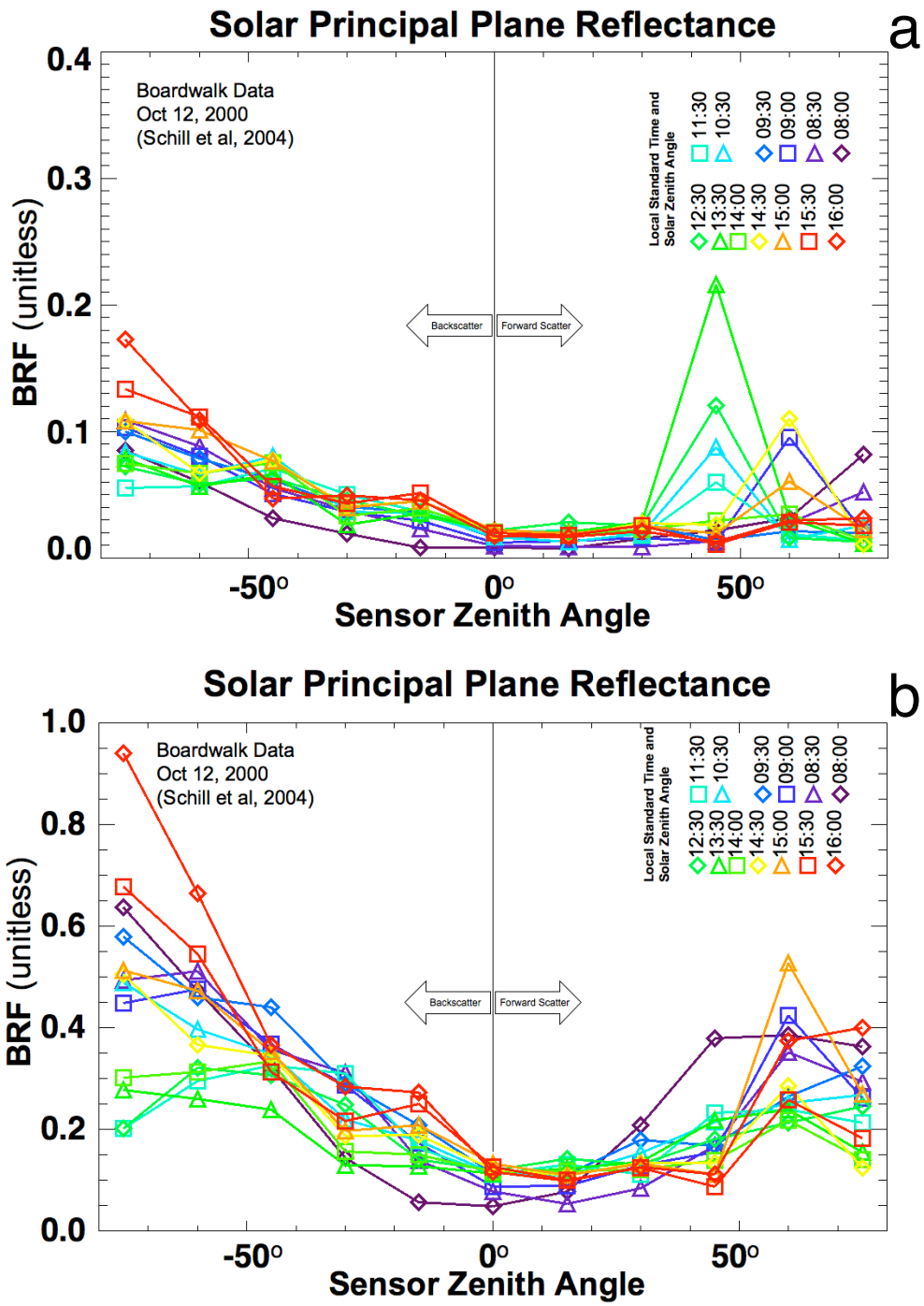

Figure 5-3. SPP reflectance for a *Spartina alterniflora* canopy taken for thirteen times of day, on 12 October 2000 at the Boardwalk Site. Plot a) gives the reflectance at 446 nm and plot b) shows the reflectance at 1028 nm. The key in upper righthand corner of each plot assigns symbols for each time of day. Each time symbol in the key is positioned horizontally to indicate the corresponding solar specular reflectance angle for that time on the horizontal axis. The coincidence between the solar specular angle and the spikes in the reflectance data implicates specular reflectance as their source.

prominent in the NIR, but some would still be observed in the visible, as indicated by the data in Figure 5-3. However, closer analysis of the underlying physics indicates that the increase in backward diffuse flux resulting from forward specularly reflected light should be limited to what can be produced by Fresnel reflectance off the water's surface. That would be between 2 and 3 percent for typical viewing and solar zenith angles in remote sensing applications. Furthermore, although higher zenith angles would exhibit a noticeable increase in specular reflectance, the canopy transmittance likewise decreases, reducing such an effect. Therefore, an increase in backscatter reflectance by such a mechanism is not likely for typical remote sensing configurations. However, a rise in backscatter reflectance for early morning and late afternoon hours might be possible where canopy sides are exposed (e.g., on the edges of water bodies).

Finally, although position of the data indicate a solar specular cause, the relative size between the visible and NIR spikes does not. There appears to be some correlation at 60°, but this is less apparent at 45° or 75°. The spectrum of glint is expected to be relatively flat over the corresponding range of wavelengths. The best explanation for this is a matter of scale. At the scale of this experiment, individual plants can significantly affect the measured reflectance. If fewer plants were in the sensor field of view that would increase the likelihood of a glint event near the specular direction. Conversely, the same lack of obscuring plant material in the visible would likewise decrease the overall measured reflectance in the NIR. As the reflectance spikes in the visible are comparable to the NIR reflectance, and the glint spectrum is flat, it could be that a similar glint spike in the NIR is simply replacing the lost reflectance stemming from correlated gaps in the canopy near the specular direction. The sensor geometry and atmospheric scattering could also be a contributor to this effect. The angular sampling of the sensor 15° instantaneous field of view (IFOV) is coarse compared to the 1/2° angular radius of the Sun. Therefore, highlights in the field-of-view could be dominated by the sun or sky irradiance near the solar disk, which would be stronger in the blue. This may have

increased the specular spikes in the blue for some cases, particular those seen at the higher zenith angles of 45°. Unfortunately, this effect is not well represented by the first-principle assumptions made by the WCRM model and further work should be done to improved prediction of this phenomenon.

Model Reflectance Comparison

WCRM and four configurations of ACRM were used to reproduce the canopy reflectance field for the SFG data. The comparison considered visible reflectance values, which displayed unambiguous glint effects. To simulate the canopy reflectance, default input parameters were used. Only LAI was attempted to be retrieved using the model inverse, because the actual LAI value for the canopy was unclear. The quality of such an inverse for visible wavelengths is suspect, however the visible reflectance field was shown in Chapter 3 to be fairly insensitive to choice of LAI value. In fact, the resulting modeled reflectance fields did fit the data fairly well. The inversion also facilitated the default run of ACRM, which involves retrieving the first two Price function coefficients.

The different configurations of ACRM included a default case and three other cases using different backgrounds (as shown in Figure 3-1). For the default case, the first two Price function coefficients are retrieved through the initial model inversion along with LAI. In this fashion, ACRM attempts to account for the bulk of the background reflectance while retrieving the vegetation structure parameter. In the three other cases, LAI was retrieved with a fixed background reflectance, represented by Price function coefficients. These included spectra for dry soil, a wet soil, and turbid water. ACRM only takes four Price function coefficients to describe the background spectrum, and does not take an entire spectrum as an input parameter. Thus, Price function coefficients for the each spectrum were derived by multiplying the spectrum by a Moore-Penrose inverse of the Price four-vector basis. In the last case, the modeled turbid water spectrum used in the inundation simulation was used for the LAI retrieval test. Applying the turbid water

background to ACRM primarily differs from the full WCRM model only by the omission of the aquatic calculations pertaining to the passage of light across the air-water interface and the use of the Walthall soil BRDF model (1985). In examining photographs of the SFG site, one can conclude that these three background spectra were progressively closer representations of the actual background spectra.

Each modeling case was run in the forward direction using the input parameters from the initial inversion. The resulting modeled reflectances were then compared with the field measurements. Figure 5-4 shows the mean error and root mean squared error

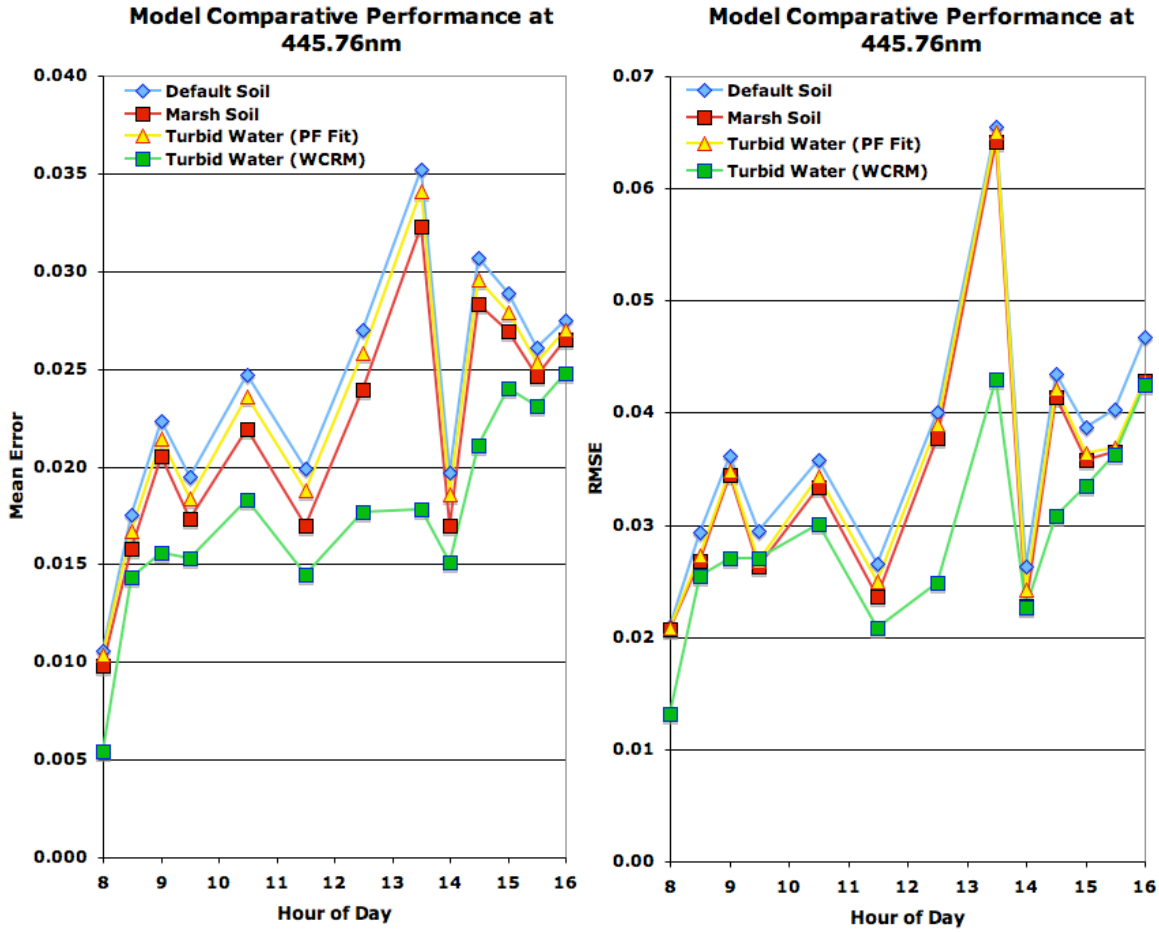

Figure 5-4. The residual bias along the SPP for each modeling case as a function of time. For all time periods, the SPP residual bias at 445.76 nm for WCRM, given by the mean difference between modeled and measured results, was the smallest of all modeling cases. This is interpreted to mean that WCRM better predicts the marsh reflectance field because it can reduce the contribution to the bias due to glint.

(RMSE) along the SPP between the "fitted" and measured reflectance at 445.76 nm as a function of time. For simplicity, all cases are plotted except wet soil, which followed the other curves closely. In nearly every case, WCRM matched the observed reflectance with a smaller residual error and bias than the other modeling cases. The improvement WCRM provides for both statistics are most notable along the SPP. This can be explained by the fact that WCRM makes a prediction for specular reflectance, while ACRM does not. Figure 5-5 illustrates how this can lead to biases in the fit of the residual.

Figure 5-6 expands beyond the SPP and considers the mean error for all azimuthal planes and all time periods. WCRM again shows a lower bias, which is likely being

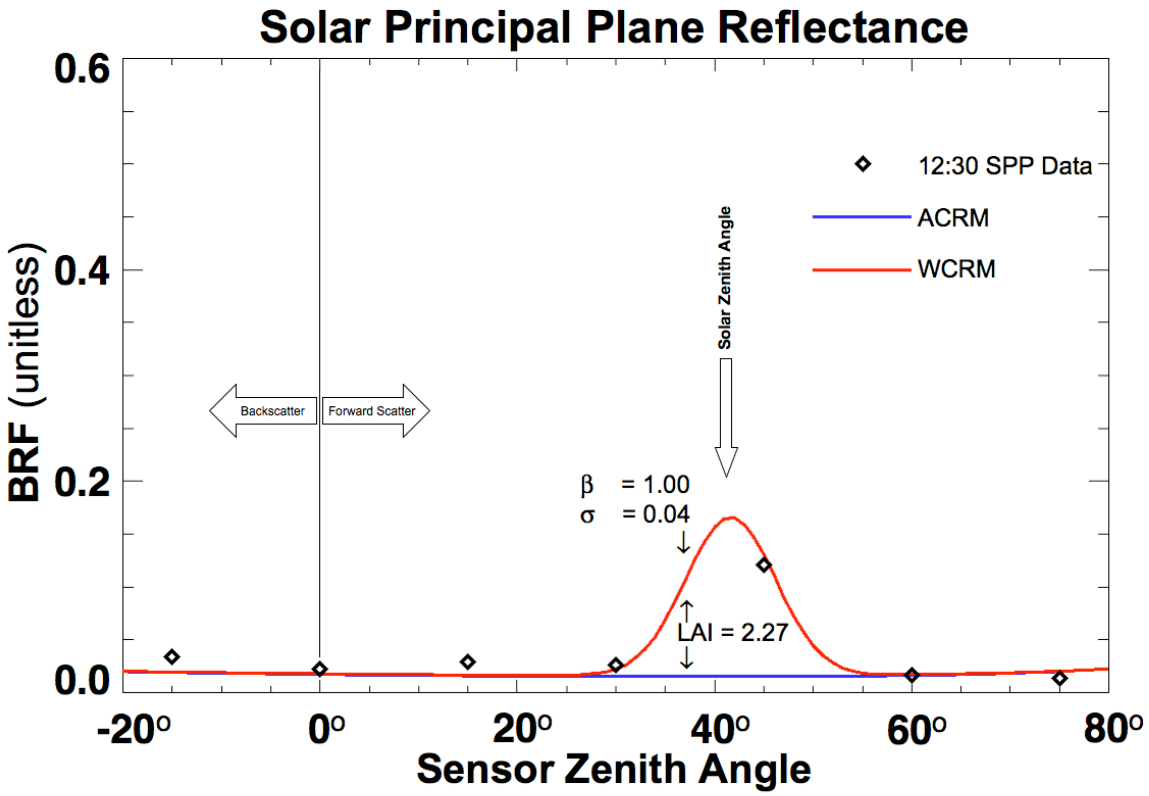

Figure 5-5. A comparison of modeled reflectance from WCRM and ACRM. To better illustrate the difference, σ was chosen to fit the data spike at 45°. However, any nonzero value above the baseline that is less than twice the difference between spike value and the baseline would better fit the data than ACRM. This means that a range of values for σ exist that would reduce model biases.

dominated by the reduction of the glint spikes along the SPP. The RMSE did not show any appreciable difference between modeling cases for the entire data set. This is interpreted to result from the fact that the modeling cases are all very similar at 445.76 nm and only differ for the SPP bias from glint, which was reduced by WCRM.

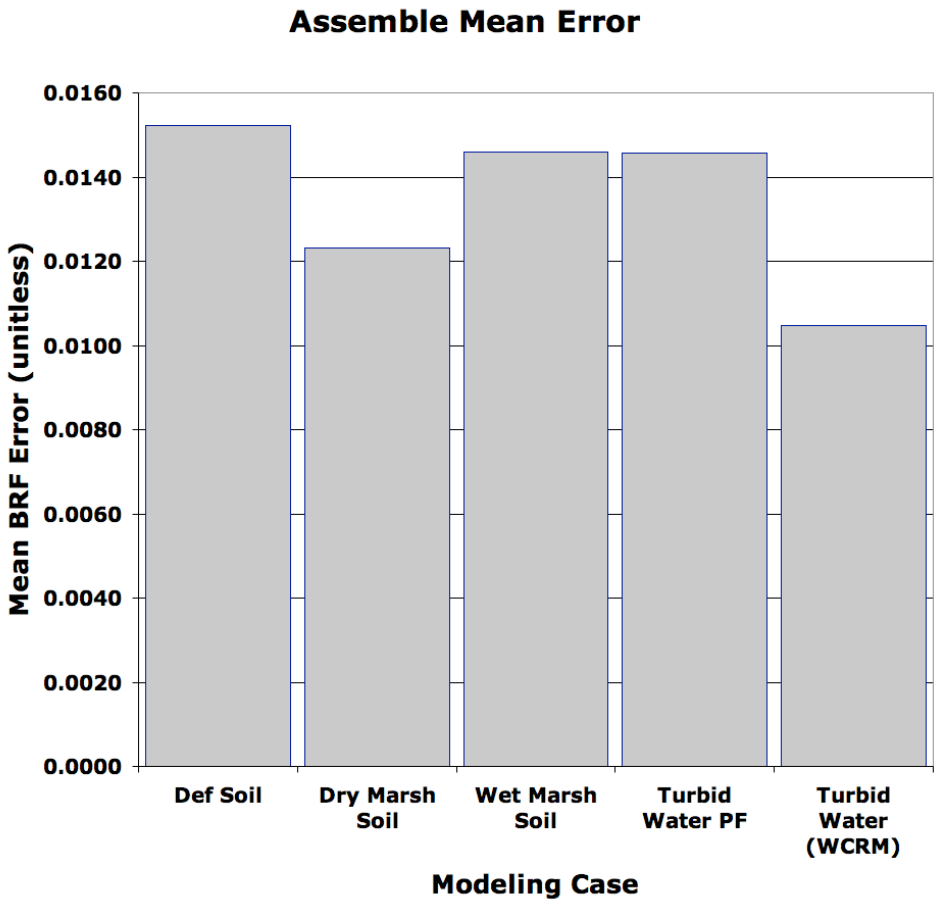

Figure 5-6. The assemble mean error for an average of residual biases for 445.76 nm over all azimuthal planes and all time periods. Despite the larger data set, which includes azimuthal planes with little to no specular reflectance effects, the reduced bias afforded by WCRM is still significant.

Spectral Correlation

Hyperspectral classification is an important analysis tool for studying marsh systems. Tidal salt and high-salinity brackish marshes tend to form monospecific canopies, with certain species favoring salinity conditions that change geographically. As a result, the landscape becomes partitioned into zones of plant species that can deal with different levels of salinity, a processes called *zonation* (Adam, 1990; Day, 1989). Observing changes in zonation can provide information about how a marsh system is responding to changes in hydrologic processes or sea level. Change in distribution can also be caused by invasive species. Hyperspectral classification techniques are commonly applied to map the distribution of marsh species (Adam and Mutanga, 2009;

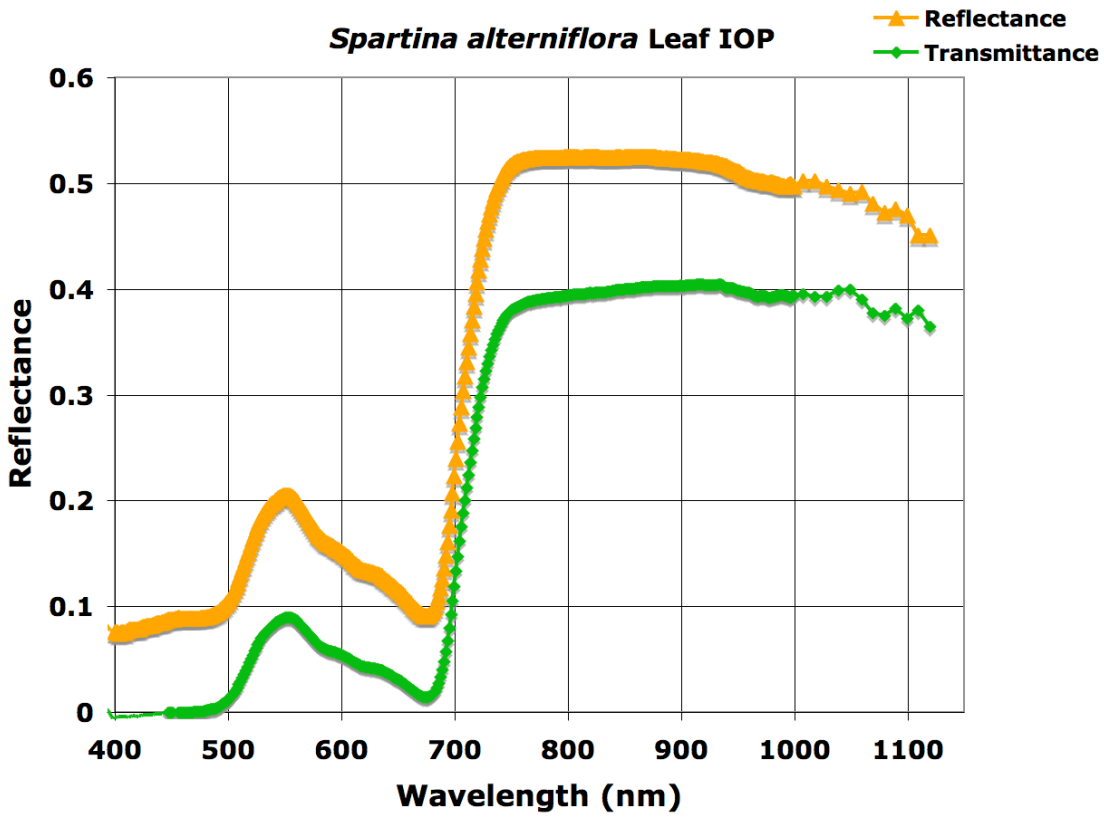

Figure 5-7. USGS Leaf reflectance and trans-mittance data for *Spartina alterniflora* Loisel (Ramsey and Rangoonwala, 2005).

Adam, *et al.*, 2009; Andrew and Ustin, 2008; Artigas and Yang, 2005; Barducci, *et al.*, 2009; Judd, *et al.*, 2007; Zomer, *et al.*, 2009).

However, the canopy reflectance spectrum can be affected by background reflectance. Any influence of the background will depend in part on viewing and illumination angles (Gemmell, 2000). To help understand how viewing and illumination angles affect the vegetation spectrum, the spectra from the SFG data were compared with leaf reflectance for *Spartina alterniflora* (Ramsey and Rangoonwala, 2005). Figure 5-7 shows both the reflectance and transmittance spectra for this species. Pearson's correlation coefficient is used as the metric to determining closeness of the canopy spectrum to the *S. alterniflora* leaf reflectance. The correlation coefficient is, when applied in this manner, also known as the spectral cross-correlation measure (SCM), which is a traditional spectral classification measure for gauging the spectral shape similarity between two spectra. Generally, the SCM is centralized to the spectra's mean. However, if the mean were zero for both spectra considered, then the SCR would equal the cosine of another traditional measure for spectral discrimination called the *spectral angular distance* (van der Meer, 2006). The SCM is defined as,

$$\rho(s_1, s_2) = \frac{Cov(s_1, s_2)}{\sigma_1 \sigma_2} \qquad \text{Eq. 28}$$

where, s_1 and s_2 represent the leaf reflectance spectrum and an instance of the SFG canopy reflectance spectrum (order is not important), and σ_1 and σ_2 are the respective standard deviations of these spectra, taken across wavelength. $\rho(s_1, s_2)$ was computed for each measured spectrum at all the angles taken with the SFG. Figure 5-8 illustrates the distribution of these angles and indicates how they map to the results shown in Figures 5-9 and 5-10. The spectra s_1 and s_2 are considered closer in spectral shape as $\rho(s_1, s_2)$ approaches unity and very different when $\rho(s_1, s_2)$ approaches zero.

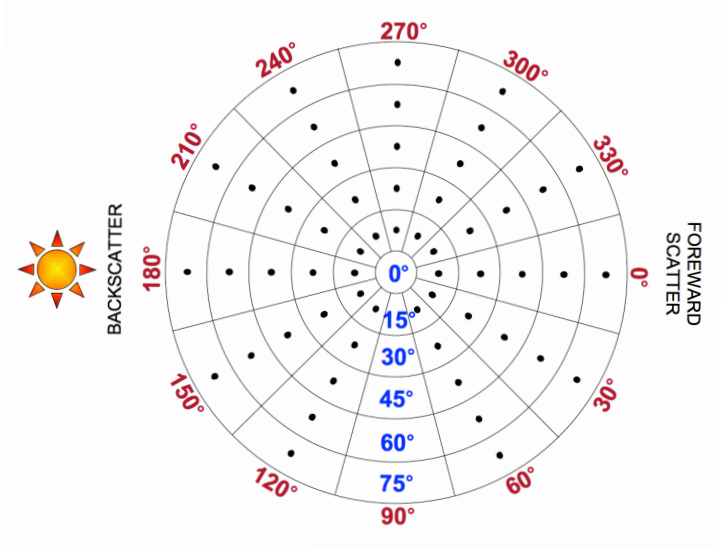

Figure 5-8. Distribution of sensor zenith angles for Schill BRF data. This convention pertains to the plots in Figures 5-9 and 5-10.

It was found that when the common NIR values were included in the correlation calculation, the result was consistently very close to unity. This is not surprising given that the dominant spectral feature from about 400 to 1100 nm is the reflectance plateau beginning just above 700 nm. Except in the case of an extremely sparse canopy, or high water level relative to the overall canopy height, the main effect of water on the background is to decrease the plateau with decreasing above water biomass. As this does not strongly affect the overall shape of the spectrum in the 400 to 1100 nm range (except for the aforementioned cases) water does not strongly affect the ability to distinguish the vegetation canopy from other spectral components. Effects like glint should in principle be spectrally flat, but at the scale of the SFG measurements, it was found that it could affect the visible without any discernible effect to the NIR reflectance. Despite this non-intuitive result, the presence of sun glint appears to have little to no effect on the correlation when the 400 to 1100 nm range is used.

Much more variation was observed across the SFG measurements in 400 to 700 nm range, which is also useful for distinguishing between some marsh species (Artigas and Yang, 2005). Figure 5-9a shows the correlation between the SFG spectrum in the visible and the *S. alterniflora* leaf reflectance. The results show that the backscatter direction is preferable for minimizing the spectral influence of the background. The minimum correlation tends to occur for low sensor zenith angles, which goes lower with

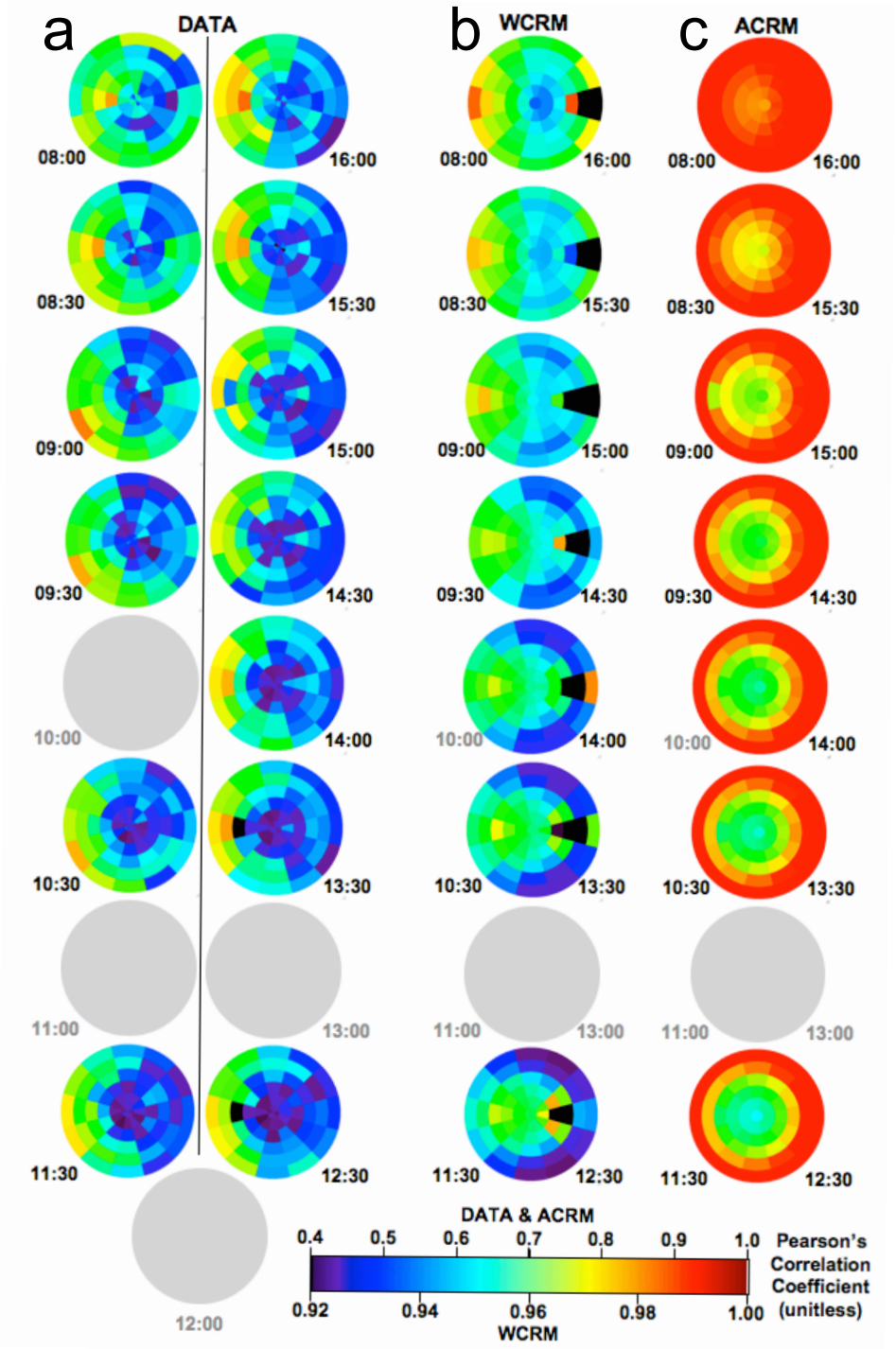

Figure 5-9. Correlation with the *S. alternifora* leaf reflectance spectrum. Each disk gives the correlation coefficent for every sensor zenith and azimuth angle (as defined in Figure 5-8). Disks are shown for 13 periods of the day for a) Schill canopy reflectance spectrum (Schill, *et al.*, 2004), b) WCRM model, and c) ACRM model (the models are symmetrical across solar noon). A sensor azimuth of 0° (and 180°) always pertains to the solar principal plane. Colors scales were applied to highlight angular patterns in correlation. Gray circles indicate that no data were taken at the time period indicated.

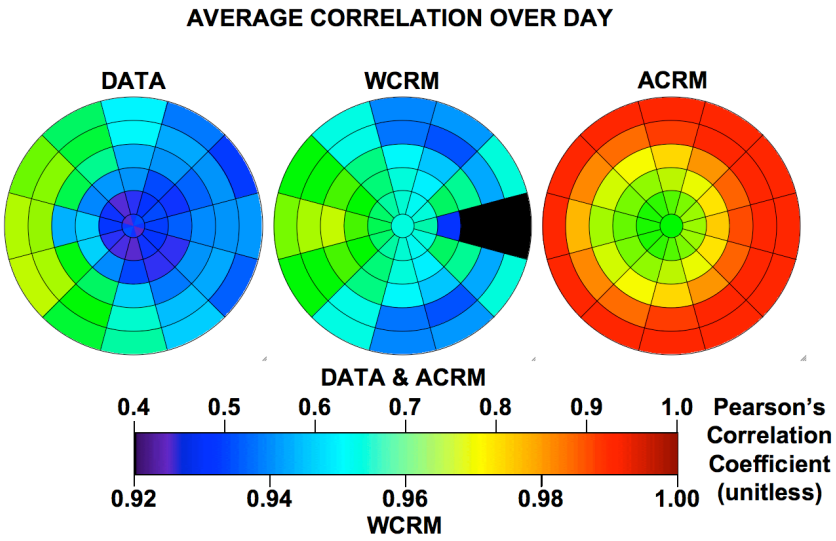

Figure 5-10. Correlations of Figure 5-9, averaged over all time periods. The average provides a more consistent, symmetric pattern to emerge in the data. The model results were averaged for comparison of like statistics.

the decreasing distance from solar noon (i.e., as the sun is closer to zenith). This is likely because the background becomes more illuminated as sunshine more deeply penetrates the canopy at low zenith angles. The data show that the maximum correlation shifts over the day from one side of the solar principal plane to the other. As the physics demand that the reflectance field be symmetrical about the SPP, a possible explanation is that there was systematic error in the positioning of the alignment of the SFG zenith arc and the solar position. Taking the average of the SCM over all measurement times produces a more symmetric distribution as shown in Figure 5-10.

The WCRM and ACRM models were run for each zenith and azimuth angle, and the correlation was computed between the modeled canopy reflectance spectrum and the leaf reflectance spectrum of *S. alteriniflora*. The results for each time period can be seen in Figure 5-9 and the averages are shown in Figure 5-10. A low canopy LAI value of 0.9 was used for both models. The default expert soil was used for ACRM. The water surface roughness, σ, was set to 0.06 and the water coverage fraction, β, was set to unity

for WCRM. The shallow water model parameters were set to the values described in Appendix D. All other parameters were set to their default values.

Both models produced correlation values that were much closer to unity than the data. This is to be expected given that the models are simple representations of the canopy and do not have other contributing spectral signals other than the substrate, whereas the actual canopy also has senescent vegetation, detritus, and other components that could affect the canopy over greater range of directions. For each measurement time, the model correlations are: mirrored across the solar principal plane, symmetric in time to solar, and are generally smoother than the data results. This stems from the simplicity of the underlying assumption of homogeneity in the vegetation media, which is probably more appropriate at larger scales. Conversely, the actual data show more variation than the models, which likely arises as individual plants and canopy gaps move in and out of view as the sensor is repositioned from measurement to measurement.

However, the resulting pattern in the data still can be related to actual behavior of the canopy spectrum across the viewable hemisphere for several solar positions. Both models show that the backscatter direction is better for getting a strong vegetation signal, and that high solar zenith angles are also useful. ACRM more closely agrees with the data that the nadir direction grows worse as the sun becomes closer to zenith, while WCRM only shows this at the highest solar zenith angles. An explanation for this would be that the submerged leaf reflectance, and perhaps in-water chlorophyll content, creates a background that is less distinguishable from the canopy above. Therefore, for the situation modeled by WCRM, the background influence on the canopy produces a stronger chlorophyll peak in the green and thus more closely matches the leaf spectrum. ACRM, conversely, can be influenced more at the top of the canopy by dry soil at green wavelengths. This suggests the substrate of the measured canopy did not include as much submerged vegetation or that the water was more turbid with suspended sediment. Photographs of the experiment during measurements suggest that either could be true.

WCRM also showed a significant drop in correlation in the solar principal plane around the direction of solar specular reflectance. This was not as apparent in the plots of Figures 5-9 or 5-10. Closer examination of the correlation coefficient along the solar principal plane, however, did show that when glint was observable, the correlation dropped substantially. As previously mentioned, local variation in the canopy structure caused much variation in the glint when the solar specular direction was observed (cf. Figure 5-3). Moreover, other natural variations in the measured spectra and noise caused variations in the correlation coefficient that was comparable to variations in the glint. The net effect was of the glint behavior was not remarkably greater than other noise sources across the entire observable hemisphere at the scale of the SFG experiment, but when it was observable, it did cause the a large drop in correlation.

Conclusions

WCRM and four configurations of ACRM were used to fit the SFG canopy reflectance field. Each model case was used to retrieve model input parameters, mainly LAI, and then run to compute the marsh reflectance. The use of WCRM was demonstrated to reduce biases in the residual reflectance field, which likely stem from specular reflectance. The SFG data also provided insight into the importance of specular and spectrum effects of an inundated canopy that suggest areas for future work.

In comparing the ability of various configurations of ACRM and the WCRM model to reproduce the SFG BRF field, WCRM had improved recovery of the observed reflectance along the SPP at 445.76 nm, where specular reflectance artifacts are more evident. Furthermore, over all the SFG azimuthal planes the mean error was smaller for WCRM than the other ACRM cases. As soil and diffuse water reflectances were similar at this wavelength for all modeled cases the resulting profiles with sensor zenith angles were close in agreement (see Figure 3-1). Moreover, the BRF shape was very flat in all cases (cf. Figure 5-5). Therefore, only WCRM was able to provide a prediction for a

spike in the direction of specular reflectance. The presence of a rise in reflectance in this direction reduced the overall error for WCRM in comparison to the modeled cases without specular reflectance. The results for the NIR case did not show any appreciable difference in all cases. For that region of the spectrum, the specular reflectance spikes appeared less prominent or nonexistent, even when spikes were evident at visible wavelengths. This might be attributed to the decimeter scale at which the SFG experiment was done. The number of gaps that are observable can vary with changing view zenith and azimuth angles. When a gap occurs that could allow the observation of glint, a prominent spike can occur in the low reflectance region of the visible spectrum. However, the same gap will cause a decrease in NIR reflectance, which can reduce any corresponding increase from specular reflectance through the same gap. Because the specular reflectance tends to be around the same amount as the NIR reflectance, it is suggested that one can replace the other at this scale.

At the scale at which the SFG data was collected, the effect of glint in the instrument's field-of-view is largely a random process. A glint spike prediction that is less than twice the average baseline-subtracted observation would reduce the RMSE and bias produced by specular reflection. Successive trials showed that the error reduction could be achieved by values of σ greater than about 0.03 with the SFG data.

The results of these comparisons against the SFG data support the hypothesis that the aquatic background model in WCRM affords some improvement in predicting specular effects over the original ACRM model. The analysis also verifies the function of the model, but does not quantify its actual predictive power for retrieval of the canopy BRF along the SPP. To achieve a satisfactory quantification of WCRM's predictive capability would require a comparison to sample data taken on a much large scale, one commensurate with distribution of random processes leading to glint at the remote sensing scales of interest. Such an investigation is outside of the scope of this study, but suggested for future work.

Correlation between the SFG data and the leaf reflectance spectrum of the plant species populating the target canopy indicate that the general backscatter direction is preferable for obtaining the strongest vegetation spectrum in the visible and that this preference increases with decreasing solar zenith angle. This is also true for the combination of the visible and NIR wavelengths, but the effect was much more subtle, as the dominant NIR plateau lends a remarkably strong feature that is easily identifiable from any direction. For the larger wavelength range, the correlation was consistently very close to unity. Both the ACRM and WCRM model produced the same preference for the backscatter direction, especially for azimuth angles closer to the solar principal plane. Both models also predicted stronger correlation near the reflectance hotspot. WCRM predicted a substantial decrease in correlation around the direction of specular reflectance. Neither the hotspot or glint effects could be clearly seen in the plots of Figure 5-9. Variations from these effects was similar in magnitude to other sources of noise in the data. Closer examination of measures where these effects were known to occur verified that they did affect the correlation in a fashion similar to the model predictions. ACRM predicted that correlations near nadir would be reduced by the influence of the background spectrum. A similar pattern arose in the correlation between the SFG data and leaf reflectance.

WCRM, however, did not predict this decrease in correlation around low solar zenith angles. This is probably because the aquatic background spectrum has a strong chlorophyll peak near 550 nm from the presence of submerged vegetation and in-water phytoplankton. This would enhance the aquatic backgrounds correlation with the vegetation in the visible region of the spectrum. However, examinations of photographs of the SFG experiment suggest that the presence of turbid water with a high sediment load, possibly from disturbances in the substrate during the set up or operation of the apparatus. This would produce an aquatic background with a more soil-like spectrum, thus the ACRM correlation better represented the results with the data. In general, a

lower value of β or higher concentration of suspended particular matter (SPM) would probably put WCRM in closer agreement with the data and ACRM. However, this raises an interesting point. The presence of emergent soil or suspended sediment can reduce the canopy's spectral similarity to a vegetation spectrum, so β and SPM are important factors to consider when modeling a marsh canopy. This also further increases the number of unknown variables when measuring the marsh reflectance spectrum. Further work will be needed to determine whether use of the NIR can delineate contributions to the green peak, as submerged chlorophyll reflects very little out of the water in that region of the spectrum.

Chapter 6 The Inundation Experiment and Simulation

Introduction

In 1995, an experiment was performed where the canopy reflectance spectrum was measured for three monospecific canopies, while the water level was artificially increased (Stutzer, 1997). For the present study, data from the inundation experiment were used to demonstrate qualitatively that WCRM can reproduce spectral effects observed with increasing levels of inundation. In addition, information from the shallow water component of the WCRM model, offered explanations for spectral features observed during high water levels.

Implications of nonlinear mixing of water and vegetation spectrum in marsh canopies is discussed. The results of that experiment showed that water causes the NIR region of the marsh vegetation spectra to drop precipitously with increasing water level. As water level increases, the influence of leaf reflectance below the water changes the characteristics of the background aquatic spectrum. In fact, the spectral signature changes to a spectral shape that is not easily explained by spectral mixing (i.e., a linear combination of vegetation and water spectra). The WCRM model helps to explain how these features arise.

Data

Spectral reflectance data were collected with a Spectron Engineering SE-590 spectroradiometer, which was positioned at near solar noon to take a nadir measurements for three different monospecific canopies in the Blackwater Marsh National Wildlife Refuge (NWR) near Cambridge, Maryland USA in May, 1995 (cf. Kearney*, et al.*, 2009). The SE-590 was used to measure the upwelling radiance from the canopy and the downwelling irradiance using a reference panel composed of barium sulfate ($BaSO_4$),

with the usual assumptions of isotropy. The spectrum was sampled from 357 nm to 1124 nm at around 3 nm intervals, but only 214 samples from 399.6 nm to 1032.4 nm were processed (Stutzer, 1997). In each case, the canopy was surrounded on four sides by 1x1 m black felt-covered aluminum panels. The enclosure was then filled by a bilge pump and spectra were recorded at increasing levels of water. Figure 6-1 shows the resulting spectra for an erectrophile canopy of *Spartina patens* with a height of about 40 cm. Measurements were also made for *Spartina cynosurides* and *Schoenoplectus americanus*, with similar results, especially the change in spectral signature when the water level to canopy height was high (cf. Kearney, *et al.*, 2009).

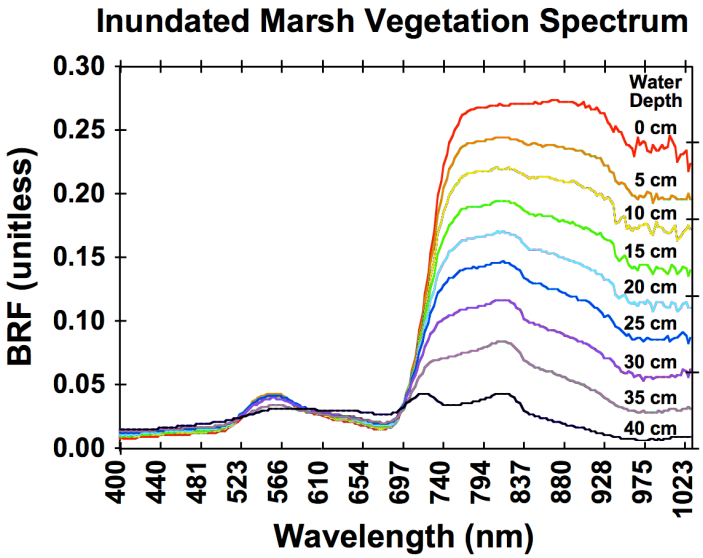

Figure 6-1. Changes in the reflectance spectrum of a canopy of *Spartina patens* as water level increases (Kearney, *et al.*, 2009).

Spectrum Simulation

To simulate the inundation experiment, WCRM was run successively for incrementally decreasing values of above-water LAI. If the distribution of the marsh vegetation canopy can be assumed to be homogeneous in the vertical direction, then above-water LAI can be used as a surrogate variable for the inundation level. Vertical homogeneity was supported by the fact that some marsh vegetation has been shown to have a strong linear correlation with level of inundation (Kearney, *et al.*, 2009), as demonstrated by the fairly even spacing of curves Figure 6-1. The equally spaced LAI values used in the simulation started with a moderately dense canopy with LAI=2.7 and

ended with complete inundation at LAI=0.0. Default values were used for the PROSPECT model, but the resulting leaf optical properties were not expected to be qualitatively different from the field data. The shallow water model values, including Suspended Particulate Matter (SPM), effective depth (H), chlorophyll concentration (C_a), and bottom reflectance ρ_b were set as described in Appendix D. Default values were used for all other input parameters. The results can be seen in Figure 6-2.

Qualitative similarities in the spectra between the simulated results and the observations are evident (cf. Figures 6-2 and 6-1). The peaks that appear near 720 nm and 815 nm were formed by absorption features of the aquatic media and reflectance of the submerged leaves. The former peak was produce with a minimum in the combined absorption of chlorophyll and water, and was characteristic of a productive water column. The latter peak was formed by the edge of a weak water absorption line situated between

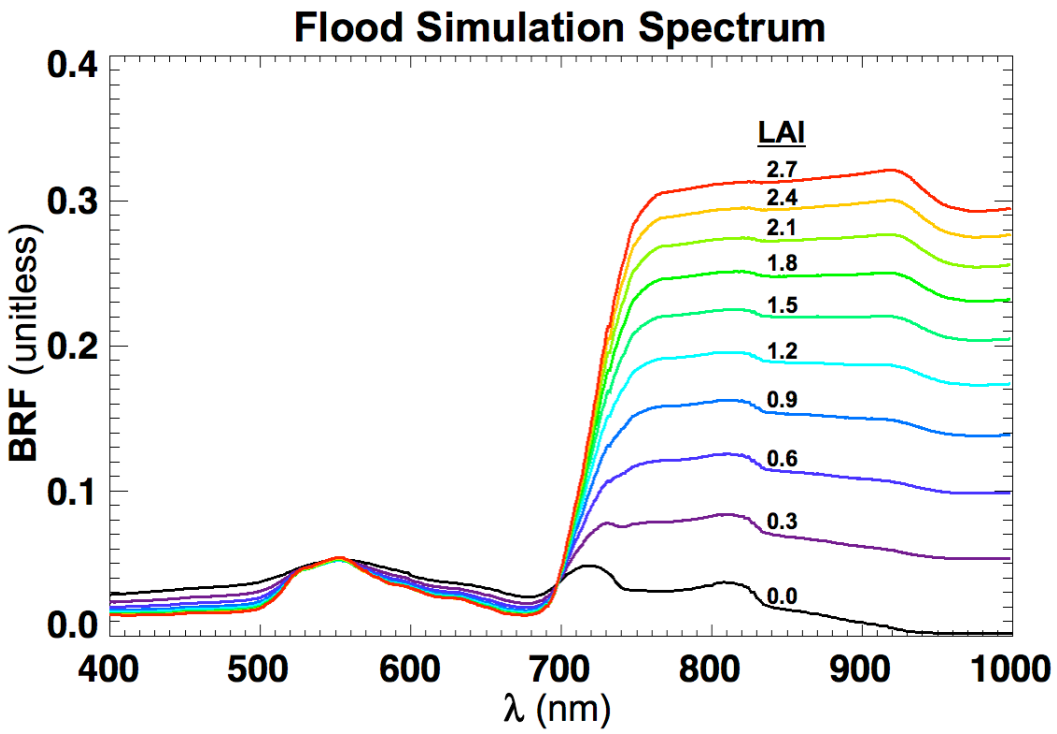

Figure 6-2. Canopy reflectance predicted by WCRM at nadir for ten different water-levels. Following the assumption that the canopy vertical distribution is homogenous, LAI used as a surrogate variable for water-level. The evolving spectral signature resulted in variation of the canopy spectral characteristics.

both peaks (Zhang, *et al.*, 2011). Both peaks were accentuated by the bright reflectance of the vegetation below the water's surface at wavelengths above ~705 nm. At high water-levels relative to the canopy height, the canopy spectral signature would be difficult to form using a simple linear combination of a water spectrum and leaf or canopy spectrum. However, WCRM could be a useful tool in non-linearly discriminating components within canopies where above-water LAI is low.

A shift of about 20nm is observed in the red edge for a dense canopy that goes from zero to complete submergence, as demonstrated with the first order derivative of the simulated spectra in Figure 6-3. This change in the spectral characteristic could be important to studies that make use of the red-edge position, i.e., the wavelengths round the region of 700 to 750 nm at which the maximum increase in vegetation reflectance occurs. The red-edge position was proposed as an indicator of leaf properties by Gates et

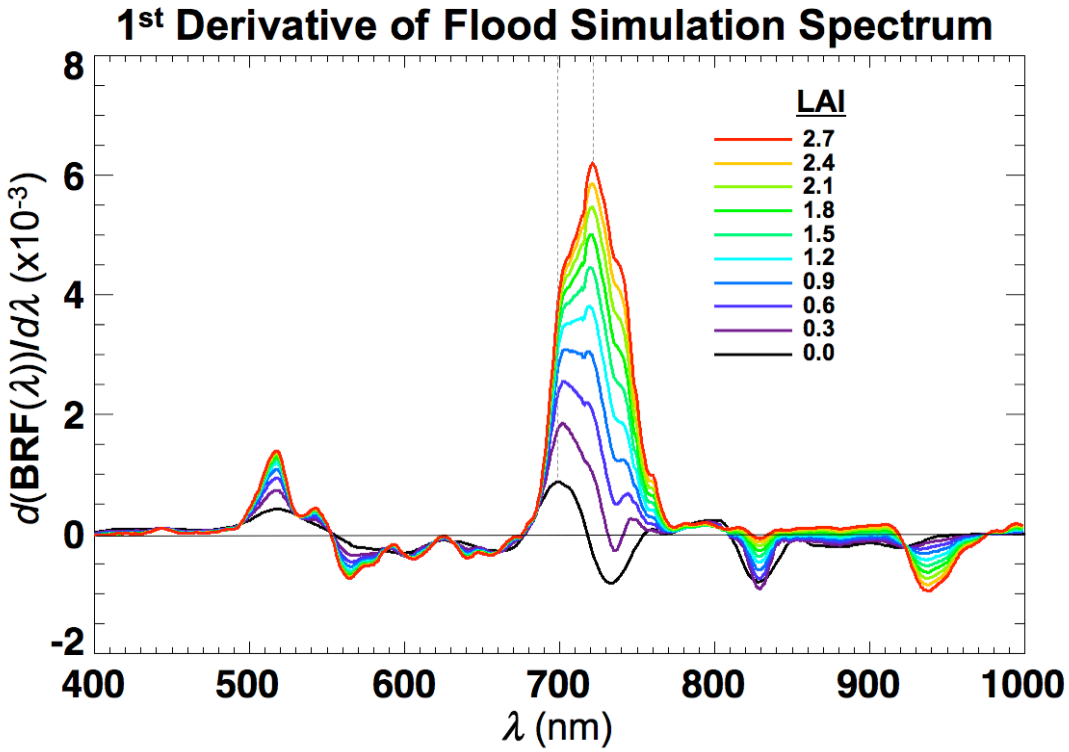

Figure 6-3. First order derivative with respect to wavelength of the simulated inundated canopy spectra show in Figure 3-2. The light gray, dashed lines indicate the peak value, or red-edge position, for the minimum (LAI=2.7 or water level = 0) and maximum water level (LAI=0.0 or water level = canopy height). These two lines are separated by about 22 nm.

al. (1965), such as chlorophyll content (Horler*, et al.*, 1983). The red-edge has since been used to estimate: biomass, LAI (Mutanga and Skidmore, 2007), species discrimination (Adam and Mutanga, 2009), hydric status (Filella and Penuelas, 1994), plant vitality and stress (Boochs*, et al.*, 1990), and effects of heavy metals (Clevers*, et al.*, 2004). The variation of the red-edge position in these studies was usually much less than 40nm (Adam and Mutanga, 2009). Thus the variation in red-edge position observed in the Stutzer experiment and the WCRM inundation simulation covers a substantial portion of the range. Furthermore, the results illustrated in Figure 6-3 demonstrate that a tidal range or flood level that is about two-thirds of the canopy height would cause most of the observed shift in the red-edge position, but it is also possible that smaller tidal ranges or flood levels could still produce significant effects. This suggests for inundated or emergent vegetation, special consideration of water spectral effects is required for studies using the red-edge position. For some situations, WCRM might provide some utility in accounting for these effects, particularly when the in-water optical properties can be estimated *a priori*.

Spectral Differences between Model and Data

The most notable difference between the modeled and measured values was the NIR reflectance. The top curve in Figure 6-1 pertains to an above-water LAI of around 1.3 and has a corresponding reflectance in the NIR of about 0.27. Conversely, the models produce a similar reflectance value for an LAI of about 2.1. This is an anomaly, because typically, both models were found to predict higher LAI reflectance than expected for the given observed LAI value. A possible explanation is that the late Spring canopy of *S. patens* is considerably more reflective in the NIR. This suggests that the model is not always biases high for the marsh conditions and plants in all cases.

Conclusion

WCRM was used to simulate the nadir reflectance spectrum of a marsh canopy as the water level is incrementally increased. The model and data quantitatively agreed, demonstrating the effects of the aquatic background reflectance spectrum and water level on the canopy spectral signature. The spectral signature for both the inundation experiment and the inundation simulation qualitatively agree, especially for low above-water LAI. The field data and model also demonstrated the strong effect that the background reflectance spectrum has on the marsh canopy. According to the discussion in Appendix D, the unique features that come to dominate the canopy with increased inundation can be describe as a result of the interaction between submerged vegetation and the aquatic medium optical properties. The result is a nonlinear combination of spectra (cf. Eq. D-1) depending on the water optical properties and the leaf albedo. The higher frequency variation of the low LAI spectral reflectance signatures with respect to wavelength precludes a simple linear combination of water and leaf endmembers. Further work to establish WCRM utility in separating these optical components is recommended. It was also discovered that as the above-water LAI varies in response to changing water levels. The red-edge position changes significantly and could influence wetland studies dependent on that parameter.

There is a potential to use WCRM to resolve the influence of in-water constituents. However, for general remote sensing applications the water level and in-water optical properties would need to be known. The parameters in the simulation were set to typical values that emphasized similarity to the observed signature. But, conditions could arise where those parameters could differ significantly in value from those used in this study, e.g., high sediment loads. Such changes could alter the weighting of the three peaks seen for mostly submerged vegetation. In extreme cases where sediment is very high and chlorophyll concentration is very low, the resulting background spectrum would be closer to the saturated soil spectrum seen in Figure 3-1. Furthermore, the inundation

experiment and simulation consider the case of submerged vegetation, pertaining to high tidal ranges or flooding. For low water levels or well drained marhes, the substrate bottom can be soil, peat, or a senescent or decaying mat of vegetation material. These substrate component could alter the spectral signature from that used in the simulation, depending on water depth, productivity, and turbidity.

Chapter 7 Synthesis and Future Work

Project summary

Coastal wetlands are of great human and ecological value. Managing and protecting these important resources require careful assessment and monitoring. Remote sensing is a very useful tool to that end as it affords large scale assessments that otherwise would be hampered by the difficulty of transversing these regions. However, the spectral reflectance properties typically measured in remote sensing techniques are influenced by the optical properties of the aquatic background. In order to understand that influence, a canopy reflectance model was modified to account for some of the effects of the presence of water beneath the vegetation canopy. The ACRM model was selected for this study because it has many of the key components used in other canopy reflectance models found in the literature and that code is publicly available with a built-in algorithm that supports the inversion of the model. Both models were used to explore the conditions that were favorable for retrieving LAI. WCRM predictions were compared to aggregated transect data, which showed that the presence of dead standing stock reduces canopy reflectance, forcing the inversion of WCRM to underestimate LAI. Experimental data were used to show that WCRM represented an improvement in predicting LAI and in fitting the reflectance field over ACRM by providing some prediction of specular reflectance. WCRM was also used to simulate the spectral effects of inundation. The results showed that the water and chlorophyll absorption features strongly influence the canopy reflectance spectrum when water levels are high relative to the canopy height.

WCRM Theory and Development

WCRM was created by inserting an aquatic background model as a lower boundary condition of the ACRM vegetation reflectance model. This was done by forming a linear combination with the embedded soil reflectance model, modulated by a fraction of water coverage. In order to include the various radiative flows of the model, the effects of water on the BRDF, the hemispheric reflectances, and the albedo were considered. The aquatic background model included the Cox-Munk model for the specular reflectance of a roughened air-water interface (Cox and Munk, 1956) and a shallow water model (Lee*, et al.*, 1998; 1999) to account for the diffuse spectral reflectance of the water beneath. Because shallow water model includes an assumption of isotropic reflection in this study, the influence of the background on the canopy BRDF anisotropy is largely driven by the calculations related to the air-water interface. However, as the specular reflectance spectrum is essentially flat across the visible and NIR wavelengths, the subsurface shallow water model drives the influence of the canopy reflectance spectrum. The shallow water model also includes the influence of internal reflectance by the air-water interface, but the effect to the BRDF can be seen only at high illumination or sensor zenith angles.

The Theoretical Relationship between LAI and Canopy Reflectance

The WCRM and ACRM models were run to create curves relating LAI to canopy reflectance for four wavelengths, representing blue, green, red, and NIR, and for different sensor zenith angles. The results indicated that there is a poor functional relationship between LAI and canopy reflectance when there is little contrast between the foreground canopy reflectance and the background canopy reflectance. The ACRM runs used a soil spectrum for the background and thus showed more potential for retrieving LAI for visible wavelengths. Blue and red wavelengths have much less multi-scatter within the canopy and thus these wavelengths are preferable for retrieving LAI from models for

most terrestrial landscapes. Conversely, WCRM was run with the dark background of an undisturbed marsh. This demonstrated that the NIR had the best potential for retrieving LAI for such a marsh setting. The visible wavelengths by contrast yielded a very poor theoretical relationship for retrieval of LAI from canopy reflectance.

Field Experiment Results

The data from three field experiments were explored with WCRM. The data provided some further insight into the radiative processes within a marsh canopy and helped to identify strengths and weaknesses in the new model. The transect experiment, WCRM predicted NIR reflectance was compared to reflectance data aggregated along transects at six sensor zenith angles. The BRF experiment showed that WCRM had improved performance over the original ACRM when both were applied to a heavily sampled marsh BRDF, primarily because of the accounting for specular reflection in WCRM. WCRM and ACRM were also compared to the BRF correlation with leaf optical properties to identify optimal viewing directions for minimizing the influence of the background. The inundation experiment and simulation showed that WCRM could qualitatively reproduce spectral features observed for an inundated canopy.

Challenges and Future Work

Several challenges to modeling marsh canopy reflectance were identified throughout this project, many of which were mentioned in previous chapters. Four topics in particular seem worth mentioning here:

1. Parameters with Specular Reflectance Effects - The uncertainty in specular reflectance stemming from lack of knowledge about surface roughness and water cover may undermine the ability to accurately predict marsh BRDF in the specular direction or use the specular reflectance to estimate canopy parameters, such as LAI.

2. Parameters with Spectral Reflectance Effects - The input parameters required by the aquatic background model can be used to model the background reflectance spectrum when known *a priori*, but may be difficult to determine the best values for remote sensing applications when the values for these parameters are not known.

3. NIR Contrast Assumption - Occasional dominance of the background reflectance in the NIR by high SPM or a highly reflective bottom could undermine the use of WCRM when using that region of the spectrum to retrieve LAI because of a reduction in contrast between the foreground canopy and background substrate.

4. Dead Vegetation and Detritus - The tendency of many marsh species to retain standing dead stock or their canopies to have large amounts of detritus reduces reflectance in the NIR, causing retrievals of LAI to be underestimated.

These issues are discussed in detail in the previous chapters. In this section, further issues regarding the model applications at remote sensing and landscape scales is discussed. Following that, the topic of specular reflectance is further considered, followed by challenges in retrieval of model input parameters using marsh canopy reflectance. Finally, potential spectral applications of WCRM are then discussed where *a priori* knowledge of input parameters is available.

During this study, considerable experience was also gained regarding marsh field work, especially including taking measurements in support of remote sensing and reflectance modeling. The lack of an established protocol for this type of work was apparent. Future work toward standardizing related marsh measurement methods, and

wetlands in general, would benefit the portion of the remote sensing community supporting studies of wetlands. Some discussion of challenges in this area is given in Appendix F.

Scaling Up to Remote Sensing Images

A major consideration for future work is adapting the model to scales that are commensurate with aerial and remote sensing imagery, which would provide an opportunity for assessments that cover large regions or perhaps even the globe. To achieve that end, application of the WCRM model, or any marsh canopy reflectance model, to remote sensing imagery will need to account for proximity of small bodies of open water and soil. Variation in the spatial distribution amongst these different cover types and within the marsh vegetation canopy are common. When the horizontal size of openings in the vegetation canopy is much greater than the canopy height (but smaller than the area sampled by the instrument's field-of-view and for relatively moderate zenith angles), the spectral BRDF should be a linear combination of the marsh canopy reflectance spectrum and the reflectance spectrum of the adjoining cover type. In this case, the WCRM model could be used to model the marsh canopy BRDF, e.g., to generate canopy reflectance components for varying levels of inundation or density and varying levels of glint. However, this is not universally true. At probably any spatial resolution, the edges of the vegetation canopy can appear fractal, covering greater number of pixels in a remote sensing image than more linear features. Ponding may present a similar problem over a large range of scales for some marshes. Therefore, the first step would be to determine the frequency of occurrence for nonlinear mixing between inundated vegetation and other cover types, especially open water. Finally, it was also noted that open water, in the form of channels and ponds, can have sufficient fetch length, or exposure, to be strongly affected by wind. Therefore, the dynamic roughening of these surfaces by wind could play a larger role in remote sensing of

marshes. The relationship between wind and surface roughness for these small bodies of water is unknown and will also require further research.

Specular Reflectance of Marsh Aquatic Surfaces

One of the greatest challenges for modeling the marsh BRDF near the specular direction is the overall lack of knowledge regarding surface roughness. Field observations suggests that the water surface roughness under the vegetation canopy may be constrained to a limited range, as also observed by Vanderbilt et al (2002), but many dynamic and static processes are at work. A nominal value may be sufficient in some applications of WCRM, but it may be useful to measure the surface roughness for the air-water interface in marshes under a variety of conditions.

Establishing a range of possible values for surface roughness might involve field studies where glint patterns are recorded (e.g., photographically) and statistics are used to determine the distribution of surface facets, similar to the work of Cox and Munk (1956) and others (Kay*, et al.*, 2009). Given the a possible spread of the solar source in the blue from atmospheric scattering, a red wavelength would probably be optimal for studying surface roughness, but ideally in a setting where soil reflectance is low (e.g., soils with high organic content). However, there are problems with this approach. First, it could be difficult to capture the glint pattern as one moves off the specular direction because the signal would be rapidly attenuated by dense vegetation. The vegetation canopy model would be needed to correct for this attenuation, but this would require good *a priori* knowledge of canopy structure and optical properties.

The same methodology might work for interstitial channels and ponds. Similar to the open water case that Cox and Munk studied, wind is likely to be the dominate influence of the surface roughness of these bodies. However, very little is known about the wind field along such surfaces, especially in the presence of emergent vegetation. Furthermore, obtaining wind fields at spatial resolutions useful for studying marshes

would be very difficult. Thus, even if an empirical relationship could be established between wind and surface roughness of ponds and channels, without *a priori* knowledge of the wind field at the scale of remote sensing pixels, that relationship could not be used to determine the surface roughness when processing satellite remote sensing imagery. This might strongly affect using the model to account for sun glint in remote sensing applications when the instrument is pointed near the specular direction.

When pointed in the specular direction, an instrument with field-of-view that is more than a few degrees across might be less sensitive to variation in the overall glint strength due to surface roughness. An example might be using a Gershun tube probe a short distance above the canopy. In such cases, a nominal surface roughness parameter should be sufficient. This is because the instrument would smear out the narrow specular beam when the surface is exceptionally flat, as if the beam were coming from a rougher surface. If this blurring of specular reflectance is larger than the maximum dispersion likely to seen in the sub-canopy water surface, then knowledge of the surface roughness is irrelevant. The strong, penetrating signal of the light from the surface then serves as a useful probe for vegetation structure as was demonstrated by Vanderbilt et al. (2002). WCRM might offer an opportunity to combine the attenuation of specular reflectance with the effects of diffuse radiative flow to obtain a good estimate of LAI, even in fairly dense canopies using probes over the canopy. However, at this stage the diffuse radiative flow will require further study before being considered for such an application.

There also appears to be a difference between the prominence of sun glint spike in the visible and NIR wavelengths. The glint spectrum is expected to be relatively flat over all measured wavelengths. Many times in the SFG data, when a spike in reflectances was observed at visible wavelengths, no corresponding increase could be seen in the NIR for the same measurement. It is expected that spikes in reflectance would be more prominent at visible wavelengths because the surrounding vegetation reflectance is relatively low, while the same glint would be relatively smaller in the NIR when compared to the strong

canopy reflectance in that region of the spectrum. However, in many cases of the SFG data, specular reflectance spikes were entirely missing at NIR wavelengths even though they were clearly detected at visible wavelengths.

It is possible that atmospheric scatter could be causing the sky near the sun to be much brighter in the blue than the NIR, effectively expanding the illumination source beyond the solar disk at blue wavelengths, thus increasing the likelihood that a facet of the water's surface will produce a highlight in the sensor's field-of-view. If so, the original sky model inherited from ACRM may need to be improved to better account for spectral variation in the distribution of direct and diffuse sky light. However, whether this is a significant contribution to the discrepancy should be verified by experiment in future work.

A more plausible explanation for this discrepancy is related to the scale of the measurements taken by the SFG. At nadir, the sensor projected field-of-view is a circle 10 cm in diameter at the top of the canopy, which is near the same scale as the plants. Furthermore, as the SFG moves the spectrometer across the zenith arc, very different portions of the canopy and background move into the sensor's field-of-view. In the specular direction, if there is a gap between all the plants in the field-of-view then there is a chance that the sensor will detect sun glint. In the visible region of the spectrum, the specular reflectance yields a strong response by the instrument in comparison to measurements at any other angle, producing a relative spike in reflectance. In the NIR region, the same gap produces a reduction in overall reflectance. Any specular flux that makes it through that gap will offset or exceed that loss, but ultimately will produce a spike that can be significantly less prominent to the spike seen in the visible. This scale effect can be addressed in future studies tied to remote sensing scale through the aggregation of data taken over greater areas. This was, in part, the objective of the transect experiment. However, that experiment did not sample at a sufficient angular

resolution along the solar principal plane nor had a large enough spatial scale to explore glint effects at remote sensing scales.

Future Work in Spectral Applications

WCRM could be applied to applications based on vegetation canopy reflectance spectrum. As noted in this study, WCRM could provided useful information about the canopy reflectance spectrum when much of the vegetation material is below the water's surface. This includes determining how the vegetation and water spectra are non-linearly mixed and also how the red edge is affected by the presence of biologically productive water. WCRM could also be used in a future study to better understand the effects the of an aquatic background on various indices that are based on the reflectance spectrum, such as the Normalized Difference Vegetation Index (NDVI). It is known from experiment that NDVI can be influenced by the aquatic background (Kearney*, et al.*, 2009; Stutzer, 1997) and is also affected in particular by spectral variations in the BRDF (Gao, 2002). It would be useful to further study how the aquatic background affects these indices as a function of canopy water properties and viewing/illumination geometry. Finally, WCRM could also be used to build a collection of glinted marsh spectra for application in techniques that require an expansive and detailed spectral library. For instance, the Multiple Endmember Spectral Mixture Analysis (MESMA) technique has been applied to species classification for marshes using data from the Airborne Visible and Infrared Imaging Spectrometer (AVIRIS) (Li*, et al.*, 2005; Rosso*, et al.*, 2005). This technique was extended to include glint endmembers to successfully separate the specular contribution to the canopy reflectance when data were influence by specular reflectance (Roberts, 2011). WCRM could be run for a variety of geometries and vegetation densities to augment the spectral library, from which endmembers could be keyed by illumination and viewing directions. WCRM also could provide spectra for a variety of

conditions of the background, varying amounts of submerged vegetation, bottom reflectance, SPM, CDOM, and algal concentration.

Model Remote Sensing Retrievals

Retrieval of LAI using the inverse of WCRM requires using nominal values and ranges for all other input values. It is helpful that WCRM and ACRM were found to be considerably more sensitive to LAI then any other input parameter. Conversely, the inverse of ACRM or WCRM is not as strong of a predictor of other vegetation canopy parameters, and because of the model's stronger response to LAI, that parameter may need to be fixed *a priori.* This situation could possibly pose a challenge for the remote sensing of model parameters other than LAI using either ACRM or WCRM for a marsh target. Moreover, the several additional parameters that were added to support the aquatic background model would likewise be difficult to retrieve. Given the typically darker signal of the aquatic background, it would be especially difficult to retrieve values for background parameters (e.g., concentrations of chlorophyll, CDOM, or SPM).

Suspended soil and variation in bottom reflectance can also strongly affect the reflectance at NIR wavelengths. The presence of reflective bottoms (e.g., sand) or high turbid water with high sediment load, would reduce the useful contrast between vegetation and background at NIR wavelengths, which would reduce the accuracy of an LAI retrieval (Gobron, 1997). In addition, for well drained marshes, soil tends to be saturated and less submerged. Therefore the fraction of water coverage, β, could play a stronger role than the more flooded marshes studied in project. Future studies need to expand the number of cases where WCRM could be applied, including well drained marshes with emergent soil and situations when suspended soil concentration are high.

Conclusions

The nature of remote sensing applications is to relate radiometric measurements to actual surface conditions. A model, such as WCRM, uses *a priori* knowledge of the radiative transfer processes within the marsh canopy to describe that relationship. WCRM, a first of its kind, will continue to improve understanding of how the aquatic background affects marsh radiometric measurements. However, currently the nascent model still needs refinement, as prior sections outlined. Each of these steps will move closer to better model applications, whether related to measurements using a sensor on the ground or using an airborne or spaceborne imager. In addition, development of a first-principle model can, and in this case has, yielded several results that provide better understanding of the processes underlying marsh canopy reflectance.

First, it was demonstrated that WCRM is an improvement over the original vegetation canopy reflectance model in predicting the effects of specular reflectance. In addition, with better information about wetland water surface roughness, the model could be used to predict directions to avoid forward scatter directions. Conversely, if further understanding of marsh water surface roughness is obtained and found predictable, then specular reflectance could possibly be used to probe marsh structure.

Second, in a parallel effort to validate one aspect of model performance, a new method was demonstrated where Sandmeier Field Goniometer spectral data was cross-correlated with a leaf spectrum to chose optimal directions for evaluating the spectral characteristics of canopy vegetation. This approach could yield information such as species or functional type, offer information about marsh microtopography and composition, or provide insight regarding canopy plant stress. This information could also be used to devise a protocol for making spectral reflectance measurements of marsh canopies. Similarly, this information could be used for developing and planning passive remotes sensing imaging of wetlands or inundated vegetation.

Furthermore, using the cross-correlation metric for a *Spartina alterniflora* canopy, it was also learned that the backscatter direction was optimal for retrieving hyperspectral characteristics in the visible. Cross-correlation with a leaf spectrum increased with zenith viewing angle, suggesting that the optimal zenith viewing angle for any remote sensing application would be limited by 1) the instrument field of view and for the case of imager applications, and by 2) decreasing atmospheric correction accuracy with increasing zenith angle.

However, SFG measurements are complicated and costly. Modeling the cross-correlation would provide a less expensive, easier way to predict optimal measurement directions and hence may be able to cover a greater variety of cases. In comparing model predicted cross-correlations to those calculated with the data, the WCRM showed improved prediction of these optimal directions over the original vegetation canopy model. This result suggests that WCRM is an improvement towards developing a prediction of optimal view and illumination geometry.

The model was also used to explain the nonlinear influence of the aquatic background on the canopy reflectance spectrum. First, WCRM could qualitatively simulate spectral effects of inundation. The unique spectral signature of heavily inundated vegetation could be explained simply using the first principles embedded within the shallow water component of WCRM. Further simulation also demonstrated a nonlinear 20 nm shift in canopy red-edge as water went from minimum to maximum level, which is a revelation that could affect a number of techniques currently being explored by researchers.

The influence of aquatic and terrestrial backgrounds on LAI retrieval, were also explored using model sensitivity analysis. That analysis showed that the inversion of a marsh canopy model would best retrieve marsh LAI using NIR wavelengths because the dark background would promote the greatest contrast with the foreground vegetation. Conversely, this spectral region is particularly poor for the terrestrial case as dry soils

tend to be much lighter at such wavelengths. However, to pursue LAI retrievals for marshes, the canopy multi-scatter must be more accurately predicted and the vegetation canopy model must also better account for the complicated matrix of spectral components found in a marsh canopy (e.g., dark, senescent and dead vegetation).

Appendices

Appendix A - Geometric Conventions for Specular Component

In deriving the specular reflectance model, a small area the air-water is divided into smaller, tilted surface facets (see Figure A-1). A ray of light that is incident on each facet forms the angle, ω, to the direction that is normal to the facet. By the law of reflectance, the light reflected from the facet forms the same angle ω with the facet normal, but propagates in the direction mirrored across the surface normal on the *plane of incidence*, which is defined by the normal and incident directions (see Figure A-2). These three directions are represented with the unit vectors $\vec{\xi}_n$, $\vec{\xi}_i$, and $\vec{\xi}_r$, which correspond respectively for the normal direction and the directions of the light source and the reflected light, represented by unit vectors. These vectors can be defined either in Cartesian coordinates or spherical coordinates, the latter being more convenient. Spherical coordinates for each unit vector is given by a zenith angle, θ, (angle between the vector and the z-axis) and an azimuth angle, ϕ, which is measured between a projection of the vector on the x-y plane and the x-axis. These two coordinate systems can be related as follows:

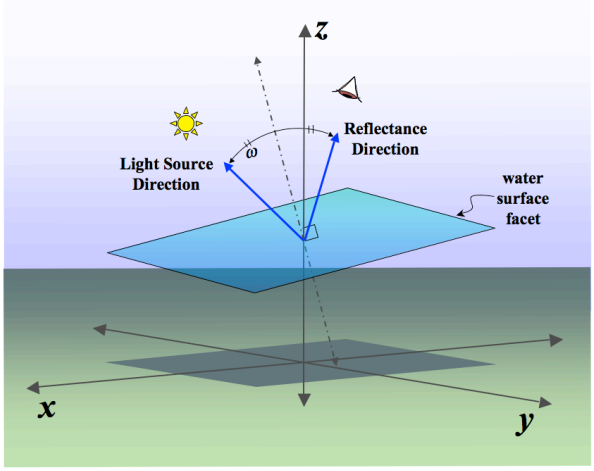

Figure A-1. The surface of the water is modeled by dividing it into small tilted facets. A ray of light incident on a facet is reflected in a unique direction determined by the direction of the light source and the direction normal to the facet.

$$\vec{\xi}_i = \begin{bmatrix} \sin\theta_i \cos\phi_i \\ \sin\theta_i \sin\phi_i \\ \cos\theta_i \end{bmatrix} \quad \text{Eq. A-1}$$

$$\vec{\xi}_r = \begin{bmatrix} \sin\theta_r \cos\phi_r \\ \sin\theta_r \sin\phi_r \\ \cos\theta_r \end{bmatrix} \quad \text{Eq. A-2}$$

$$\vec{\xi}_n = \begin{bmatrix} \sin\theta_n \cos\phi_n \\ \sin\theta_n \sin\phi_n \\ \cos\theta_n \end{bmatrix} = \frac{1}{2\cos\omega} \begin{bmatrix} \sin\theta_i \cos\phi_i + \sin\theta_r \cos\phi_r \\ \sin\theta_i \sin\phi_i + \sin\theta_r \sin\phi_r \\ \cos\theta_i + \cos\theta_r \end{bmatrix} \quad \text{Eq. A-3}$$

where θ_n, θ_i, and θ_r are the zenith angles and ϕ_n, ϕ_i, and ϕ_r are the azimuth angles of unit vectors $\vec{\xi}_n$, $\vec{\xi}_i$, and $\vec{\xi}_r$, respectively. Figure A-2 illustrates the geometric convention being used for these vectors and their corresponding directional angles. For convenience, $\vec{\xi}_r$ will also be used for the direction of observation.

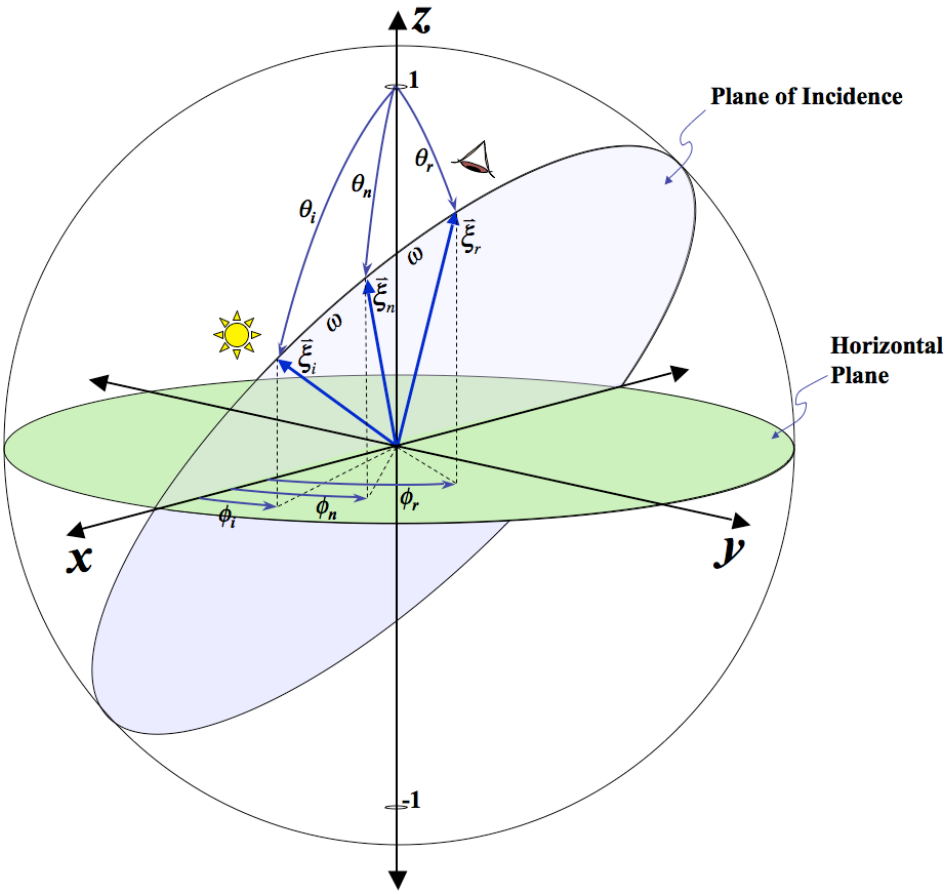

Figure A-2. Illustration showing the geometric convention used for the unit vectors and their zenith and azimuth angles.

Appendix B - Calculation of Fresnel Reflectance

The reflectivity (and transmissivity) of each facet of the air-water interface is governed by Fresnel equations, which can be simplified to give reflectance for light at wavelength λ incident on a single facet,

$$r_f(\omega,\lambda) = \frac{r_s(\omega,\lambda) + r_p(\omega,\lambda)}{2} \qquad \text{Eq. B.1}$$

where, $r_s(\omega,\lambda)$ and $r_p(\omega,\lambda)$ indicate the reflectance of light polarized such that the E-vector is perpendicular and parallel to the plane of incidence, respectively. These quantities are in turn given by

$$r_s(\omega,\lambda) = \left[\frac{\sin(\omega - \omega_t(\lambda))}{\sin(\omega + \omega_t(\lambda))}\right]^2 \qquad \text{Eq. B.2}$$

and

$$r_p(\omega,\lambda) = \left[\frac{\tan(\omega - \omega_t(\lambda))}{\tan(\omega + \omega_t(\lambda))}\right]^2 \qquad \text{Eq. B.3}$$

where $\omega_t(\lambda) = \sin^{-1}(n_r(\lambda)\sin\omega)$ is the angle of the light transmitted below the surface of the facet and its normal. $n_r(\lambda)$ is the ratio of the index of refraction of air to that of water, $n_a(\lambda)/n_w(\lambda)$,

$$n_r(\lambda) = \frac{n_a(\lambda)}{n_w(\lambda)} \cong \frac{1}{n_w} \qquad \text{Eq. B.4}$$

which is approximately 0.75 for most of the visible to near infrared wavelengths. In this study, the incident light is assumed to be unpolarized for simplicity and Fresnel

reflectance (and transmittance) will be calculated only as the average reflected light given by Equation B.1.

Appendix C - Cox-Munk Slope Density Function: Change of Variables

As described in Chapter 2, the differential radiance value attributed to facets reflecting towards the observer from some source is

$$dL_{r,s} = L_i \frac{\cos\omega}{\cos\theta_n \cos\theta_r} r_f(\omega) \cdot p_{\mathbb{R}^2}(z_x, z_y) \cdot dz_x dz_y \qquad \text{Eq. C-1}$$

where, L_i is the radiance of the source. For simplicity, the dependence on wavelength λ is omitted in this equation.

To calculate dL_r as function of illumination and observation directions, z_x and z_y must be determined as functions of $\vec{\xi}_i$ or $\vec{\xi}_r$,

$$z_x(\theta_i, \phi_i, \theta_r, \phi_r) = \frac{-(\sin\theta_i \cos\phi_i + \sin\theta_r \cos\phi_r)}{\cos\theta_i + \cos\theta_r} \qquad \text{Eq. C-2}$$

$$z_y(\theta_i, \phi_i, \theta_r, \phi_r) = \frac{-(\sin\theta_i \sin\phi_i + \sin\theta_r \sin\phi_r)}{\cos\theta_i + \cos\theta_r} \qquad \text{Eq. C-3}$$

which puts the probability density function in terms of angles associated with these directions, for which the notation $p_\Omega(\theta_i, \phi_i, \theta_r, \phi_r) = p_{\mathbb{R}^2}\left(z_x(\theta_i, \phi_i, \theta_r, \phi_r), z_y(\theta_i, \phi_i, \theta_r, \phi_r)\right)$ is used, where Ω denotes the probability density function mapped to the unit sphere. Now, the probability that a ray of light passes from the source into the direction of observation can be defined as

$$P\left\{|\theta - \theta_r| < d\theta_r \wedge |\phi - \phi_r| < d\phi_r\right\} \cong p_\Omega(\theta_i, \phi_i, \theta_r, \phi_r) \cdot |\mathbf{J}| \cdot d\theta_r d\phi_r. \qquad \text{Eq. C-4}$$

where the Jacobian matrix, **J**, is used to change the independent variables of the probability density function $p_{\mathbb{R}^2}(z_x, z_y)$. The Jacobian matrix is defined as

$$|\mathbf{J}| = \begin{vmatrix} \frac{\partial z_x}{\partial \theta_r} & \frac{\partial z_x}{\partial \phi_r} \\ \frac{\partial z_y}{\partial \theta_r} & \frac{\partial z_y}{\partial \phi_r} \end{vmatrix} \qquad \text{Eq. C-5}$$

so that for transferring from slope space to coordinates on the unit sphere the determinant becomes,

$$|\mathbf{J}| = \frac{\sin\theta_r \left[1 + \sin\theta_i \sin\theta_r \cos\left(\phi_i - \phi_r\right) + \cos\theta_r \cos\theta_i\right]}{\left(\cos\theta_r + \cos\theta_i\right)^3} \qquad \text{Eq. C-6}$$

This can be further reduced to more a more compact form using only three angles, so that

$$|\mathbf{J}| = \frac{\sin\theta_r}{4\cos\omega\cos^3\theta_n} \qquad \text{Eq. C-7}$$

because

$$\cos\omega = \sqrt{\frac{1 + \sin\theta_i \sin\theta_r \cos\left(\phi_i - \phi_i\right) + \cos\theta_i \cos\theta_r}{2}} \qquad \text{Eq. C-8}$$

and

$$\cos\theta_n = \frac{\cos\theta_i + \cos\theta_r}{2\cos\omega} \qquad \text{Eq. C-9}$$

Substituting the transformed probability density function and Equations C-7 through C-9 into Equation C-1, the small reflected radiance becomes,

$$dL_{r,s} = \frac{L_i}{4\cos^4\theta_n \cos\theta_r} \cdot r_f(\omega) \cdot p_\Omega\left(\theta_i, \phi_i, \theta_r, \phi_r\right) \cdot d\Omega_r \qquad \text{Eq. C-10}$$

Appendix D - Shallow Water Reflectance Model

The shallow water reflectance model by Lee et al. (1998; 1999) was described by Volpe et al. (2011) as,

$$r_d = r_{rs}^{dp}\left[1 - e^{-\left(K_d + K_u^C\right)H}\right] + \frac{\rho_b}{\pi} e^{-\left(K_d + K_u^B\right)H} \qquad \text{Eq. D-1}$$

where,

H = water depth (m);
ρ_b = bottom albedo (assuming bottom as an isotropic reflector);
r_{rs}^{dp} = subsurface remote sensing reflectance for an infinitely deep water column (sr-1) = $(0.084 + 0.17u)\,u$;
u = $b_b / (a + b_b)$, with b_b being the backscattering coefficient (m^{-1}) and a being the absorption coefficient (m^{-1});
K_d = $D_d\alpha$ = downwelling diffusive attenuation coefficient;
K_u^C = $D_u^C\alpha$ = upwelling diffusive attenuation coefficient due to the water column;
K_u^B = $D_u^B\alpha$ = upwelling diffusive attenuation coefficient due to the bottom reflectance;
α = $a + b_b$;
D_d = $1/\cos\theta_w$ = subsurface solar zenith angle (rad);
D_u^C = $1.03\ (1 + 2.4u)^{0.5}$
D_u^B = $1.04\ (1 + 5.4u)^{0.5}$

The absorption and backscatter coefficients are taken as total absorption and backscatter coefficients for water and various in-water constituents, respectively. For absorption,

$$a = a_w + a_{\mathrm{NAP}} + a_{ph} + a_{\mathrm{CDOM}} \qquad \text{Eq. D-2}$$

a_w is the absorption due to water, as measured by Buiteveld et al. (1994) from 300 to 800nm and Kou et al. (1993) for values above 800nm. The non-algal particle absorption, a_{NAP}, is calculated according to Volpe et al. (2011) as

$$a_{\mathrm{NAP}} = a_{\mathrm{NAP},443\mathrm{nm}} 0.75 e^{-0.0128(\lambda - 443)} \qquad \text{Eq. D-3}$$

where $a_{\mathrm{NAP},443\mathrm{nm}} = \gamma \cdot \mathrm{SPM}$, γ = 0.041 m^2/g, and SPM is the suspended particulate matter. The phytoplankton absorption, a_{ph}, is derived from Lee et al. (1999) to be

$$a_{ph} = 0.06\left[C_a\right]^{0.65} \cdot a^*_{ph,440} \qquad \text{Eq. D-4}$$

where C_a is the concentration of chlorophyll *a* pigment in mg m^{-3} and $a^*_{ph,440}$ is the phytoplankton specific absorption normalized at 440nm (Bricaud*, et al.*, 1995). The absorption due to the presence of chromophoric dissolved organic matter (CDOM) is given by a_{CDOM} and estimated as

$$a_{\mathrm{CDOM}} = a_{\mathrm{CDOM},375} \cdot e^{-0.0192(\lambda - 375)} \qquad \text{Eq. D-5}$$

where $a_{\mathrm{CDOM},375}$ is the CDOM absorption at 375nm and is generally taken to be 0.125 m^{-1} (Volpe*, et al.*, 2011). Figure D-1 illustrates the absorption spectra for these components.

The backscatter coefficient, b_b, is the fraction of the total scattering coefficient, b, corresponding to light that is scattered at angles greater than 90°. b is computed from a sum of water and in-water constituents,

$$b = b_w + b_p \qquad \text{Eq. D-6}$$

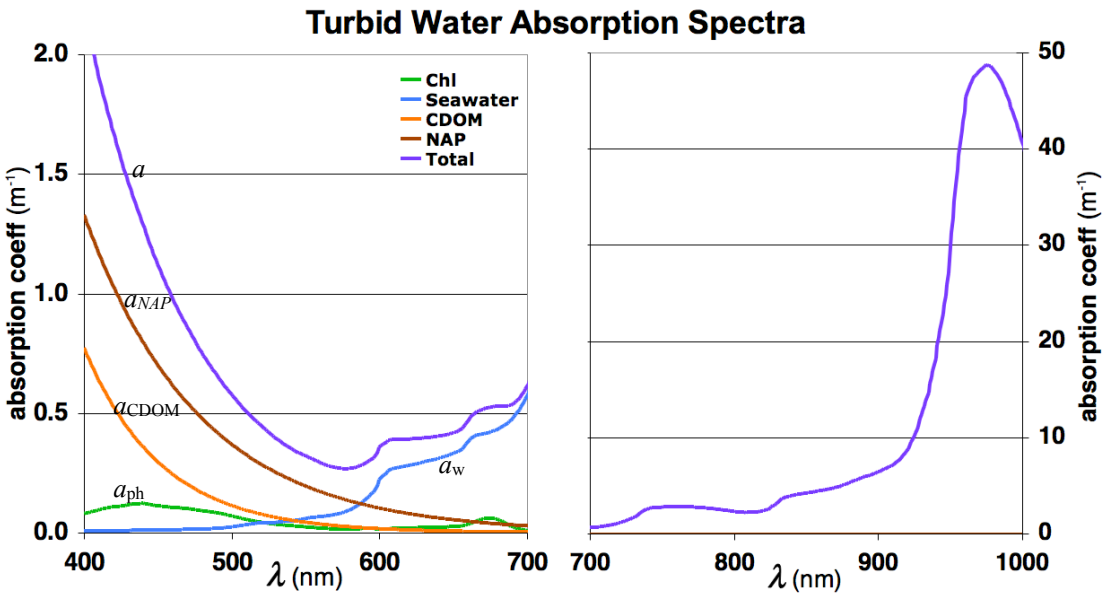

Figure D-1. Shallow water absorption spectra components. Shown are total absorption and the absoption spectrum for water, a_w, phytoplankton, a_{ph}, for CDOM, a_{CDOM}, and for non-algal particles, a_{NAP}. As an example, C_a is set to 3 mg m-3 for the calculation of a_{ph}.

where, b_w is the backscatter of water, taken from Morel (1974) and the scatter due to particles, b_p, is estimated according to Lee et al. (1999) as

$$b_p = \frac{550}{\lambda} \Re \cdot C_a^{0.62} \qquad \text{Eq. D-5}$$

where $\Re$ is set to 5.0 for the highly turbid waters found along coasts. b_b is generally taken to be 0.019 times b. Figure D-2 illustrates the backscatter spectra for these components.

Typically, when the water optical depth is large enough to obscure the bottom, which is often the case in a marsh setting, submerged leaves can be a strong reflector, particularly in the near-infrared.

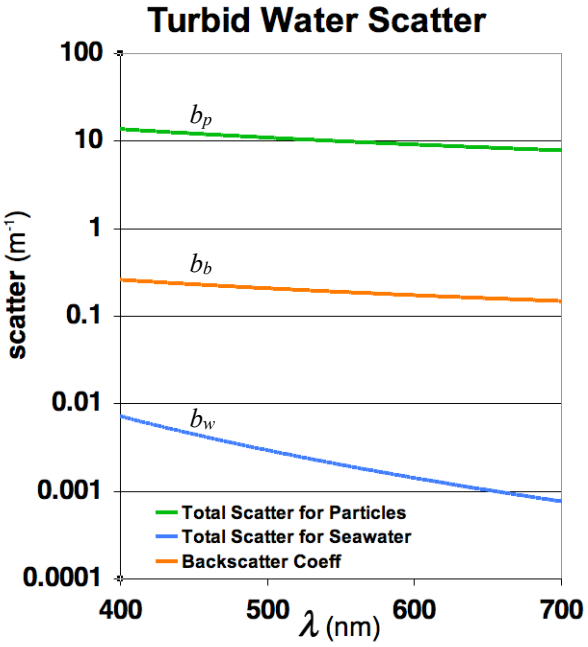

Figure D-2. Total scatter coefficients. Shown are total scatter coefficients for water, b_w, and particles, b_p, and backscatter co-efficient, b_b, where $\Re$ = 5 and C_a = 3.

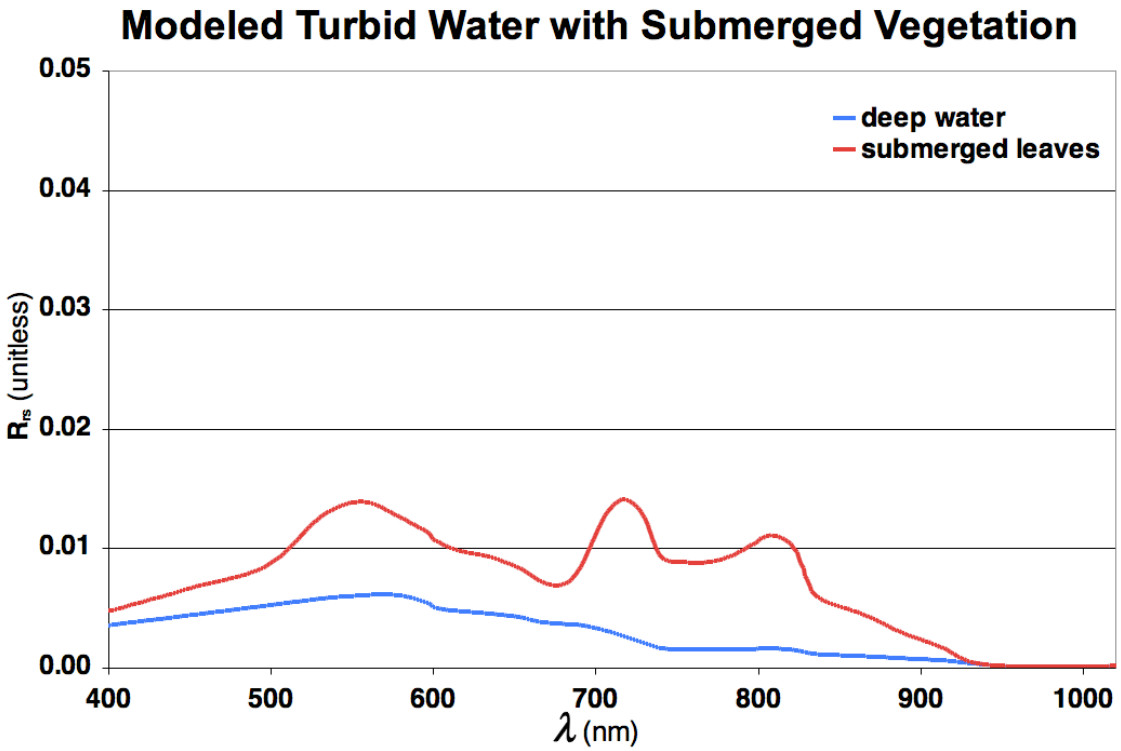

Figure D-3. Reflectance spectra for deep turbid water and and turbid water with submerged leaves near the surface. In this example, H = 25 cm, C_a = 3 mg m^{-3}, and SPM = 0.3 g m^{-3}.

Otherwise, soil and decaying vegetation contribute to the reflectance spectrum. For this study, ρ_b was set to the leaf reflectance spectrum of marsh vegetation, specifically that of the ubiquitous grass *Spartina alterniflora* (Ramsey and Rangoonwala, 2005), however most any species could be used. Figure D-3 illustrates the resulting spectrum for H = 25cm, C_a = 3 mg m^{-3}, and SPM = 0.3 g m^{-3}.

Appendix E - Aquatic Background Code

The WCRM model is a variant of the ACRM model, which is an agglomeration of models representing different optical components of a vegetation canopy. A diagram illustrating the relationship of these models and their input parameters is given in Figure E-1. WCRM replaces the boundary condition of the radiative transfer model for the vegetation canopy with a linear combination of the existing soil BRDF model and an aquatic surface reflectance model. The aquatic surface reflectance model is an

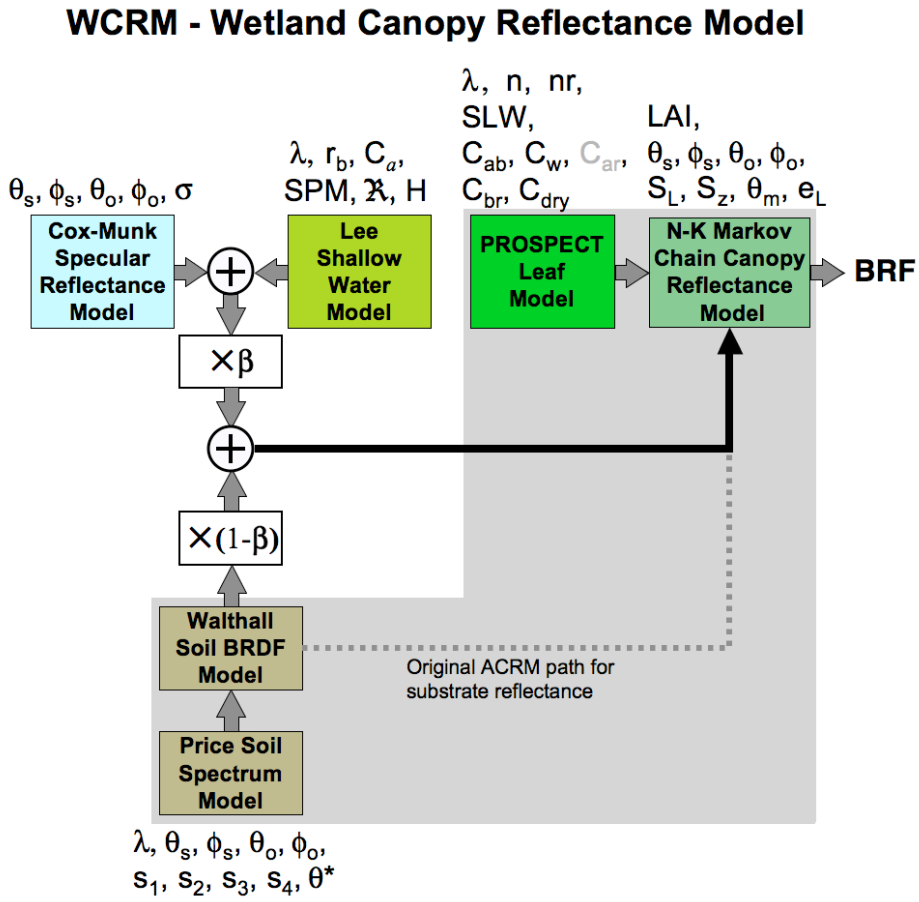

Figure E-1. Calculation flow diagram. This diagram shows how the main components work together. The gray area includes components that were originally part of the original ACRM model. Above or below each component are shown its input parameters, which are defined in Table E-1. The parameter C_{ar}, the concentration of leaf carotenoid pigments, was not included in this study because ACRM uses the PROSPECT 3 model. Future updates to the model should include PROSPECT 5, which includes C_{ar}.

Table E-1. Defined are the input parameters to WCRM as shown in Figure E-1. Also given is the general aspect of canopy light propagation that each parameter affects.

Input Parameter	Use	Description
β	Soil and Water	Fraction of canopy bottom water coverage (unitless).
ϕ_0	Canopy, Soil, Specular	Solar azimuth angle (radians).
ϕ_s	Canopy, Soil, Specular	Observation azimuth angle (radians).
λ	Soil, Water diffuse reflectance, Leaf reflectance, Sky irradiance.	Wavelength (nm) of light propagating through canopy.
θ_0	Canopy, Soil, Specular	Solar zenith angle (radians).
θ_s	Canopy, Soil, Specular	Observation zenith angle (radians).
θ^*	Soil reflectance	Solar zenith reference angle (radians).
θ_m	Canopy light field	Modal leaf angle (radians).
σ	Water specular reflectance	Water surface roughness (unitless).
C_a	Water diffuse reflectance	Water chlorophyll a concentration (mg m^{-3}).
C_{ab}	PROSPECT3 leaf optics	Concentration of chlorophyll a and b pigments (% specific leaf weight).
C_{ar}	PROSPECT5 leaf optics	Concentration of carotenoid pigments (g m^{-2}).
C_{br}	PROSPECT3 leaf optics	Concentration of brown pigments (% specific leaf weight).
C_{dry}	PROSPECT3 leaf optics	Concentration of dry material (% specific leaf weight).
C_w	PROSPECT3 leaf optics	Leaf water equivalent thickness (cm).
e_L	Canopy light field	$=-ln(1 - \varepsilon)$, ε is the eccentricity of the elliptical leaf angle distribution.
H	Water diffuse reflectance	Effective depth to submerged diffuse reflector (m).
LAI	Canopy transmittance	Leaf area index, which is the ratio of one-sided leaf area to horizontal unit ground area (m^2m^{-2}).
n	PROSPECT3 leaf optics	Number of elementary layers within a leaf (integral number).
nr	PROSPECT3 leaf optics	Ratio of refractive indices of leaf surface wax and internal medium.

Table E-1. - continued.

Input Parameter	Use	Description
$\mathfrak{R}$	Water diffuse reflectance	Bio-optical parameter relating particulate backscatter to water turbidity.
r_b	Water diffuse reflectance	Submerged surface reflectance.
s_1	Soil spectrum	1st Price soil spectrum coefficient (unitless).
s_2	Soil spectrum	2nd Price soil spectrum coefficient (unitless).
s_3	Soil spectrum	3rd Price soil spectrum coefficient (unitless).
s_4	Soil spectrum	4th Price soil spectrum coefficient (unitless).
S_L	Canopy light field	Relative length of leaves. (m m^{-1}).
SLW	PROSPECT3 leaf optics	Specific leaf weight (g m^{-2}).
SPM	Water diffuse reflectance	Suspended particulate matter.
S_z	Canopy light field	Markov parameter (unitless); accounts for correlated leaf layers.

application of the shallow water model by Lee et al. In this study, leaf reflectance characteristics are used the bottom reflectance, as described in Appendix D. However, other surfaces reflectance spectra, or mixtures of spectra, could also be used for different wetland conditions. In this study, the shallow water model was implemented using Excel spreadsheets, and the results were fed to WCRM as an input text file. However, for future use, the shallow water model could be easily be coded for direct application with WCRM.

Like ACRM, WCRM code modules were implemented in the FORTRAN language (although, they were prototyped in the IDL language). The following is a listing of all FORTRAN code models that were implemented for this study and combined to ACRM to created. Also, included are the code modules in ACRM that were modified to facilitate the merger of the two models. Figure E-2 illustrates the hierarchical relationship of these code models.

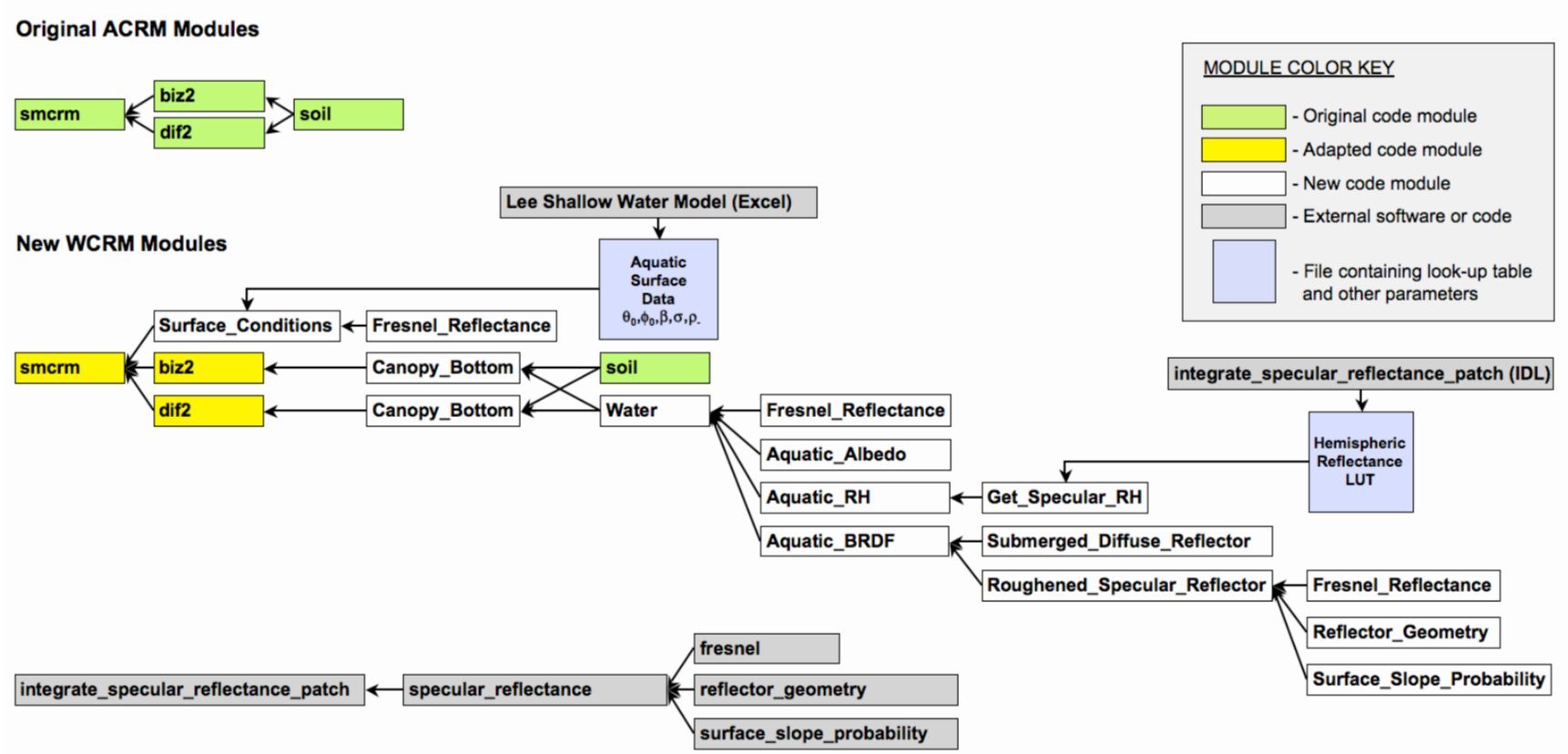

Figure E-2. Hierarchical structure diagram. This diagram shows the relationship of the new aquatic background code modules to the original ACRM code. The smcrm subroutine drives all calculations for the ACRM and WCRM models. The original subroutines dif2 and biz2 handle the diffuse and direct streams, respectively. These routines were adapted to call new modules related to the aquatic background. Other various subroutines, including the modules for leaf optics (PROSPECT and LIBERTY), sky spectrum, and the various higher level driving routine are not shown because no more than superficial changes were made to these routines. External calculations that are indicated are not listed in this document.

```
c Aquatic Background Subroutines and Functions - KRT - 20110406
c
c--------------------------------------------------------------------
c
      Subroutine Surface_Conditions( wlgth, beta, rd,  sig )
c
         Implicit None
c
         Integer          LUN,    N_wl,   Stat,
     &                    i,      j,      di,     h
c
         Double Precision wlgth,  pwlgth, BRF,
     &                    beta,   rd,     sig,
     &                    beta_x, rd_x,   sig_x,
     &                    thetv,  phiv,   thets,  phis,
     &                    Max_wl, Min_wl,
     &                    tdaw,   tuwa,   gamma,
     &                    nr,     rho,    m,
     &                    dr,     a,      w,      pi
c
         Double Precision wlarr(2001), rho_msrd(2001)
c
         Double Precision Fresnel_Reflectance
c
         Data a/1.000274d0/, w/1.34d0/, gamma/0.48d0/,
     &        dr/1.745329251994330d-2/, pi/3.14159265358979d0/
c
         Data N_wl/2001/
c
         Common / Aquatic_Surface / beta_x,  rd_x,    sig_x,
     &                              wlarr,   rho_msrd,
     &                              thetv,   phiv,    thets,   phis,
     &                              pwlgth,  N_wl,    Stat
c
         beta = beta_x
         rd   = rd_x
         sig  = sig_x
c
         If (Stat .NE. 1) then
c
            LUN  = 2
            Open( LUN, file = 'aquatic_surface.dat', status = 'old' )
c
            Read( LUN, * )
```

```
            Read( LUN, * ) beta
            Read( LUN, '(/)' )
            Read( LUN, * ) sig
            Read( LUN, '(2/)' )
            Read( LUN, * ) thetv, phiv
            Read( LUN, '(/)' )
            Read( LUN, * ) thets, phis
            Read( LUN, '(/)' )
c
            Do i = 1, N_wl
               Read( LUN, * ) wlarr(i), BRF
               rho_msrd(i) = BRF/100.0d0/pi
            EndDo
c
            Stat = 1
            Close( LUN )
c
            beta_x = beta
            sig_x  = sig
         EndIF
c
         If (wlgth .NE. pwlgth) then
c
            pwlgth = wlgth
c
            Min_wl = wlarr(1)
            Max_wl = wlarr(N_wl)
c
            i  = 1
            j  = N_wl
c
c           Check for wavelength range edge or beyond
            If (wlgth .GE. Max_wl) then
               j = N_wl
               i = j - 1
            EndIf
c
            If (wlgth .LE. Min_wl) then
               i = 1
               j = i + 1
            EndIf
c
c           Perform binary search along index for wavelength:
c
            di = j - i
  100       If (di .GT. 1) then
```

```
               h = di/2 + i
               If (wlgth .LT. wlarr(h)) then
                  j = h
               Else
                  i = h
               EndIf
               di = j - i
               GoTo 100
            EndIf
c
            m    = (rho_msrd(j)-rho_msrd(i)) / (wlarr(j)-wlarr(i))
            rho  = m * (wlgth-wlarr(j)) + rho_msrd(i)
c
            tdaw = 1.0d0 - Fresnel_Reflectance( thets*dr, a, w )
            tuwa = 1.0d0 - Fresnel_Reflectance( thetv*dr, a, w )
c
            nr   = a/w
            rd   = rho / (nr*nr*tdaw*tuwa/pi + gamma*rho)
c
            rd_x = rd
         EndIf
c
         Return
      End
c
c-----------------------------------------------------------------------
c
      Subroutine Canopy_Bottom( rsl,     beta,    rd,      sig,
     &                          thetv,   thets,   thss,    dphi,
     &                          rsosurf, rsdsurf, rodsurf, rddsurf )
c
         Implicit None
         Double Precision beta,     rsl,      rd,       sig,
     &                    thetv,    thets,    thss,     dphi,
     &                    rsosoil,  rsdsoil,  rodsoil,  rddsoil,
     &                    rsowater, rsdwater, rodwater, rddwater,
     &                    rsosurf,  rsdsurf,  rodsurf,  rddsurf
c
         rsowater = 0.0d0
         rsdwater = 0.0d0
         rodwater = 0.0d0
         rddwater = 0.0d0
c
         Call Water( rd,       sig,
     &               thetv,    thets,    dphi,
     &               rsowater, rsdwater, rodwater, rddwater )
```

```
c
         Call Soil(  rsl,      thetv,    thets,    thss,     dphi,
     &               rsosoil,  rsdsoil,  rodsoil,  rddsoil )
c
         rsosurf = beta * rsowater + (1.0d0-beta)*rsosoil
         rsdsurf = beta * rsdwater + (1.0d0-beta)*rsdsoil
         rodsurf = beta * rodwater + (1.0d0-beta)*rodsoil
         rddsurf = beta * rddwater + (1.0d0-beta)*rddsoil
c
      Return
      End
c
c-----------------------------------------------------------------------
c
      Subroutine Water( rd,   sig,
     &                  th2,  th1,  dph,
     &                  rso,  rsd,  rod,  rdd )
c
         Implicit Double Precision (a-h, o-z)
c
         Data a/1.000274d0/, w/1.34d0/, pi/3.14159265358979d0/
c
c        Calc Fresnel transmittances in and out of water:
         tdaw = 1.0d0 - Fresnel_Reflectance( th1, a, w )
         tuwa = 1.0d0 - Fresnel_Reflectance( th2, a, w )
c
c        Calc BRF=pi*BRDF, Hemispheric Reflectances, and Albedo:
         rso = Aquatic_BRDF  ( rd, tdaw, tuwa, sig, th1,th2, dph ) * pi
         rsd = Aquatic_RH    ( rd, tdaw, sig, th1 )
         rod = Aquatic_RH    ( rd, tuwa, sig, th2 )
         rdd = Aquatic_Albedo( rd )
c
         Return
      End
c
c-----------------------------------------------------------------------
c
      Function Aquatic_Albedo( rd )
c
         Implicit Double Precision (a-h, o-z)
c
         Data a/1.000274d0/, w/1.34d0/
c
c        Air-Water Inteface from numerical integration.
         As  = 0.0267d0
c
```

```
c        Index of refraction ratio
         r   = a / w
c
c        Internal reflectance coeff (Lyzenga 1978), from Lee et al 1998.
         gm  = 0.48d0
c
c        Numerically integrated Fresnel transmittance.
         T   = 0.93255058d0
c
         Ad  = (T*r)*(T*r) * rd / (1.0d0 - gm*rd)
c
         Aquatic_Albedo = As + Ad
c
         Return
      End
c
c-----------------------------------------------------------------------
c
      Function Aquatic_RH( rd, tf, sig, th )
c
         Implicit Double Precision (a-h, o-z)
c
         Data a/1.000274d0/, w/1.34d0/
c
c        Interpolate specular hemispheric reflectance look-up table
         RHs = Get_Specular_RH( th, sig )
c
         r   = a / w
c
c        Internal reflectance coeff (Lyzenga 1978), from Lee et al 1998.
         gm  = 0.48d0
c
c        Numerically integrated Fresnel transmittance
         T   = 0.93255058d0
c
c        Compute diffuse hemispheric reflectance
         RHd = rd * T * tf * r*r / (1.0d0 - gm*rd)
c
         Aquatic_RH = RHs + RHd
         Return
      End
c
c-----------------------------------------------------------------------
c
      Double Precision Function Get_Specular_RH( th_rad, sig )
c
```

```
      Implicit None
c
      Integer LUN, di, dk, h, i, j, k, l, ns, nt, Stat
c
      Double Precision RH_LUT(91,16), RH_T(91), RH_S(16),
     &                 Min_T, Max_T, Min_S, Max_S, as, at,
     &                 RHa, RHb, RH, pi, dr, th, th_rad, sig
c
      Data dr/1.745329251994330d-2/, pi/3.14159265358979d0/
      Data nt/91/, ns/16/
c
      Common / Specular_RH_LUT / RH_T, RH_S, RH_LUT, nt, ns, Stat
c
      LUN = 2
      th  = th_rad / dr
c
   10 Format( 16F10.7 )
c
      If (Stat .NE. 1) then
         Open( LUN, File = "specular_rh.dat", Status="OLD" )
         Read( LUN, * ) (RH_T(i), i = 1, nt)
         Read( LUN, * ) (RH_S(i), i = 1, ns)
         Read( LUN, 10 ) ((RH_LUT(i,j), j = 1, ns), i = 1, nt)
         Stat = 1
         Close( LUN )
      EndIf
c
      Max_T = RH_T(nt)
      Max_S = RH_S(ns)
c
      Min_T = RH_T(1)
      Min_S = RH_S(1)
c
      i  = 1
      j  = nt
      at = Abs( th )
c
c     Check for table edge or beyond
      If (at .GE. Max_T) then
         j = nt
         i = j - 1
      EndIf
c
      If (at .LE. Min_T) then
         i = 1
         j = i + 1
```

```
         EndIf
c
c        Perform binary search along index for zenith angle, theta:
c
         di = j - i
  100    If (di .GT. 1) then
            h = di/2 + i
            If (at .LT. RH_T(h)) then
               j = h
            Else
               i = h
            EndIf
            di = j - i
            GoTo 100
         EndIf
c
         k  = 1
         l  = ns
         as = Abs( Sig )
c
c        Check for table edge or beyond
         If (as .GE. Max_S) then
            l = ns - 1
            k = l - 1
         EndIf
c
         If (as .LE. Min_S) then
            k = 1
            l = k + 1
         EndIf
c
c        Perform binary search along index for surf roughness parameter, sigma:
c
         dk = l - k
  200    If (dk .GT. 1) then
            h = dk/2 + k
            If (as .LT. RH_S(h)) then
               l = h
            Else
               k = h
            EndIf
            dk = l - k
            GoTo 200
         EndIf
c
         RHa = (RH_LUT(j,k)-RH_LUT(i,k))*(th-RH_T(i)) + RH_LUT(i,k)
```

```
         RHb = (RH_LUT(j,l)-RH_LUT(i,l))*(th-RH_T(i)) + RH_LUT(i,l)

         RH  = (RHb-RHa)/(RH_S(l)-RH_S(k))*(Sig-RH_S(k)) + RHa
c
         Get_Specular_RH = RH * pi
c
         Return
      End
c
c--------------------------------------------------------------------
c
      Function Aquatic_BRDF( rd, tdaw, tuwa, sig, ths, tho, dph )
c
         Implicit Double Precision (a-h, o-z)
c
         Rdiff = Submerged_Diffuse_Reflector( rd, tdaw, tuwa, ths, tho)
         Rspec = Roughened_Specular_Reflector( sig, ths, tho, dph )
c
         Aquatic_BRDF = Rspec + Rdiff
         Return
      End
c
c--------------------------------------------------------------------
c
      Function Submerged_Diffuse_Reflector( rd, tdaw, tuwa )
c
         Implicit Double Precision (a-h, o-z)
c
         Data a/1.000274d0/, w/1.34d0/, pi/3.14159265358979d0/
c
         r      = a / w
c
         Gamma  = 0.48d0
         RInt   = 1.0d0 / (1.0d0 - Gamma*Rd)
c
         Submerged_Diffuse_Reflector = rd * tdaw*tuwa * r*r / pi * RInt
c
         Return
      End
c
c--------------------------------------------------------------------
c
      Function Roughened_Specular_Reflector( sig, ths, tho, dph )
c
c        Uses directionless wind surface roughing model based on
c        Cox & Munk (1954) and Kay,Lavender,and Hedley (2009).
```

```
c
         Implicit Double Precision (a-h, o-z)
c
         Data a/1.000274d0/, w/1.34d0/
c
         Call Reflector_Geometry( ths, tho, dph, zx, zy, cosom, costhn )
         omega = Abs( ACos( cosom ) )
c
         Rf = Fresnel_Reflectance( omega, a, w )
c
         P  = Surface_Slope_Probability( zx, zy, sig ) /
     &        ( 4.0d0*Costhn**4.0d0 * Cos( ths ) * Cos( tho ) )
c
         Roughened_Specular_Reflector = P * Rf
c
         Return
       End
c
c-----------------------------------------------------------------------
c
       Subroutine Reflector_Geometry( thi, thr, dph,
     &                                zx, zy, cosw, costhn )
c
         Implicit Double Precision (a-h, o-z)
c
         sinthi = Sin( thi )
         costhi = Cos( thi )
c
         sinthr = Sin( thr )
         costhr = Cos( thr )
c
c        Slopes of reflecting facets producing highlights:
         z      = costhi + costhr
         zx     = -( sinthi + sinthr*Cos( dph ) ) / z
         zy     = -sinthr*Sin( dph ) / z
c
c        Cosines of the angle (2w) between I and R,
c                   the angle (w)  between I and the normal vector (I+R),
c                   the zenith angle (thn) of the normal vector (I+R)
c
         cos2w  = sinthi*sinthr*Cos( dph ) + costhi*costhr
         cosw   = SqRt( (1.0d0 + cos2w)/2.0d0 )
         costhn = z/(2.0d0*cosw)
c
         Return
       End
```

```
c
c-----------------------------------------------------------------------
c
      Function Surface_Slope_Probability( zx, zy, sig )
c
         Implicit Double Precision (a-h, o-z)
c
         Data pi/3.14159265358979d0/
c
c        Compute surface slope probability:
c
         sig2 = sig*sig
c        (note: in Cox-Munk, sig2 = 0.003 + 0.00512*W, W is windspeed in m/s)
c
         Surface_Slope_Probability =
     &       Exp( -( zx*zx + zy*zy )/(2.0d0*sig2) ) /
     &                     (2.0d0*pi*sig2)
      End
c
c-----------------------------------------------------------------------
c
      Function Fresnel_Reflectance( t_i, r1, r2 )
c
         Implicit Double Precision (a-h, o-z)
c
c        t_i = incident zenith angle in radians
c
c        Compute ratio of the index of refractions
         rn  = r1 / r2
c
         Rs  = (r1-r2)/(r1+r2)
c
         Rs  = Rs*Rs
         Rp  = Rs
c
         sin_t_t = Sin( t_i ) * rn
c
         If ((t_i .NE. 0.0d0) .AND. (Sin_t_t .LE. 1.0d0)) then
c
            t_t = ASin( sin_t_t )
c
            Rs = ( Sin( t_i - t_t ) /
     &             Sin( t_i + t_t ) )
c
            Rs = Rs*Rs
c
```

```
            Rp = ( Tan( t_i - t_t ) /
     &             Tan( t_i + t_t ) )
c
            Rp = Rp*Rp
         EndIf
c
         If (sin_t_t .GT. 1.0d0) then
            Rs = 1.0d0
            Rp = 1.0d0
         EndIf
c
         Fresnel_Reflectance = (Rs + Rp) / 2.0d0
c
         Return
      End
c
c-----------------------------------------------------------------------
c
```

Appendix F - Challenges of Field Work in Coastal Marshes

A number of challenges exist when measuring either LAI or spectral reflectance in a coastal marsh. This appendix discusses issues that should be addressed when making these measurements in the field. The intent here is to use experience in the field to set the direction for future work that could lead to a marsh remote sensing protocol. Such a protocol would be invaluable to wetland researchers in combining and comparing their data. A protocol would also help guide both novice and veteran researchers with standard methodologies that would promote the quality of the data that they collect.

He et al. (2007) identified three sources of biases in making LAI measurements with a LI-COR LAI2000 plant canopy analyzer. The first is the mentioned LAI underestimate from light scattered from leaves lower in an erectophile canopy (LI-COR, 1992; Stroppiana*, et al.*, 2006). They also point out that in graminaceous canopies, it is impossible to not disturb the canopy with the sensor, causing a further underestimate. Finally, they point to the problem of graminaceous canopies being spatially distributed in clumps, introducing additional variation in the measurements that affect accuracy. These complications affect the accuracy of LAI measurements and require special attention during field work. In addition, the presence of standing dead vegetation typically found with some marsh species complicate the meaningfulness of indirect methods of measuring LAI.

Variation in canopy structure can also be related to variation in plant height, structure of individual plants (e.g., leaf angle), and ground distribution. Plant height and structure tended to differ by species, but could be affected by marsh drainage properties (e.g., short form and tall form of *Spartina alterniflora*). Ground distribution ranges from homogeneous cover to hummocky, where plants formed clumps surrounded by water or mud filled hollows or even small islands within ponds. In these cases, it was a challenge to devise a sampling scheme for the LAI2000 sub-canopy measurements. It was decided

that half of the measurements would be taken between plant clumps and half would be taken within clumps because of their proximity to each other. However, in areas where interstitial changes are larger or clumps are further apart, that scheme might have to be adjusted in order to get an unbiased estimate of the LAI for the canopy.

Above canopy reflectance measurements may likewise be challenged, but Figure 4-3 suggests that the NIR reflectance might provide sufficient response to change in canopy densities for the sites studied during the short transect experiment. Sensitivity analysis of WCRM indicated that the model also continued to have a strong relationship between NIR reflectance and LAI. The primary limitation of using WCRM for this type of application is its expectation of a canopy reflectance that is much higher than marsh plant species, which is a problem that stems from application of the PROSPECT leaf reflectance model. Improving the control of the PROSPECT model so that it better represents these darker canopies would greatly help the LAI underestimate. Further work should be done to determine whether this relationship can be effectively exploited to use NIR reflectance to determine LAI for dense marsh canopies using an improved WCRM model or some other method.

The retention of standing dead vegetation in the canopy of some species was discussed in Chapters 3 and 6 in terms of its strong influence on the reflectance spectrum of the canopy. The mixture of live and dead plants (and patches of soil and water), increases the canopy reflectance variation over small spatial scales. However, the presence of dead vegetation also impacts the meaningfulness of LAI measurements. Because the LAI-2000 measurements are based on the canopy gap fraction, any body that is opaque at blue wavelength would be included in the estimate of canopy LAI. Therefore the LAI-2000 measures a foliage area index (LI-COR, 1992). Furthermore, this means that for plants with high lignin content that kept standing dead stock from previous growth cycles, the LAI-2000 is over estimating the "green" LAI. In the study regions this would include species such as *Phragmites spp*, *Spartina cynosurides*,

Schoenoplectus, and *Juncus spp*, but probably applies to most large grass species, sedges, and rushes. Such LAI measurements could lead to an overestimate of green biomass or productivity.

Given the observed variation in spectral reflectance, a dense sample was necessary to obtain a good estimate canopy structure. In this study, however, the spectrometer sampling rate was only sufficient to obtain dense samples over relatively short transects for several angles. To get greater spatial or angular coverage will require higher sampling rates, by at least an order of magnitude. In addition, having an additional sensor to monitor the solar irradiance would save time, providing opportunity to make more measurements while in the field. What is more important, accounting for contemporaneous variation in the solar irradiance field would open the opportunity to take measurements under less than perfect sky conditions, further increasing the number of sites that can be measured during a growing season.

An import objective of marsh canopy remote sensing is determining the spatial distribution of marsh physical and biological properties. Interestingly, the spatial distribution of plants within marsh canopies can pose challenges to obtaining LAI or spectral reflectance using light sensing instruments. The distribution of small open bodies of water and open mud flats can further complicate remote sensing imagery. Considerable future work needs to be done to account for the effects that can arise from the spatial distribution of plants. This would include a close evaluation of sampling methods for ground measurements and the development of a landscape scale canopy reflectance model to deal with effects at remote sensing scales. WCRM could contribute to those efforts.

Graminaceous plants can produce thick canopies with a dense root network, which is a useful trait in an environment extremely vulnerable to erosion. Conversely, marsh vegetation that succumbs to stressing conditions, such as relative sea level rise, can be quickly replaced by open water (Kearney*, et al.*, 1988). Examination of aerial photos

from 2005 to 2007 and field observations during the 2007 and 2008 visibly showed no appreciable change in marsh plant distribution in the Blackwater Marsh study area. Therefore that region could be considered relatively stable, at least during the period of study, and most marsh plants were in dense expanses or clumps.

Much of the marsh in study area along the road in the Blackwater Marsh was far from the well drained bank marshes. Inner marshes are subject to stressing conditions, such a poor drainage, variable salinity, and low redox potentials. These conditions can give rise to stable hummock-hollow microtopography. Hummocks consists of clumps of dense vegetation with a thick root network situated on a stack of peat and soil. There is evidence that this formation enables the plants to influence the chemical and hydrological characteristics of the hummock soil to their advantage (Stribling*, et al.*, 2007; Stribling*, et al.*, 2006). Hollows are lower elevation spaces between hummocks that characteristically are unvegetated and often inundated. Thus, a hummock-hollow microtopography enables the plant also keep their local density quite high, while the canopy becomes a complex of vegetation clumps separated by interstitial spaces of open water. Given their general distance from banks of the Blackwater River, a large portion of the canopies measured in the Blackwater Marsh study area had a hummock-hollow microtopography. This was particularly notable in Sites 1 and 3 of the short transect experiment and most measurements taken in canopies of *Schoenoplectus americanus* in the inner marsh.

Dense foliage conditions present a number of issues when making measurements in marsh canopies. This decreases effectiveness of the indirect methods explored in this study. The amount of foliage within a single hummock or within a relatively homogeneously distributed canopy hummocks can be too high to get an accurate reading of LAI. Marsh canopies examined this study were observed to be densely populated, with most of the LAI measurements ranging between 2.5 to 3.5. This poses a challenge for indirect measurements like those taken with an LAI2000 because sensor sensitivity to variation in canopy density decreases as LAI becomes high (LAI > 3) and the gap

fraction saturates near 4 to 5 (Garrigues*, et al.*, 2008; Gower, 1999). In addition, sensitivity analysis of the retrieval of LAI through inverse of ACRM or WCRM lose their ability to respond changes in reflectance as LAI between 3 and 4 for blue wavelengths and perhaps higher for the NIR wavelengths, which agrees with theoretical limits estimated by Gobron et al. (1997). Therefore, the natural thickness of fully grown marsh vegetation can hamper the measurement of LAI.

The hummock-hollow microtopography greatly increases the measurement variability for LAI and spectral reflectance measurements over small spatial scales. Such conditions also increase the probability of specularly reflected sunlight or skylight reaching the sensor. Heterogeneity of the canopy distribution can confound the homogeneity assumption made by the LI-COR LAI-2000 algorithm that converts canopy transmittance into LAI, or most canopy reflectance models in predicting BRDF. Furthermore, it is known that a sub-canopy transmittance measurement, like those taken by a LI-COR LAI-2000 plant canopy analyzer, is subject to underestimate LAI because of single scattering off leaves at the bottom of a mostly erectophile canopy (LI-COR, 1992; Stroppiana*, et al.*, 2006). The effect could be exaggerated by the lateral position of the sensor relative to hummocks. It would be useful to study what sampling techniques are effect for this type of distribution.

In a natural setting, canopy properties present are subject to high variability, even in monospecific canopies. ACRM has mostly been applied to uniform agricultural canopies (Delalieux*, et al.*, 2008; Houborg*, et al.*, 2009; Houborg and Boegh, 2008; Weihs, 2008). Greater uniformity may be found in inundated agricultural canopies, such a rice paddies, where growth and background conditions are artificially controlled. WCRM may have better performance for such situation, where conditions are more homogeneous and similar work has shown promise (Xiao*, et al.*, 2002). Because the model could provide utility for such applications, its performance should be evaluated in future work. In addition, measurements of LAI might be more applicable to canopies

with less standing dead vegetation present, during the early part of the growing cycle when LAI is lower than 3. Thus, the early growth of species like *Spartina altnerniflora* or *Spartina patens* would be idea subjects for future work on LAI retrievals from above-canopy reflectance.

Special attention is needed to address all of various challenges in making indirect measurements of LAI or canopy spectral reflectance. In particular, if large scale surveys are employed to support remote sensing effort (e.g, for satellite or areal sensor measurement validation), these sources of bias need to be addressed in a standard and consistent fashion. Therefore, it is recommended that field measurement protocol be developed for wetlands. Using a standard protocol will help guide practitioners in the field between teams and between campaigns in assuring that all biases have been addressed in a consistent fashion and provide a reference to inform novice instrument operators, and remind experienced instrument operators, of the standard techniques that should be used for marsh environments.

Bibliography

Adam E, and Mutanga O. 2009. Spectral discrimination of papyrus vegetation (Cyperus papyrus L.) in swamp wetlands using field spectrometry. ISPRS Journal of Photogrammetry and Remote Sensing 64(6):612-620.

Adam E; Mutanga O, and Rugege D. 2009. Multispectral and hyperspectral remote sensing for identification and mapping of wetland vegetation: A review. Wetlands Ecology and Management 18(3):281-296.

Adam P. 1990. Saltmarsh ecology. Cambridge, England: Cambridge University Press.

Adam P. 2002. Saltmarshes in a time of change. Environmental Conservation 29:39-61.

Andrew M, and Ustin S. 2008. The role of environmental context in mapping invasive plants with hyperspectral image data. Remote Sensing of Environment 112(12): 4301-4317.

Artigas FJ, and Yang JS. 2005. Hyperspectral remote sensing of marsh species and plant vigour gradient in the New Jersey Meadowlands. International Journal of Remote Sensing 26(23):5209-5220.

Barbier EB; Hacker SD; Kennedy C; Koch EW; Stier AC, and Silliman BR. 2011. The value of estuarine and coastal ecosystem services. Ecological Monographs 81(2): 169-193.

Barducci A; Guzzi D; Marcoionni P, and Pippi I. 2009. Aerospace wetland monitoring by hyperspectral imaging sensors: A case study in the coastal zone of San Rossore natural park. Journal of Environmental Management 90(7):2278-2286.

Bell FW. 1997. The economic valuation of saltwater marsh supporting marine recreational fishing in the southeastern United States. Ecological Economics 21 (3):243-254.

Boesch DF, Turner, R.E. 1984. Dependence of fishery species on salt marshes: The role of food and refuge. Estuaries 7:460–468.

Bohren CF, and Clothiaux EF. 2006. Fundamentals of atmospheric radiation: An introduction with 400 problems. Weinheim, Federal Republic of Germany: Wiley-VCH Verlag GmbH & Co. KGaA. p. 208-211.

Boochs F; Kupfer G; Dockter K, and Kuhbauch W. 1990. Shape of the red edge as vitality indicator for plants. International Journal of Remote Sensing 11(10): 1741-1753.

Bricaud A; Babin M; Morel A, and Claustre H. 1995. Variability in the chlorophyll-specific absorption-coefficients of natural phytoplankton - analysis and parameterization. Journal of Geophysical Research-Oceans 100(C7): 13321-13332.

Bromberg-Gedan K; Silliman BR, and Bertness MD. 2009. Centuries of human-driven change in salt marsh ecosystems. Annual Review of Marine Science 1(1): 117-141.

Brown de Colstoun E, and Walthall C. 2006. Improving global scale land cover classifications with multi-directional POLDER data and a decision tree classifier. Remote Sensing of Environment 100(4):474-485.

Buiteveld H, Hakvoort, J.H.M., Donze, M. 1994. The optical properties of pure water. In: Jaffe JS, editor. SPIE Proceedings on Ocean Optics XII. p. 10.

Casella G, Berger, R.L. 1990. Statistical inference. Belmont, California: Duxbury Press, a division of Wadsworth, Inc.

Cebrian J. 2002. Variability and control of carbon consumption, export, and accumulation in marine communities. Limnology and Oceanography 47(1):11-22.

Chopping, and M. 2003. Canopy attributes of desert grassland and transition communities derived from multiangular airborne imagery. Remote Sensing of Environment 85 (3):339-354.

Clevers J; Kooistra L, and Salas EAL. 2004. Study of heavy metal contamination in river floodplains using the red-edge position in spectroscopic data. International Journal of Remote Sensing 25(19):3883-3895.

Costanza R, d'Arge, Ralph, de Groot, Rudolf, Farber, Stephen, Grasso, Monica, Hannon, Bruce, Limburg, Karin, Naeem, Shahid, O'Neill, Robert V., Paruelo, Jose, Raskin, Robert G., Sutton, Paul, van den Belt, Marjan. 1997. The value of the world's ecosystem services and natural capital. Nature 387:253-260.

Cox C, and Munk W. 1954a. Measurement of the roughness of the sea surface from photographs of the suns glitter. Journal of the Optical Society of America 44(11): 838-850.

Cox C, and Munk W. 1954b. Statistics of the sea surface derived from sun glitter. Journal of Marine Research 13(2):198-227.

Cox C, and Munk W. 1956. Slopes of the sea surface deduced from photographs of sun glitter. La Jolla, CA, USA: University of California Press, Berkley and Los Angeles, Cambridge University Press, London. p. 401-488.

Cox DD. 2002. A naturalist's guide to wetland plants – an ecology for Eastern North America. Syracuse, New York: Syracuse University Press. p. 5.

Dahl TE. 2011. Status and trends of wetlands in the conterminous United States 2004 to 2009. Washington, D.C.: U.S. Department of the Interior; Fish and Wildlife Service.

Day JW, Jr., Hall, C.A.S., Kemp, W.M., Yanez-Arancibia, A. 1989. Estuarine ecology. New York: John Wiley & Sons.

Delalieux S; Somers B; Hereijgers S; Verstraeten WW; Keulemans W, and Coppin P. 2008. A near-infrared narrow-waveband ratio to determine leaf area index in orchards. Remote Sensing of Environment 112(10):3762-3772.

Engle VD. 2011. Estimating the provision of ecosystem services by gulf of mexico coastal wetlands. Wetlands 31(1):179-193.

Erickson JE; Megonigal JP; Peresta G, and Drake BG. 2007. Salinity and sea level mediate elevated CO2 effects on C3/C4 plant interactions and tissue nitrogen in a Chesapeake Bay tidal wetland. Global Change Biology 13(1):202-215.

Field R. 2006. Personal communication - phone discussion regarding various marsh conditions encountered in his years of field work.

Filella I, and Penuelas J. 1994. The red edge position and shape as indicators of plant chlorophyll content, biomass and hydric status. International Journal of Remote Sensing 15(7):1459-1470.

Gao F, Jin, Y., Li, X., Schaaf, C.B., Strahler, A.H. 2002. Bidirectional NDVI and atmospherically resistant BRDF inversion for vegetation canopy. IEEE Transactions on Geoscience and Remote Sensing 40(6):1269-1278.

Garrigues S; Shabanov N; Swanson K; Morisette J; Baret F, and Myneni R. 2008. Intercomparison and sensitivity analysis of leaf area index retrievals from LAI-2000, AccuPAR, and digital hemispherical photography over croplands. Agricultural and Forest Meteorology 148(8-9):1193-1209.

Gates DM; Keegan HJ; Schleter JC, and Weidner VR. 1965. Spectral properties of plants. Appl. Opt. 4(1):11-20.

Gedan KB; Kirwan ML; Wolanski E; Barbier EB, and Silliman BR. 2011. The present and future role of coastal wetland vegetation in protecting shorelines: Answering recent challenges to the paradigm. Climatic Change 106(1):7-29.

Gemmell F. 2000. Testing the utility of multi-angle spectral data for reducing the effects of background spectral variations in forest reflectance model inversion. Remote Sensing of Environment 72(1):46-63.

Gemmell F, and McDonald AJ. 2000. View zenith angle effects on information content of three spectral indices. Remote Sensing of Environment 72(2):139-158.

GER. 1997. Ger-3700 spectroradiometer user's manual, version 2.0. Millbrook, NY: Geophysical Environment Research Corporation.

Gobron N, Pinty, B., Verstraete, M.M. 1997. Theoretical limits to the estimation of the leaf area index on the basis of visible and near-infrared remote sensing data. IEEE Transactions on Geoscience and Remote Sensing 35(6):1438-1445.

Gordon HR; Brown OB; Evans RH; Brown JW; Smith RC; Baker KS, and Clark DK. 1988. A semianalytic radiance model of ocean color. Journal of Geophysical Research-Atmospheres 93(D9):10909-10924.

Goward SN, and Huemmrich KF. 1992. Vegetation canopy PAR absorptance and the normalized difference vegetation index - an assessment using the SAIL model. Remote Sensing of Environment 39(2):119-140.

Gower ST, Kucharik, C.J., Norman, J.M. 1999. Direct and indirect estimation of leaf area index, FAPAR, and net primary production of terrestrial ecosystems. Remote Sensing of Environment 70(1):29-51.

Gross MF; Hardisky MA, and Klemas V. 1988. Effects of solar angle on reflectance from wetland vegetation. Remote Sensing of Environment 26(3):195-212.

He YH; Guo XL, and Wilmshurst JF. 2007. Comparison of different methods for measuring leaf area index in a mixed grassland. Canadian Journal of Plant Science 87(4):803-813.

Horler DNH; Dockray M, and Barber J. 1983. The red edge of plant leaf reflectance. International Journal of Remote Sensing 4(2):273-288.

Houborg R; Anderson M, and Daughtry C. 2009. Utility of an image-based canopy reflectance modeling tool for remote estimation of LAI and leaf chlorophyll content at the field scale. Remote Sensing of Environment 113(1):259-274.

Houborg R, and Boegh E. 2008. Mapping leaf chlorophyll and leaf area index using inverse and forward canopy reflectance modeling and spot reflectance data. Remote Sensing of Environment 112(1):186-202.

Houborg R; Soegaard H, and Boegh E. 2007. Combining vegetation index and model inversion methods for the extraction of key vegetation biophysical parameters using Terra and Aqua MODIS reflectance data. Remote Sensing of Environment 106(1):39-58.

Huemmrich KF, and Goward SN. 1997. Vegetation canopy PAR absorptance and NDVI: An assessment for ten tree species with the SAIL model. Remote Sensing of Environment 61(2):254-269.

Hughes RG. 2004. Climate change and loss of saltmarshes: Consequences for birds. Ibis 146:21-28.

Jacquemoud S, and Baret F. 1990. PROSPECT: A model of leaf optical properties spectra. Remote Sensing of Environment 34(2):75-91.

Jensen JR; Hodgson ME; Christensen E; Mackey HE; Tinney LR, and Sharitz R. 1986. Remote-sensing inland wetlands - a multispectral approach. Photogrammetric Engineering and Remote Sensing 52(1):87-100.

Jollineau MY, and Howarth PJ. 2008. Mapping an inland wetland complex using hyperspectral imagery. International Journal of Remote Sensing 29(12): 3609-3631.

Judd C; Steinberg S; Shaughnessy F, and Crawford G. 2007. Mapping salt marsh vegetation using aerial hyperspectral imagery and linear unmixing in Humboldt bay, California. Wetlands 27(4):1144-1152.

Kay S; Hedley JD, and Lavender S. 2009. Sun glint correction of high and low spatial resolution images of aquatic scenes: A review of methods for visible and near-infrared wavelengths. Remote Sensing 1:697-730.

Kearney MS; Grace RE, and Stevenson JC. 1988. Marsh loss in Nanticoke Estuary, Chesapeake Bay. Geographical Review 78(2):205-220.

Kearney MS, and Riter JCA. 2011. Inter-annual variability in Delaware Bay brackish marsh vegetation, USA. Wetlands Ecology and Management 19(4):373-388.

Kearney MS; Stutzer D; Turpie K, and Stevenson JC. 2009. The effects of tidal inundation on the reflectance characteristics of coastal marsh vegetation. Journal of Coastal Research 25(6):1177-1186.

Klemas V. 2009. The role of remote sensing in predicting and determining coastal storm impacts. Journal of Coastal Research 25(6):1264-1275.

Klemas V. 2011a. Remote sensing of wetlands: Case studies comparing practical techniques. Journal of Coastal Research 27(3):418-427.

Klemas V. 2011b. Remote sensing techniques for studying coastal ecosystems: An overview. Journal of Coastal Research 27(1):2-17.

Klemas VV. 2001. Remote sensing of landscape-level coastal environmental indicators. Environmental Management 27(1):47-57.
Kou LH; Labrie D, and Chylek P. 1993. Refractive-indexes of water and ice in the 0.65-mu-m to 2.5-mu-m spectral range. Applied Optics 32(19):3531-3540.
Kuusk A. 1991. The hot spot effect in plant canopy reflectance. In: Myneni RB, Ross J, editors. Photon-vegetation interactions. Applications in optical remote sensing and plant ecology. Berlin: Springer-Verlag. p. 139-159.
Kuusk A. 1995a. A fast, invertible canopy reflectance model. Remote Sensing of Environment 51(3):342-350.
Kuusk A. 1995b. A Markov-chain model of canopy reflectance. Agricultural and Forest Meteorology 76(3-4):221-236.
Kuusk A. 1996. A computer-efficient plant canopy reflectance model. Computers & Geosciences 22(2):149-163.
Kuusk A. 1998. Monitoring of vegetation parameters on large areas by the inversion of a canopy reflectance model. International Journal of Remote Sensing 19(15): 2893-2905.
Kuusk A. 2009. Two-layer canopy reflectance model ACRM user guide, version 07.2009, 22 july 2009. Tartu, Estonia: Tartu Observatory.
Lang ARG. 1987. Simplied estimate of leaf area index from transmittance of the sun's beam. Agricultural and Forest Meteorology 41:179-186.
Lee ZP; Carder KL; Mobley CD; Steward RG, and Patch JS. 1998. Hyperspectral remote sensing for shallow waters. I. A semianalytical model. Applied Optics 37(27): 6329-6338.
Lee ZP; Carder KL; Mobley CD; Steward RG, and Patch JS. 1999. Hyperspectral remote sensing for shallow waters: 2. Deriving bottom depths and water properties by optimization. Applied Optics 38(18):3831-3843.
Li L; Ustin SL, and Lay M. 2005. Application of multiple endmember spectral mixture analysis (MESMA) to AVIRIS imagery for coastal salt marsh mapping: A case study in China Camp, CA, USA. International Journal of Remote Sensing 26(23): 5193-5207.
LI-COR I. 1992. LAI-2000 plant canopy analyzer operatiing manual. Lincoln, Nebraska.
Lotze HK, Lenihan, Hunter S., Bourque, Bruce J., Bradbury, Roger H., Cooke, Richard G., Kay, Matthew C., Kidwell, Susan M., Kirby, Michael X., Peterson, Charles H., Jackson, Jeremy B. C. 2006. Depletion, degradation, and recovery potential of estuaries and coastal seas. Science 312:1806-1809.
Lyzenga DR. 1978. Passive remote-sensing techniques for mapping water depth and bottom features. Applied Optics 17(3):379-383.
McKee KL; Mendelssohn IA, and Materne MD. 2004. Acute salt marsh dieback in the Mississippi River deltaic plain: A drought-induced phenomenon? Global Ecology and Biogeography 13(1):65-73.
Mendelssohn IA; McKee KL, and Kong T. 2001. A comparison of physiological indicators of sublethal cadmium stress in wetland plants. Environmental and Experimental Botany 46(3):263-275.

Miyamoto M; Yoshino K, and Kushida K. 2001. Relationship between canopy BRDF and physical parameters of 3D structure of vegetation in northern wetlands in Japan. Asian Journal of Geoinformatics 1:14.

Mobley CD. 1994. Light and water: Radiative transfer in natural waters. San Diego, CA, USA: Academic Press.

Morel A. 1974. Optical properties of pure water and pure sea water. In: Jerlov NG, Nielsen, E.S., editor. Optical aspects of oceanography. New York. p. 1-24.

Mutanga O, and Skidmore AK. 2007. Red edge shift and biochemical content in grass canopies. ISPRS Journal of Photogrammetry and Remote Sensing 62(1):34-42.

Nicodemus FE. 1963. Radiance. American Journal of Physics 31(5):368-&.

Nicodemus FE; Richmond JC; Hsia JJ; Ginsberg IW, and Limperis T. 1977. Geometrical considerations and nomenclature for reflectance. In: Commerce UDo, editor. Washington, D.C.: National Bureau of Standards.

Nilson T, and Kuusk A. 1989. A reflectance model for the homogeneous plant canopy and its inversion. Remote Sensing of Environment 27(2):157-167.

Ogburn MB, and Alber M. 2006. An investigation of salt marsh dieback in Georgia using field transplants. Estuaries and Coasts 29(1):54-62.

Pinty B; Gobron N; Widlowski JL; Gerstl SAW; Verstraete MM; Antunes M; Bacour C; Gascon F; Gastellu JP; Goel N*, et al.* . 2001. Radiation transfer model intercomparison (RAMI) exercise. Journal of Geophysical Research-Atmospheres 106(D11):11937-11956.

Pinty B; Widlowski JL; Taberner M; Gobron N; Verstraete MM; Disney M; Gascon F; Gastellu JP; Jiang L; Kuusk A*, et al.* . 2004. Radiation transfer model intercomparison (RAMI) exercise: Results from the second phase. Journal of Geophysical Research-Atmospheres 109(D6).

Press WH, Teukolsky, S.A., Vetterling, W.T., and Flannery, B.P. 1992. Numerical recipes in FORTRAN. The art of scientific computing. Cambridge: Cambridge Press.

Price JC. 1990. On the information-content of soil reflectance spectra. Remote Sensing of Environment 33(2):113-121.

Ramsey E, and Rangoonwala A. 2005. Leaf optical property changes associated with the occurrence of spartina alterniflora dieback in coastal Louisiana related to remote sensing mapping. Photogrammetric Engineering and Remote Sensing 71(3): 299-311.

Ramsey E, and Rangoonwala A. 2006. Canopy reflectance related to marsh dieback onset and progression in coastal Louisiana. Photogrammetric Engineering and Remote Sensing 72(6):641-652.

Roberts D. 2011. E-mail and phone conversation on hyperspectral marsh reflectance phenonena and the HyspIRI mission. In: Turpie KR, editor.

Rosso PH; Ustin SL, and Hastings A. 2005. Mapping marshland vegetation of San Francisco Bay, California, using hyperspectral data. International Journal of Remote Sensing 26(23):5169-5191.

Sandmeier SR. 2000. Acquisition of bidirectional reflectance factor data with field goniometers. Remote Sensing of Environment 73(3):257-269.

Sandmeier SR, and Itten KI. 1999. A field goniometer system (FIGOS) for acquisition of hyperspectral BRDF data. IEEE Transactions on Geoscience and Remote Sensing 37(2):978-986.

Sandmeier SR; Middleton EM; Deering DW, and Qin WH. 1999. The potential of hyperspectral bidirectional reflectance distribution function data for grass canopy characterization. Journal of Geophysical Research-Atmospheres 104(D8): 9547-9560.

Savitzky A, and Golay MJE. 1964. Smoothing plus differentiation of data by simplified least squares procedures. Analytical Chemistry 36(8):1627-&.

Schaepman-Strub G; Schaepman M; Painter T; Dangel S, and Martonchik J. 2006. Reflectance quantities in optical remote sensing—definitions and case studies. Remote Sensing of Environment 103(1):27-42.

Schill S; Jensen J; Raber G, and Porter D. 2004. Temporal modeling of bidirectional reflection distribution function (BRDF) in coastal vegetation. GIScience & Remote Sensing 41(2):116-135.

Schill SR. 2006. Boardwalk site data was of superior quality to the Clambank site. In: Turpie KR, editor.

Schmidt KS, and Skidmore AK. 2003. Spectral discrimination of vegetation types in a coastal wetland. Remote Sensing of Environment 85(1):92-108.

Schmidt KS, and Skidmore AK. 2004. Smoothing vegetation spectra with wavelets. International Journal of Remote Sensing 25(6):1167-1184.

Seher SS, Tueller, P.T. 1973. Color aerial photos for marshland. Photogrammetric Engineering 38(6):489-499.

Silvestri, and S. 2003. Hyperspectral remote sensing of salt marsh vegetation, morphology and soil topography. Physics and Chemistry of the Earth, Parts A/B/C 28(1-3):15-25.

Sone C; Saito K, and Futakuchi K. 2009. Comparison of three methods for estimating leaf area index of upland rice cultivars. Crop Science 49(4):1438.

Stribling JM; Cornwell JC, and Glahn OA. 2007. Microtopography in tidal marshes: Ecosystem engineering by vegetation? Estuaries and Coasts 30(6):1007-1015.

Stribling JM; Glahn OA; Chen XM, and Cornwell JC. 2006. Microtopographic variability in plant distribution and biogeochemistry in a brackish-marsh system. Marine Ecology-Progress Series 320:121-129.

Stroppiana D; Boschetti M; Confalonieri R; Bocchi S, and Brivio P. 2006. Evaluation of LAI-2000 for leaf area index monitoring in paddy rice. Field Crops Research 99 (2-3):167-170.

Stutzer DC. 1997. The effects of tidal inundation on measured spectral reflectance characteristics of coastal marsh vegetation [Master's Thesis]. [College Park]: University of Maryland. p. 108.

Tilley DR. 2003. Hyperspectral reflectance of emergent macrophytes as an indicator of water column ammonia in an oligohaline, subtropical marsh. Ecological Engineering 21(2-3):153-163.

Titus J, G. 1998. Rising seas, coastal erosion, and the takings clause: How to save wetlands and beaches without hurting property owners. Maryland Land Review 27(5):1279-1399.

Torrance KE, and Sparrow EM. 1967. Theory for off-specular reflection from roughened surfaces. Journal of the Optical Society of America 57(9):1105-&.

Underwood EC; Mulitsch MJ; Greenberg JA; Whiting ML; Ustin SL, and Kefauver SC. 2006. Mapping invasive aquatic vegetation in the Sacramento-San Joaquin delta using hyperspectral imagery. Environmental Monitoring and Assessment 121 (1-3):47-64.

UNEP UNEP. 2006. Marine and coastal ecosystems and human well-being: A synthesis report based on the findings of the millennium ecosystem assessment. Nairobi, Kenya: UNEP.

Ustin SL. 2006. Personal communication - discussion on remote sensing studies at University of California at Davis.

Vaesen K; Gilliams S; Nackaerts K, and Coppin P. 2001. Ground-measured spectral signatures as indicators of ground cover and leaf area index: The case of paddy rice. Field Crops Research 69(1):13-25.

van der Meer F. 2006. The effectiveness of spectral similarity measures for the analysis of hyperspectral imagery. International Journal of Applied Earth Observation and Geoinformation 8(1):3-17.

Vanderbilt VC; Perry GL; Livingston GP; Ustin SL; Barrios MCD; Beron FM; Leroy MM; Balois JY; Morrissey LA; Shewchuk SR*, et al.* . 2002. Inundation discriminated using sun glint. IEEE Transactions on Geoscience and Remote Sensing 40(6):1279-1287.

Verhoef W. 1984. Light-scattering by leaf layers with application to canopy reflectance modeling - the SAIL model. Remote Sensing of Environment 16(2):125-141.

Volpe V; Silvestri S, and Marani M. 2011. Remote sensing retrieval of suspended sediment concentration in shallow waters. Remote Sensing of Environment 115 (1):44-54.

Walthall CL; Norman JM; Welles JM; Campbell G, and Blad BL. 1985. Simple equation to approximate the bidirectional reflectance from vegetative canopies and bare soil surfaces. Applied Optics 24(3):383-387.

Wang F; Huang J; Tang Y, and Wang X. 2007. New vegetation index and its application in estimating leaf area index of rice. Rice Science 14(3):195-203.

Wang MH, and Bailey SW. 2001. Correction of sun glint contamination on the SeaWiFS ocean and atmosphere products. Applied Optics 40(27):4790-4798.

Webb EC, and Mendelssohn IA. 1996. Factors affecting vegetation dieback of an oligohaline marsh in coastal Louisiana: Field manipulation of salinity and submergence. American Journal of Botany 83(11):1429-1434.

Webb EC; Mendelssohn IA, and Wilsey BJ. 1995. Causes for vegetation dieback in a Louisiana salt marsh: A bioassay approach. Aquatic Botany 51(3-4):281-289.

Weihs P, Suppan, F., Richter, K., Petritsch, R., Hasenauer, H., Schneider, W. 2008. Validation of forward and inverse modes of a homogeneous canopy reflectance model. International Journal of Remote Sensing 29(5):1317-1338.

Xavier AC, and Vettorazzi CA. 2004. Mapping leaf area index through spectral vegetation indices in a subtropical watershed. International Journal of Remote Sensing 25(9):1661-1672.

Xiao X; He L; Salas W; Li C; Iii BM; Zhao R; Frolking S, and Boles S. 2002. Quantitative relationships between field-measured leaf area index and vegetation index derived from vegetation images for paddy rice fields. International Journal of Remote Sensing 23(18):3595-3604.

Zanuttigh B. 2011. Coastal flood protection: What perspective in a changing climate? The THESEUS approach. Environmental Science & Policy 14(7):845-863.

Zeisse CR. 1995. Radiance of the ocean horizon. Journal of the Optical Society of America a-Optics Image Science and Vision 12(9):2022-2030.

Zhang Y; Lin H; Chen C; Chen L; Zhang B, and Gitelson AA. 2011. Estimation of chlorophyll-a concentration in estuarine waters: Case study of the Pearl River estuary, South China Sea. Environmental Research Letters 6(2):024016.

Zhao B; Yan Y; Guo H; He M; Gu Y, and Li B. 2009. Monitoring rapid vegetation succession in estuarine wetland using time series MODIS-based indicators: An application in the Yangtze River delta area. Ecological Indicators 9(2):346-356.

Zomer RJ; Trabucco A, and Ustin SL. 2009. Building spectral libraries for wetlands land cover classification and hyperspectral remote sensing. Journal of Environmental Management 90(7):2170-2177.